

# **A study on coupled martensitic phase transformation and crack propagation- a phase-field approach**

DISSERTATION

zur Erlangung des akademischen Grades

Doktoringenieur  
(Dr.-Ing.)

von MSc. Ehsan Borzabadi Farahani  
geboren am 21.02.1984 in Shiraz, Iran

genehmigt durch die Fakultät für Maschinenbau  
der Otto-von-Guericke-Universität Magdeburg

Gutachter:

1. Prof. Dr.-Ing. Daniel Juhre
2. Prof. Dr.-Ing. Björn Kiefer

Promotionskolloquium am 25.09.2023

# Abstrakt

Die Wechselwirkung zwischen Mikrostruktur und Materialeigenschaften steht im Mittelpunkt der Materialwissenschaft sowie -technik und ist entscheidend für die Entwicklung optimaler Materialien. Materialeigenschaften wie Bruchzähigkeit, Festigkeit, Duktilität, Wärmeleitfähigkeit, thermische Stabilität, Korrosionsbeständigkeit, elektrische Leitfähigkeit, magnetische Koerzitivkraft und magnetische Hysterese sind nur einige Beispiele für die extrinsische und intrinsische „Architektur“ von Materialien, die wir maßschneidern können. Materialien mit diesen Charakteristiken haben im Gegensatz zu idealen Einkristallen meist eine komplexe Mikrostruktur. Die martensitische Phasenumwandlung (MPT) ist eine dissipative und diffusionslose Festkörperumwandlung, die zu Nano- und Mikrostrukturen unterschiedlicher Komplexität in Stählen, Formgedächtnislegierungen (SMA) und Keramiken führt. MPT-behandelte Materialien bieten wünschenswerte mechanische Eigenschaften, wie z. B. hohe Festigkeit, Formgedächtniseffekte, Pseudoelastizität und Pseudoplastizität. Die hohe Festigkeit der martensitischen Phase ist mit dem kohlenstoffbasierten Mischkristallverfestigungseffekt und der komplexen martensitischen Mikrostruktur verbunden, die durch die schnelle MPT erzeugt wird. Eine wesentliche Gefügeänderung ist die martensitische Umwandlung, bei der sich das Kristallgitter von metastabilem Austenit mit kubisch-flächenzentriertem Gitter zu stabilem Martensit mit tetragonal-raumzentriertem Gitter ändert. Die Volumenänderung und Gitterscherung, die vor der MPT auftreten, erzeugen eine umwandlungsinduzierte Eigendehnung oder Umwandlungsdehnung. Je nach Gitterscherrichtung unterschiedliche martensitische Orientierungsvarianten, die gekoppelt ein komplexes Gefüge erzeugen. Mikrorisse treten immer auf der Mikroebene der austenitischen Struktur auf, die mit Phasenumwandlungen interagiert. Hohe Spannungen an der Risspitze aktivieren und verschieben die martensitische Phase, was wiederum den Rissverlauf unterschiedlich beeinflusst. Dies bedeutet, dass die beiden Phänomene MPT und Risswachstum immer gekoppelt untersucht werden müssen.

Der Zweck dieser Studie besteht darin, das Verhalten der gekoppelten MPT und Bruchmechanik Schritt für Schritt zu simulieren und auf jeder Stufe weitere Details hinzuzufügen. Um dieses Multi-Physik-Phänomen zu modellieren, wurde der Phasenfeldansatz (PFA) verwendet. Zur Lösung der resultierenden Gleichungen wird die Finite-Elemente-Methode in dem Open-Source-Paket FEAP (Finite Element Analysis Program) verwendet. Dies wurde mittels mehrerer Subroutinen in der Programmiersprache FORTRAN umgesetzt. Die Studie konzentrierte sich zunächst auf die Simulation des martensitischen Phasenwechsels unter Berücksichtigung aller relevanten Energieterme. Die Untersuchung wurde dann um die Rissbildung und das Risswachstum in diesem martensitischen Bereich erweitert. Um der Realität näher zu kommen, wurde dann die Modellierung des Phänomens vollständig gekoppelt untersucht. Alle Modelle bis zu diesem Schritt wurden bei einer konstanten Temperatur (athermischer Prozess) durchgeführt. Schließlich wurde die Temperatur als unabhängiger Freiheitsgrad in den Gleichungssatz aufgenommen, um die Möglichkeit einer thermomechanischen Analyse des gekoppelten Problems zu schaffen.

# Abstract

The interaction between microstructure and material characteristics is at the heart of materials science and engineering, and it is critical for developing optimal materials. Material properties such as fracture toughness, strength, ductility, thermal conductivity, thermal stability, corrosion resistance, electrical conductivity, magnetic coercivity, and magnetic hysteresis are just a few examples of the extrinsic and intrinsic "architecture" of materials that we can tailor. Materials with these characteristics, in contrast to ideal single crystals, usually have a complex microstructure. Martensitic phase transformation (MPT) is a dissipative and diffusionless solid-state transformation that results in nano and microstructures of varied complexities in steels, shape memory alloys (SMA), and ceramics. MPT-treated materials offer desirable mechanical features, such as high strength, shape-memory effects, pseudoelasticity, and pseudoplasticity. The high strength of the martensitic phase is linked to carbon strong solid solution hardening effect and the complex martensitic microstructure created by the rapid MPT. The martensitic transformation, during which the crystal lattice changes from metastable austenitic with a face-centered cubic lattice to stable martensite with a body-centered tetragonal lattice, is a significant structural alteration. The volume change and lattice shear that occur prior to the MPT produce a transformation-induced eigenstrain or transformation strain. Depending on the lattice shear direction, different martensitic orientation variants develop that are coupled to generate a complex microstructure. Microcracks are always occurred on the micro-level of austenitic structure interacting with phase transformations. High stresses at the crack tip activate and shift the martensitic phase, which in turn affects the crack path differently. This means the two phenomena of MPT, and fracture must always be considered as a coupled investigation.

The purpose of this study is to simulate the behavior of the coupled MPT and fracture step by step, adding more details at each step. To model this multi physics phenomenon, phase field approach (PFA) has been utilized. To solve the resulting equations, the numerical approach of the finite element method is employed in the open-source package FEAP (Finite Element Analysis Program) which was accomplished by several subroutines in FORTRAN programming language. Firstly, this study concentrated on simulation the martensitic phase change, taking into consideration all relevant energy terms. The investigation has been then expanded to include the formation and cracks growth in this martensitic area obtained in the previous section in an uncoupled analysis. Then, in order to make the model more realistic, the interaction between MPT and fracture was investigated in a completely coupled manner. All the models up to this step were accomplished in a constant temperature (athermal process). Finally, the temperature as an independent degree of freedom has been included in the set of equations to provide the possibility for a thermomechanical analysis in the coupled problem.

# Contents

|   |           |
|---|-----------|
| <b>1 Introduction</b> .....   | <b>1</b>  |
| 1.1 Motivation .....  | 1         |
| 1.2 Overview .....  | 4         |
| <b>2 Continuum Mechanics and Thermodynamics</b> .....   | <b>7</b>  |
| 2.1 Theory of Elasticity .....  | 7         |
| 2.2 Balance Equations .....   | 8         |
| 2.3 Thermodynamics Law.....   | 10        |
| <b>3 Main Concepts and Formulations</b> .....   | <b>17</b> |
| 3.1 Martensitic phase transformation .....  | 17        |
| 3.1.1 Thermodynamic point of view on the MPT .....  | 17        |
| 3.1.2 Characteristics of the martensitic Transformation and fracture .....                                | 18        |
| 3.2 Phase-field approach for a martensitic phase transformation.....                                      | 21        |
| 3.3 Phase field approach for fracture .....   | 31        |
| 3.4 A coupled phase field approach of martensitic phase transformation and fracture.....                  | 37        |
| 3.5 A phase field approach for fracture coupled with martensitic transformation and heat transfer .....   | 41        |
| <b>4 Numerical Results and Discussion</b> .....   | <b>51</b> |
| 4.1 An uncoupled phase-field approach for martensitic transformation and fracture .....                   | 51        |
| 4.1.1 Multi-variant martensitic phase transformation .....  | 51        |
| 4.1.2 Crack initiation and propagation .....  | 57        |
| 4.2 The coupled phase-field approach for martensitic transformation and fracture.....                     | 63        |
| 4.2.1 The one variant martensitic transformation coupled with fracture (verification of the model) ..     | 63        |
| 4.2.2 The two-variant martensitic transformation coupled with fracture .....                              | 64        |
| 4.2.3 The coupled martensitic transformation and fracture in view of geometrical inhomogeneities .        | 73        |
| 4.2.4 The coupled martensitic transformation and fracture in polycrystalline structures .....             | 75        |
| 4.3 The phase field approach for fracture coupled with martensitic transformation and heat transfer ..... | 82        |



|  |            |
|--|------------|
| 4.3.1 The one variant of martensitic transformation coupled with fracture and heat transfer..... | 82         |
| 4.3.2 The two-variants martensitic transformation coupled with fracture and heat transfer.....   | 86         |
| <b>5 Conclusions and Recommendations for Future Research .....</b>                               | <b>95</b>  |
| 5.1 Main conclusions .....   | 95         |
| 5.2 Recommendations for future research.....   | 98         |
| <b>Bibliography .....</b>  | <b>100</b> |

# 1

## Introduction

### 1.1 Motivation

Most demanding characteristics of engineering materials, such as strength, resistance to corrosion, and their quality of performance, are primarily determined by their properties. These attributes are related to the material underlying the microstructure. Microstructures are directly influenced by the processes and environments in which they evolve. So, understanding microstructure evolution helps us to understand material properties and behavior. In nature, physical investigations, and contemporary technologies, phase transformation is extremely common. The significance of phase changes is associated with technologies such as heat treatment of metals, melting/solidification, use of smart materials (significantly shape memory alloys), and high-pressure synthesis of diamonds and other superhard materials (Fig. 1.1) [1].



**Figure 1.1: Some applications of the material sciences in the production of the tools; (a): stent, (b): synthetic diamond, and (c): mechanical cutting tool [2]**

Adolf Marten metallographic observations in 1890 earned him the name "martensite" [3, 4]. Due to its outstanding mechanical qualities, including high strength and resistance, Martensite has developed into a critical class of materials used in various applications, from kitchen cutlery to spacecraft. [5-7]. This structure also occupies an essential role in a wide range of industrial applications, making it necessary to thoroughly investigate its structure and behavior and fully comprehend the complexity of the MPT.

It was first used to characterize the hard phase that forms in quenched steels. It is now named to describe any diffusionless product, such as ferrous and nonferrous metals, ceramics, and minerals, during cooling or deformation. Martensite transformation occurs primarily in steels after rapid cooling from above austenitic temperatures, a process known as quenching, where the cooling rate is sufficient to inhibit diffusional solid-state changes such as ferrite and pearlite [8]. Depending on the carbon and alloying element content at room temperature, the martensite transformation may be accomplished partially or entirely. Hardenability is a property of steel that reflects its ability to create martensite upon quenching, as well as the threshold cooling rate required for martensitic transformation to occur.

In steels, MPT occurs by a diffusionless transformation of austenite with a face-centered cubic (FCC) lattice to martensite with a body-centered tetragonal (BCT) lattice. Due to the significant alloying solubility difference between the FCC and BCT lattices, the distorted BCT lattice will be strongly supersaturated with carbon. The phase transition results in a volume change and lattice shearing, which results in an eigenstrain generated by the transformation within the martensitic phase. Different orientations of martensitic variants depend on the shearing direction of the crystal lattice, which is combined to form a complex microstructure (Fig. 1.2). Internal stresses control the microstructure. The internal stresses arise even if there are no external stresses. When a significant volume change occurs, these stresses trigger the plastic deformation of martensite and the surrounding austenite. The geometry of the microstructure is entirely determined by these internal stresses [9].

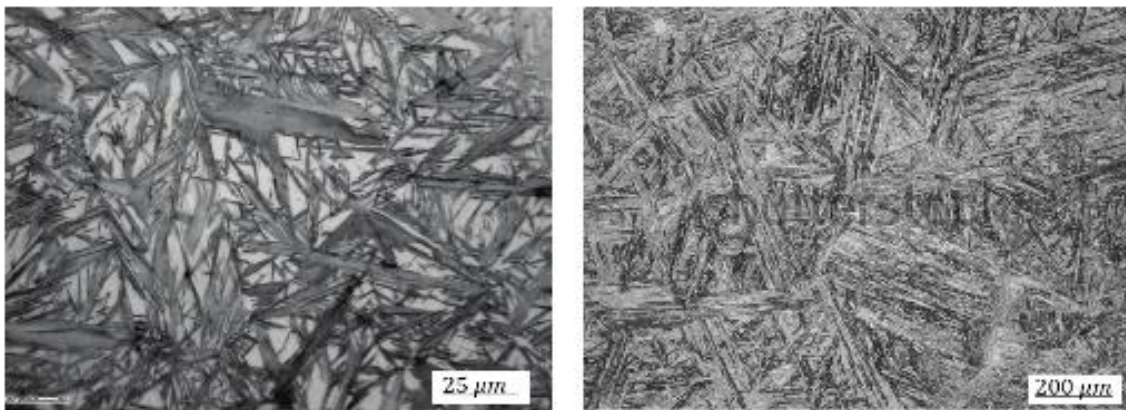


**Figure 1.2: The arrangement of the martensitic layers in two different resolutions [10]**

Microcracks in the martensitic structure are always a part of this structure, according to findings conducted in martensitic materials. These cracks, which may exist in the parent material or be generated during the phase change, affect the formation of the martensitic structure. Martensite occurs mainly at the crack tip due to a stress-induced transformation. Because of the eigenstrain acting in the martensite, this influences crack propagation. Due to high stress at the crack tip,

further crack growth and movement in the created structure has an impact on the structure and it is also rebuilt (Fig. 1.3).

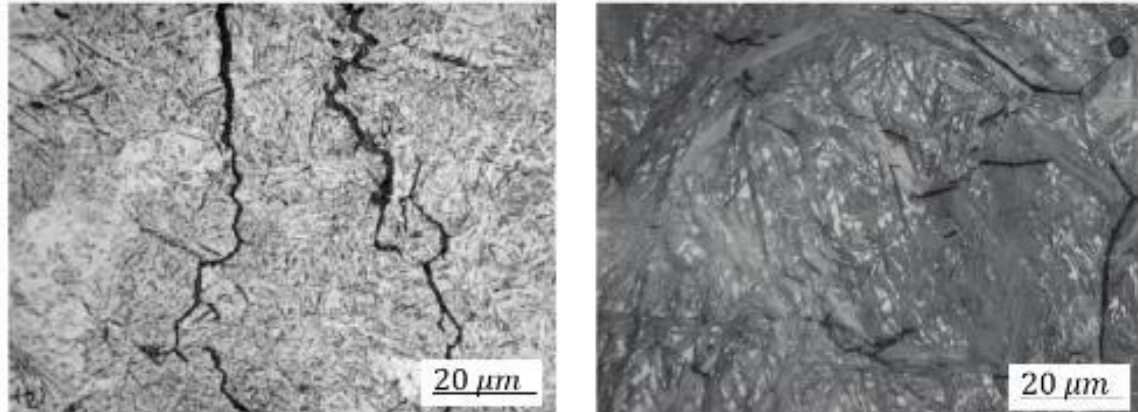


**Figure 1.3: Microcracking resulting from large volume change of MPT during a severe quench [10]**

With the use of a numerical model, the purpose of this work is to contribute to a better understanding of these complicated interactions. Although numerous studies have been conducted in this field, there is always a need for additional research due to the complexity of this phenomenon. As a result, numerical simulation approaches based on continuum mechanics, in particular, have become fundamental methodologies for modeling microstructure evolution. To explain strain-induced MPT, Reisner et al. [11] used a thermodynamic transformation criterion. In contrast, Bartel et al. [12, 13] used the idea of energy relaxation in conjunction with evolution equations deriving from inelastic potentials to model MPT. Cherkaoui et al. [14] used the concept of moving boundaries to micro-mechanically model MPT-induced plasticity micro-mechanically, assuming an indefinitely sharp boundary between the austenite and martensite phases. Regularizing discontinuities using the PFA and including an order, the parameter can help solve the problems that arise when tracking changing interfaces. The time-dependent Ginzburg-Landau (TDGL) equation [15] describes the evolution of the order parameter. The rate change of the order parameter is directly linked to the thermodynamic driving forces conjugated to the order parameter, which are the functional derivatives of the Helmholtz free energy with respect to the order parameter [16, 17]. Levitas and Preston [18] proposed a Landau theory for multivariant stress-induced MPT. Other researchers have followed these seminal works. Other studies have attempted to follow in the footsteps of these critical publications, each attempting to investigate modeling in greater depth. [19-22].

PFA to fracture models, on the other hand, has recently received a lot of interest in the literature [23] because crack paths are automatically determined as part of the solution. This method is based on Francfort and Marigo [24] variational formulation of brittle fracture, which is regularized by Bourdin et al. [25] and develops the classical Griffith's theory of fracture. The ability of the approach to elegantly represent various elements of fracture processes, including

crack initiation, propagation, merging, and branching, without the requirement for extra ad-hoc criteria, such as tracking moving borders, makes it particularly intriguing. The evolution of the smooth crack field parameter on a fixed mesh is used to track crack growth automatically. This is a significant improvement over the discrete fracture description, which requires explicit (in the conventional FEM [26, 27]) or implicit (in the extended finite element method (XFEM) [28]) addressing of the discontinuities to be numerically implemented.

In the mechanics of strength, deformational and transformational properties of materials, interactions between MPT and fracture are crucial. Despite the problem critical importance, only a few research [22, 29] looked at MPT and fracture as a combined investigation with the PFA. Clayton and Knap [30] presented and implemented a PF theory in finite element computations, including fracture and deformation twinning processes in crystalline solids. Schmitt et al. [31] proposed a combined continuum PF model for MPT and fracture. Only one variant of MPT was investigated in that study. The crack growth behavior in a solely austenitic specimen was compared to the effect of MPT combined with crack initiation and propagation. Jafarzadeh et al. [32] established a PF approach for the interaction of fracture and MPT, which incorporates the change in surface energy during MPT and the impact of unknown scale parameters proportionate to the ratio of the crack surface and phase interface widths. Ciss'e and Asle Zaeem [33] established a non-isothermal PF model to examine toughening owing to tetragonal to monoclinic martensitic transformation in CuAlBe shape memory alloy.

## 1.2 Overview

For this study, the PFA was employed to simulate the phenomenon. The equations are implemented into the FE software “FEAP” using an implicit time integration scheme for the transient terms. In the first section of the study, a pure change from austenite to martensite has been modeled using this method. The simulations have considered two martensitic variants to implement the theoretical concepts precisely. In this way, the elastic properties of each phase can be considered separately. The order parameter smoothly interpolates between the phases, which is advantageous for the PFA. It is possible to precisely control the smooth transition area and the interaction between different phases using numerical parameters and calibration input data. Based on the micro-elasticity theory, a coupled system of the TDGL equation and the equilibrium equation is established, revealing the nucleation and growth of diffusionless martensitic multi-variants forming the martensitic microstructure. The system of metastable and stable states is described using a Landau polynomial with both local and global minima, while the polynomial coefficients determine the temperature-dependent energy landscape.

Then the first endeavor was to induce the crack effect in the simulations. An uncoupled approach has been implemented to simplify and acquire the initial results of the crack behavior in a martensitic microstructure resulting from MPT. Adding a damage variable to the multi-variant MPT model allows the PFA to analyze the onset and propagation of a crack in the obtained martensitic microstructures, both with and without a pre-existing crack.

In the next part of the study, to improve the realism of the simulation, it was chosen to investigate the MPT and crack growth in a completely coupled approach. Therefore, the model comprises a coupled system of the TDGL equations and the static elasticity equation, which characterize the evolution of the distribution of austenite and two martensitic variants, as well as crack growth, in terms of corresponding order parameters. According to the numerical results, crack growth does not begin until MPT has almost completely grown through the structure. Following the formation of the martensite variants, the initial crack propagates in such a way that its path is primarily determined by the feature of the martensite variants formations, the orientation and direction in which the martensite plates are aligned together, and the stress concentration between martensitic variants. Several polycrystallines in microscale were also created in this section of the study to be investigated in this coupled PFA.

Finally, following the coupling analysis, the effect of temperature has been added as another degree of freedom in the system of governing equations. The transient heat transfer equation was defined as one of the main equations to the set of problem equations for this purpose, and this equation can influence the other results in the coupled approach. Temperature changes can have two effects on the problem: thermal strain and various energy levels for MPT. The energy level for the change of austenite to martensite is variable at each temperature, increasing as the temperature rises. This means that transformation is more difficult in high-temperature areas. Furthermore, in this thermomechanical investigation if the temperature exceeds a specific threshold, the energy released at the crack tip is insufficient to deliver the required energy for MPT, and the austenite remains intact in some regions.



# 2

## Continuum Mechanics and Thermodynamics

The fundamental relationships between continuum mechanics and thermodynamics are explained in this chapter. The definition of elasticity, which describes the linear deformation of a material body, is introduced in the first section (section 2.1). The balance equations for mass, momentum, angular momentum, energy, and entropy are explored in section 2.2, to derive general constitutive equations eventually. Altenbach [34], Gurtin et al. [35], Haupt [36], Holzapfel [37], Becker Gross [38, 39], and Levitas [2] are some of the textbooks on this subject.

### 2.1 Theory of Elasticity

The theory of elasticity is an elegant and fascinating subject that treats explicitly a particular response of materials to applied forces, namely the elastic response, in which the stress at every point in a material body (continuum) depends at all times solely on the simultaneous deformation in the immediate neighborhood of the point. If the relationship between the stress and the deformation is linear, the material is assumed to be linearly elastic, and the corresponding theory is called the linear theory of elasticity. The linear theory of elasticity deals with problems in which deformations, displacements, and rotations are "small."

In this work only, small displacement gradients have been considered leading to the linearized strain tensor.

$$\boldsymbol{\varepsilon} = \frac{1}{2}(\nabla \mathbf{u} + (\nabla \mathbf{u})^T). \quad (2.1)$$

The split of the linearized strain tensor into a spherical and a deviatoric part by

$$\boldsymbol{\varepsilon} = \underbrace{\frac{\text{tr}(\boldsymbol{\varepsilon})}{3} \mathbf{I}}_{\text{spherical part } (\boldsymbol{\varepsilon}^v)} + \mathbf{e} \quad \text{with} \quad \mathbf{e} = \boldsymbol{\varepsilon} - \frac{\text{tr}(\boldsymbol{\varepsilon})}{3} \mathbf{I} \quad (2.2)$$

which is for some problems advantageous. In the next step, the balance equations are discussed.



## 2.2 Balance Equations

In the following, the 3-D elasticity equations of motion have been derived for any continuum in motion. The fundamental postulate is that each continuum particle must satisfy Newton's law of motion. Fig. 2.1 shows the stress vectors that are acting on the six faces of a small rectangular element that is isolated from the continuum in the neighborhood of the position designated by  $x_i$ . Let  $\mathbf{B} = B_i \mathbf{e}_i$  be the body force (such as weight) per unit mass and  $\mathbf{a}$  the acceleration of a particle currently at the position  $x_i$ ; then Newton's law of motion takes the form, valid in rectangular cartesian coordinate systems:

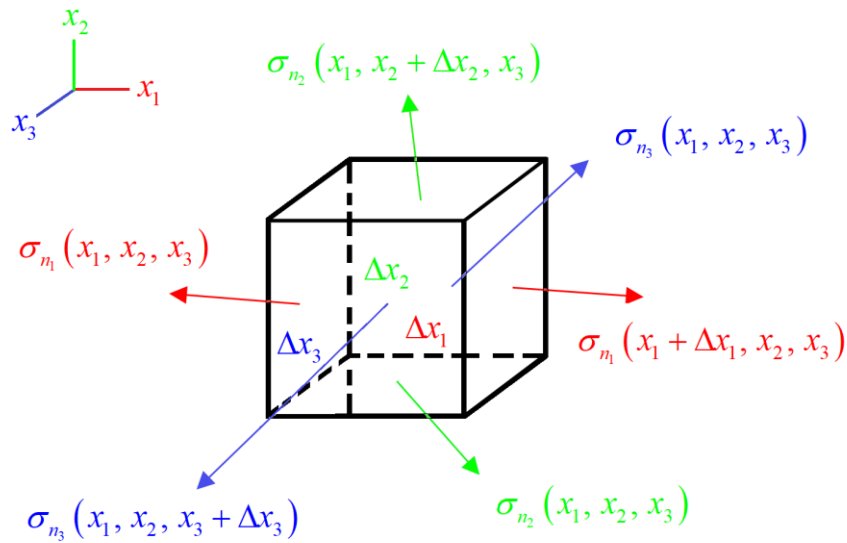


Figure 2.1: Stress vectors acting on the six faces of a small rectangular element

$$\begin{aligned}
 & \left( \sigma_{n_1}(x_1 + \Delta x_1, x_2, x_3) - \sigma_{n_1}(x_1, x_2, x_3) \right) \Delta x_2 \Delta x_3 + \\
 & \left( \sigma_{n_2}(x_1, x_2 + \Delta x_2, x_3) - \sigma_{n_2}(x_1, x_2, x_3) \right) \Delta x_1 \Delta x_3 + \\
 & \left( \sigma_{n_3}(x_1, x_2, x_3 + \Delta x_3) - \sigma_{n_3}(x_1, x_2, x_3) \right) \Delta x_1 \Delta x_2 + \rho \mathbf{B} \Delta x_1 \Delta x_2 \Delta x_3 = (\rho \mathbf{a}) \Delta x_1 \Delta x_2 \Delta x_3
 \end{aligned} \tag{2.3}$$

Dividing by  $\Delta x_1 \Delta x_2 \Delta x_3$  and considering  $\Delta x_i \rightarrow 0$ , we have

$$\frac{\partial \sigma_{n_1}}{\partial x_1} + \frac{\partial \sigma_{n_2}}{\partial x_2} + \frac{\partial \sigma_{n_3}}{\partial x_3} + \rho \mathbf{B} = \rho \mathbf{a} \tag{2.4}$$

since  $\sigma_{n_i} = \sigma_{n_i} = \sigma_{ij} n_j$ , for the different Cartesian directions we have:

$$\frac{\partial \sigma_{ij}}{\partial x_j} \mathbf{e}_i + \rho B_i \mathbf{e}_i = \rho a_i \mathbf{e}_i \quad (2.5)$$

The above equations are universal, i.e., they are independent of the type of material that we consider. The constitutive equations determine the differences between materials. The following constitutive equation between stress tensor  $\boldsymbol{\sigma}$ , strain tensor  $\boldsymbol{\varepsilon}$  and temperature  $\theta$  will be investigated in particular:

$$\boldsymbol{\sigma} = \boldsymbol{\sigma}(\boldsymbol{\varepsilon}, \theta). \quad (2.6)$$

Eq. (2.6) defines some general class of nonlinear thermoelastic materials that, may describe materials with phase transformations (PT). Thermodynamics laws impose strict limitations on constitutive equations in general and Eq. (2.6), which will be discussed later.

The linearized strain tensor yields the linear elastic constitutive law is illustrated as

$$\boldsymbol{\sigma} = \mathbf{C}\boldsymbol{\varepsilon} \quad \rightarrow \quad \sigma_{ij} = C_{ijkl} \varepsilon_{kl} \quad (2.7)$$

which is a representation of Hooke's law of elasticity. The fourth-order tensor  $\mathbf{C} = C_{ijkl}$  is called the stiffness or elasticity tensor. Due to the symmetry of the stress and strain tensor and the constitutive relation in Eq. (2.7), the tensor components  $C_{ijkl}$  possess the symmetries

$$C_{ijkl} = C_{jikl} = C_{ijlk} = C_{klij} \quad (2.8)$$

For an isotropic material, which shows the same behavior in all directions, the stiffness tensor  $\mathbf{C}$  solely depends on the two independent Lamé constants  $\lambda$  and  $\mu$

$$C_{ijkl} = \lambda \delta_{ij} \delta_{kl} + \mu (\delta_{ik} \delta_{jl} + \delta_{il} \delta_{jk}) \quad (2.9)$$

The relations between the Lamé constants and Young's modulus  $E$ , Poisson's ratio  $\nu$  and the shear modulus  $G$  are

$$\lambda = \frac{\nu E}{(1+\nu)(1-2\nu)}, \quad \mu = G = \frac{E}{2(1+\nu)} \quad (2.10)$$

with the split of the linearized strain tensor according to Eq. (2.2), the material law may be decomposed into a hydrostatic (volumetric) and a deviatoric part

$$\boldsymbol{\sigma} = K_n \boldsymbol{\varepsilon}^V \mathbf{I} + 2\mu \boldsymbol{\varepsilon}, \quad (2.11)$$

where

$$K_n = \lambda + \frac{2\mu}{n} \quad (2.12)$$

denotes the n-dimensional bulk modulus.

### 2.3 Thermodynamics Laws

Phase transformation is a thermodynamic process and thermodynamic laws represent the main rigorous tool to study it. With the help of thermodynamics, one can:

- derive the constitutive equations for stresses, entropy, and internal variables;
- determine the thermodynamic driving force for phase transformation;
- define thermodynamic stability and instability conditions of phases;
- describe the interaction between different thermomechanical processes;
- determine kinetic equations, in particular, for phase transformations;
- derive the temperature development equation;
- determine some boundary conditions.

As temperature and stress can cause PTs, Thermodynamics will answer the fundamental question, of which combination of temperature and stress tensor affects the PT.

Consider a multiphase material volume  $V$  with a boundary  $S$ . Allow the traction vector  $\mathbf{p}$  to be specified on one part of the surface and the velocity vector  $\mathbf{v}$  to be prescribed on the other portion of the surface, but mixed boundary conditions are also possible. The global (i.e., for the entire body) energy balance equation can represent the first law of thermodynamics.

$$\int_S (\mathbf{p} \cdot \mathbf{v} - \mathbf{h} \cdot \mathbf{n}) dS + \int_V \rho (\mathbf{f} \cdot \mathbf{v} + \mathbf{x}) dV = \frac{d}{dt} \int_V \rho (U + 0.5 \mathbf{v} \cdot \mathbf{v}) dV. \quad (2.13)$$

The second law of thermodynamics will be accepted in the form of the global entropy balance equation combined with the Clausius-Duhem inequality for the whole volume  $V$ :

$$S_i := \frac{d}{dt} \int_V \rho s dV - \int_V \rho \frac{\mathbf{x}}{\theta} dV + \int_S \frac{\mathbf{h}}{\theta} \cdot \mathbf{n} dS \geq 0. \quad (2.14)$$

Here  $\mathbf{h}$  is the heat flux,  $\mathbf{n}$  is the unit outer normal to  $S$ ,  $U$  is the specific (per unit mass) internal energy,  $s$  is the specific entropy,  $S_i$  is the total entropy production rate, and  $\mathbf{x}$  is the specific volumetric heat supply rate (e.g., due to electric heating).

For the reversible (equilibrium) processes, the entropy production rate is zero and the equality sign should be used in Eq. (2.14); for the irreversible (non-equilibrium) processes, the inequality sign should be used in the equation.

In Eq. (2.13), the first integral represents the power supply to the body through its surface  $S$ , namely mechanical power  $\mathbf{p} \cdot \mathbf{v}$  and normal to the surface component of the heat flux  $\mathbf{h} \cdot \mathbf{n}$ . The sign minus corresponds to the following sign convention: the heat supply to the body,  $\mathbf{h} \cdot \mathbf{n} < 0$ , positively influences the energy. The second integral denotes the power supply inside the body, including mechanical power  $\mathbf{f} \cdot \mathbf{v}$  and volumetric heat supply  $\mathbf{x}$ . Total mechanical and heat power on the left side is equal to the rate of change of the body's total energy, including internal and kinetic energy. There is no energy production, which is the essence of the energy conservation statement.

Entropy balance. Eq. (2.14) can be rewritten in the form of the entropy balance equation.

$$\frac{d}{dt} \int_V \rho s dV = \int_V \rho \frac{\mathbf{x}}{\theta} dV - \int_S \frac{\mathbf{h}}{\theta} \cdot \mathbf{n} dS + S_i; \quad S_i \geq 0. \quad (2.15)$$

In Eq. (2.15),  $\mathbf{x}/\theta$  and  $\mathbf{h}/\theta$  are considered as local volumetric entropy supply and entropy flux, respectively. As a result, the rate of change of the body entropy is equal to the entropy supply from the outside and inside, as well as the rate of entropy generation. In contrast to energy (and mass), the entropy production rate is zero for reversible processes only and positive for irreversible processes. 1 If we designate total entropy as  $\bar{S} := \int_V \rho s dV$ , total heat supply rate

$$\dot{Q} := \int_V \rho \mathbf{x} dV - \int_S \mathbf{h} \cdot \mathbf{n} dS, \text{ and assume homogeneous temperature, then Eq. (2.14) transforms to a}$$

well-known classical thermodynamic inequality.

$$\dot{\bar{S}} \geq \frac{\dot{Q}}{\theta}. \quad (2.16)$$

In statistic mechanics, the entropy is defined via number of the microstates corresponding to the current macrostate, i.e., through probability function. In macroscopic thermodynamics, entropy is defined for the reversible (equilibrium) process via Eq. (2.16), i.e.  $d\bar{S} = \frac{dQ}{\theta}$ ; both heat increment and temperature are measurable parameters, which define (to within a constant) the entropy. It is proven that entropy is a state function (like, e.g., energy), i.e., it depends on state parameters (like temperature and strain or stress) and is independent of the process leading to

the current state; then entropy is defined for the reversible process is used for an arbitrary irreversible (non-equilibrium) process, or some additional contributions are included for irreversible processes.

Transformation to the local form. Let us transform Eqs. (2.13) and (2.14) to a local point. First, one needs to transform all surface integrals to volume integrals with the help of the divergence theorem

$$\int_S \mathbf{A} \cdot \mathbf{n} dS = \int_V \nabla \cdot \mathbf{A} dV, \quad (2.17)$$

By considering the effect of the traction vector  $\mathbf{p} = \boldsymbol{\sigma} \cdot \mathbf{n}$  and  $\dot{\boldsymbol{\varepsilon}} = \nabla \dot{\mathbf{u}} = \nabla \mathbf{v}$  we will have

$$\int_S \mathbf{p} \cdot \mathbf{v} dS = \int_S \mathbf{v} \cdot \boldsymbol{\sigma} \cdot \mathbf{n} dS = \int_V \nabla \cdot (\mathbf{v} \cdot \boldsymbol{\sigma}) dV = \int_V (\mathbf{v} \cdot \nabla \cdot \boldsymbol{\sigma} + (\nabla \mathbf{v})^t : \boldsymbol{\sigma}) dV = \int_V (\mathbf{v} \cdot \nabla \cdot \boldsymbol{\sigma} + \boldsymbol{\sigma} : \dot{\boldsymbol{\varepsilon}}) dV. \quad (2.18)$$

We used the known equation for the divergence of the scalar product of vector and tensor,

$$\nabla \cdot (\mathbf{v} \cdot \boldsymbol{\sigma}) = \mathbf{v} \cdot \nabla \cdot \boldsymbol{\sigma} + (\nabla \mathbf{v})^t : \boldsymbol{\sigma} \quad (2.19)$$

Utilizing decomposition of the velocity gradient into the sum of its symmetric and skew-symmetric parts,  $\nabla \mathbf{v} = \dot{\boldsymbol{\varepsilon}} + \boldsymbol{\omega}$ , where  $\boldsymbol{\omega} := (\nabla \mathbf{v})_a$ , and the symmetry of the stress tensor, one derives  $(\nabla \mathbf{v})^t : \boldsymbol{\sigma} = \boldsymbol{\sigma} : (\nabla \mathbf{v})^t = \boldsymbol{\sigma} : (\nabla \mathbf{v})_s - \boldsymbol{\sigma} : (\nabla \mathbf{v})_a = \boldsymbol{\sigma} : \dot{\boldsymbol{\varepsilon}}$ . Using  $\dot{\boldsymbol{\varepsilon}} = (\nabla \mathbf{v})_s$ , and the fact that the double product of symmetric and skew-symmetric tensors is zero. Similarly, for the heat and the entropy fluxes

$$\int_S \mathbf{h} \cdot \mathbf{n} dS = \int_V \nabla \cdot \mathbf{h} dV; \quad \int_S \frac{\mathbf{h}}{\theta} \cdot \mathbf{n} dS = \int_V \nabla \cdot \frac{\mathbf{h}}{\theta} dV. \quad (2.20)$$

Allowing for the conservation of mass. Also, for the differentiation of the volumetric integrals, e.g., for the internal energy

$$\frac{d}{dt} \int_V \rho U dV = \frac{d}{dt} \int_V U dm = \int_V \dot{U} dm = \int_V \rho \dot{U} dV. \quad (2.21)$$

We used the conservation of mass  $\dot{m} = dm = 0$ .

Substituting Eqs. (2.18) and (2.20) for surface integrals in Eq. (2.13), using Eq. (2.21), and regrouping the terms, one obtains

$$\int_V (\boldsymbol{\sigma} : \dot{\boldsymbol{\varepsilon}} - \rho \dot{U} - \nabla \cdot \mathbf{h} + \rho x) dV + \int_V (\nabla \cdot \boldsymbol{\sigma} + \rho \mathbf{f} - \rho \dot{\mathbf{v}}) \cdot \mathbf{v} dV = 0. \quad (2.22)$$

Let us consider an observer that moves with the constant velocity  $\mathbf{a}$  with respect to a fixed frame of reference. For this observer, velocity  $\mathbf{v}$  in Eq. (2.22) should be substituted with  $\mathbf{v} - \mathbf{a}$ . Since  $\mathbf{a}$  is an arbitrary vector and the energy balance should be independent of an observer, we conclude that the term in parenthesis in the second integral in Eq. (2.22) is identically zero. In such a way we derived the local momentum balance equation Eq. (2.5) (or equation of motion). Alternatively, we can just substitute Eq. (2.5) in Eq. (2.22).

Local form of the thermodynamics laws. Then the energy balance reduces to

$$\int_V (\boldsymbol{\sigma} : \dot{\boldsymbol{\varepsilon}} - \rho \dot{U} - \nabla \cdot \mathbf{h} + \rho x) dV = 0. \quad (2.23)$$

Substituting Eq. (2.20) into Eq. (2.24), one obtains

$$S_i := \int_V (\rho \dot{s} - \rho \frac{x}{\theta} + \nabla \cdot \frac{\mathbf{h}}{\theta}) dV \geq 0. \quad (2.24)$$

Since equality (2.23) and inequality (2.24) are valid for an arbitrary volume, then they have to be valid for each material point:

$$\boldsymbol{\sigma} : \dot{\boldsymbol{\varepsilon}} - \rho \dot{U} - \nabla \cdot \mathbf{h} + \rho x = 0. \quad (2.25)$$

$$\rho \tilde{S}_i := \rho \dot{s} - \rho \frac{x}{\theta} + \nabla \cdot \frac{\mathbf{h}}{\theta} \geq 0, \quad (2.26)$$

where  $\tilde{S}_i$  is the local entropy production rate. Eqs. (2.25) and (2.26) represent the local form of the first and second laws of thermodynamics. For materials with local interaction, e.g., when behavior of each material point depends on the thermomechanical process in this point only and is independent of the processes in other points, these equations can be postulated as the primary expressions, instead of Eqs. (2.13) and (2.14).

Our next purpose is to combine Eqs. (2.25) and (2.26) in a way that is the most convenient for the derivation of the constitutive equations, e.g, equations for the stresses and entropy, as well as for the driving force for PT. First, we derive

$$\nabla \cdot \frac{\mathbf{h}}{\theta} = \frac{1}{\theta} \nabla \cdot \mathbf{h} + \mathbf{h} \cdot \nabla \left( \frac{1}{\theta} \right) = \frac{1}{\theta} \nabla \cdot \mathbf{h} - \frac{1}{\theta^2} \mathbf{h} \cdot \nabla \theta, \quad (2.27)$$

then

$$\rho \tilde{S}_i := \rho \dot{s} - \rho \frac{\dot{x}}{\theta} + \frac{1}{\theta} \nabla \cdot \mathbf{h} - \frac{1}{\theta^2} \mathbf{h} \cdot \nabla \theta \geq 0. \quad (2.28)$$

By presenting the local dissipation rate,

$$\rho D := \rho \theta \tilde{S}_i = \rho \theta \dot{s} - \rho x + \nabla \cdot \mathbf{h} - \frac{1}{\theta} \mathbf{h} \cdot \nabla \theta \geq 0. \quad (2.29)$$

Resolving Eq. (2.25) for the expression  $\nabla \cdot \mathbf{h} - \rho x$  and substituting it in Eq. (2.29), one finds the following dissipation inequality

$$\rho D = \boldsymbol{\sigma} : \dot{\boldsymbol{\varepsilon}} - \rho \dot{U} + \rho \theta \dot{s} - \frac{\nabla \theta}{\theta} \cdot \mathbf{h} \geq 0. \quad (2.30)$$

As a reasonable simplification, we assume that the heat conduction described by  $\mathbf{h}$  and thermomechanical processes described by rates  $\dot{\boldsymbol{\varepsilon}}$  and  $\dot{s}$  are mutually independent. Then the inequality (2.30) transforms to two stronger inequalities

$$\rho D = \boldsymbol{\sigma} : \dot{\boldsymbol{\varepsilon}} - \rho \dot{U} + \rho \theta \dot{s} \geq 0, \quad -\frac{\nabla \theta}{\theta} \cdot \mathbf{h} \geq 0. \quad (2.31)$$

Definitely, putting in inequality (2.30)  $\mathbf{h}=0$ , we arrive at the first inequality in Eq. (2.30), which is called the Planck's inequality. We preserve the same designation  $D$  for thermomechanical processes. Assuming inequality (2.30),  $\dot{\boldsymbol{\varepsilon}} = \dot{s} = 0$  we obtain the second inequality in Eq. (2.30), which is called Fourier's inequality.

A practical inconvenience of using the internal energy  $U$  is that according to Eq. (2.31) it should depend on  $\boldsymbol{\varepsilon}$  and  $s$ . It is much more convenient to use temperature  $\theta$  as an independent thermodynamic parameter instead of entropy. This can be done by introducing the specific

Helmholtz free energy  $\psi = U - \theta s$ . Substituting  $\dot{U} = \dot{\psi} + \theta \dot{s} + \dot{\theta} s$  in Eq. (2.31), we acquire the final expression for the dissipation inequality, which we will use

$$\rho D = \boldsymbol{\sigma} : \dot{\boldsymbol{\varepsilon}} - \rho \dot{\psi} - \rho s \dot{\theta} \geq 0. \quad (2.32)$$





# 3

## Main Concepts and Formulations

### 3.1 Martensitic Phase Transformation

#### 3.1.1 Thermodynamic point of view on the MPT

The martensitic transformation can take place in a thermal or stress-induced process. This means that the energy required for this transformation must be supplied from a source. Changing the temperature of the material or applying mechanical stresses of internal or external origin can provide this needed energy. A system with the Helmholtz free energy, which includes austenite and martensite, is defined to examine the martensitic transformation from a thermodynamic point of view. In a stress-free condition, phase transformation presupposes the existence of at least two phases, implying that free energy should have at least two extrema. Free energy has at least two local minima if both phases are stable in the presence of tiny perturbations. If the new phase is in a more stable condition of the system, the phase transition will occur. The phase transition will correspond to a move toward equilibrium. As a result, the stability of the equilibrium during finite fluctuations is a crucial factor in the treatment of MPT. The stable phase is the one with the least amount of energy. The metastable phase is the phase that corresponds to the local but not global energy minimum. The minimum corresponding to austenite vanishes at a certain critical temperature, and austenite becomes the unstable phase. Similarly, the martensite minimum disappears at a certain critical temperature, and the martensite turns into the unstable phase [2].

Fig. 3.1 shows the effect of temperature on the formation of the different energy levels in austenitic and martensitic transformation. From Fig. 3.1.a can be interpreted that when the temperature is higher than  $T_e$  austenite is stable and martensite is metastable;  $E_{M \rightarrow A}$  and  $E_{A \rightarrow M}$  are the energy barriers for phase transformations from martensite to austenite and from austenite to martensite, respectively. In this situation, the energy level required to tackle the energy barrier for austenitic transformation is lower than martensitic transformation. Fig. 3.1.b which relates to a temperature below the equilibrium temperature, shows a completely different situation from Fig. 3.1.a; martensite is stable, and austenite is metastable as the energy barrier for martensitic transformation is less than the austenitic transition.

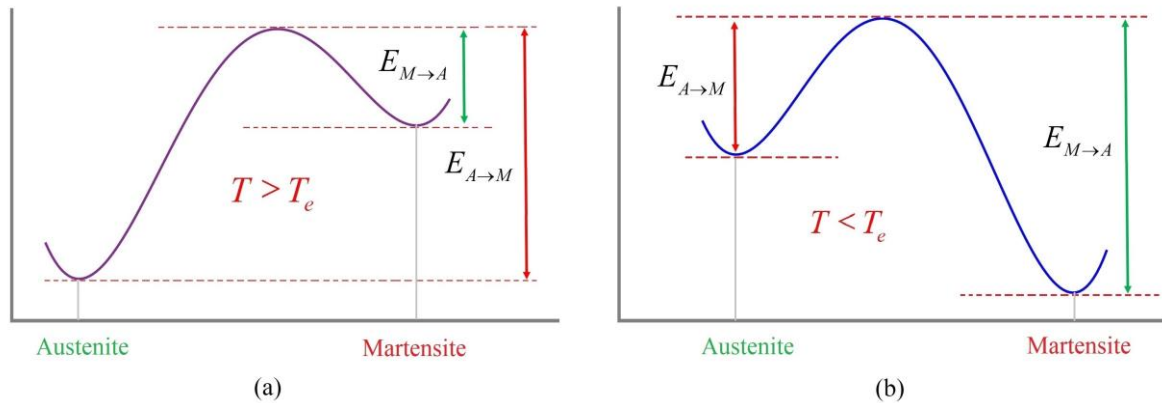


**Figure 3.1: Schematic variation of Helmholtz free energy for (a) an austenitic stable structure and (b) a martensitic stable structure**

### 3.1.2 Characteristics of the martensitic transformation and fracture

In this section, an attempt has been made to provide concepts about martensitic phase change under thermal and stress-induced conditions, as well as the relation between this transformation and fracture mechanics. Phase transformation, dislocation movement, and microcracks are found on the microscale of metastable austenitic steels. Martensite has a different crystalline structure (tetragonal) than the face-centered-cubic austenite it is made of, but the chemical and alloy composition is the same. Because the transition between these two forms occurs displacive or martensitic via the slight but quick rearranging of atomic locations, it requires activation energy and has been observed even at cryogenic temperatures. As martensite has a lower density than austenite, the martensitic transition causes a volume change [40-42].

The martensitic structure is a highly hard metastable structure with a crystal structure that is body-centered tetragonal (BCT). Martensite forms in materials when the cooling rate from austenite is so high that carbon atoms do not have enough time to diffuse. This study has concentrated on the so-called MPT. It is not limited to MPT in steel; these are more generic types of phase transitions found in various materials. The critical point is that the parent phase's crystal lattice turns into the product phase's crystal lattice without any diffusion or alteration of atoms relative neighbors [38]. If each atom in Fig. 3.2 has three neighbors during the initial phase, it will have the same three neighbors throughout the production phase. The crystal lattice does not undergo any diffusion or rebuilding.

When austenite (A) transfers to martensite (M), it retains the same amount of carbon and does not diffuse, which is the difference between diffusive and MPT. As a result, martensitic transformations are defined as a spontaneous deformation of the crystal lattice of an initial phase (austenite) to the crystal lattice of the product phase (martensite), which is accompanied by a jump in all thermomechanical properties (elastic and thermal properties, specific heat, thermal expansion coefficient, and all other mechanical and physical properties) but not

diffusion. During the metamorphosis, there are three main martensitic variants. The transformation strains cause tension in the first direction, as well as compression in the second and third. These strains produce the second martensitic variant due to the symmetry of the initial crystal lattice. Finally, transformation strain can result in tension in a third direction as well as compression in two orthogonal directions.

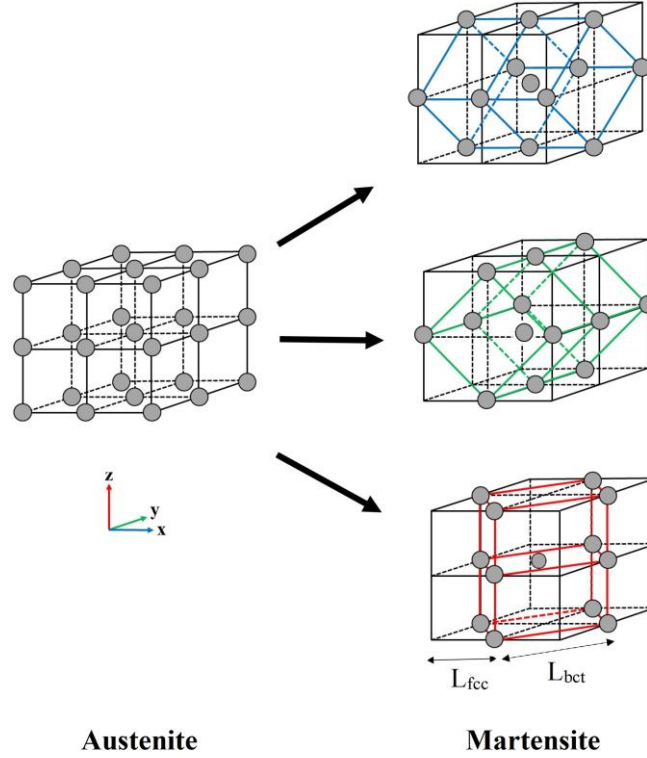


**Figure 3.2:** The Bain correspondence for martensite in steels is depicted schematically.

As a result, there are three main distinct martensitic variants. They are quite similar, yet they are still distinct since they have a different transformation strain tensor, they can exist in parallel, and have an interface between the variants. The Bain strain tensor  $\mathbf{B}$ , which can be obtained from Fig. 3.2 using the austenite and martensite lattice parameters,  $L_{fcc}$  and  $L_{bct}$ , respectively, describes this deformation in the small strain context.

$$\mathbf{B} = \begin{bmatrix} \frac{\sqrt{2}L_{bct} - L_{fcc}}{L_{fcc}} & 0 & 0 \\ 0 & \frac{\sqrt{2}L_{bct} - L_{fcc}}{L_{fcc}} & 0 \\ 0 & 0 & \frac{L_{bct} - L_{fcc}}{L_{fcc}} \end{bmatrix} \quad (3.1)$$

The occurrence of a habit plane, an undistorted and unrotated plane between the austenite and martensite, is an experimentally observed property of the martensitic transformation; see, for example, Pereloma and Edmonds [43], Zhang and Kelly [44]. The habit plane is proposed by phenomenological crystallographic theories on the martensitic transformation developed independently by Wechsler et al. [45], Bowles and Mackenzie [46], respectively.

The elastic strain energy density is obtained using micro-elasticity theory, which is illustrated schematically in Fig. 3.3. The austenite matrix spherical martensitic nuclei are separated and allowed to transform into a stress-free state (see Fig. 3.3.B). MPT is applied to the region in accordance with the Bain strain or, more broadly, the transformation strain or eigenstrain. As a result, the nuclei change shape from spherical to ellipsoidal, as illustrated in Fig. 3.3.C. The ellipsoidal martensitic inclusions are strained to keep their original size and form, as seen in Fig. 3.3.D, and are reinserted into their matrix "holes." After removing the imposed stress, the austenitic matrix containing the martensitic inclusion is relaxed. As a result, the austenite matrix resists this relaxation and exerts strain on the martensitic inclusion, as illustrated in Fig. 3.3.E.

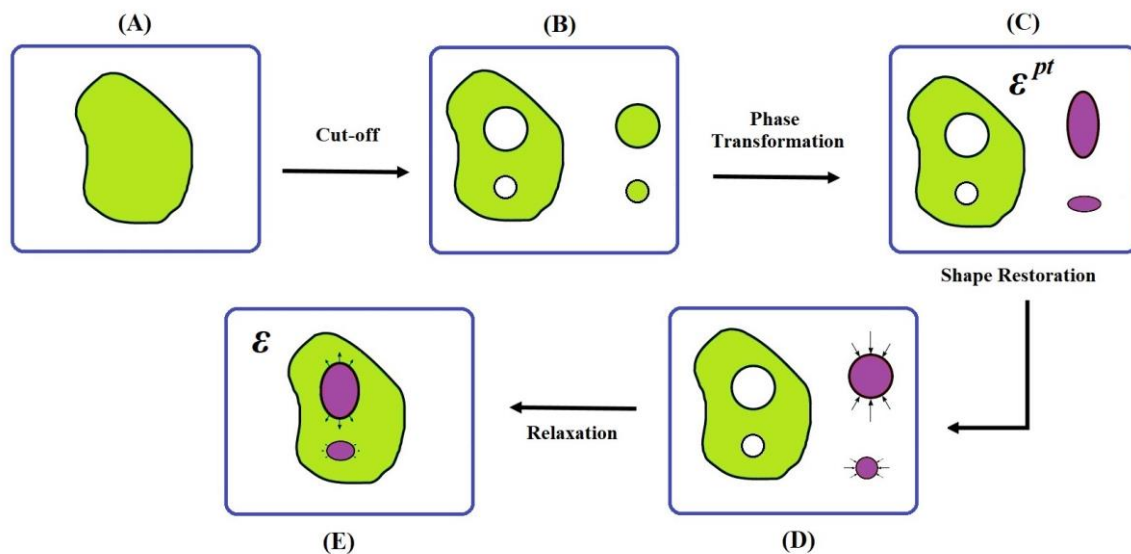


**Figure 3.3: Consecutive steps by which a coherent multi-phase microstructure is constituted, and the associated elastic strain is generated in the material based on the micro-elasticity theory.**

The internal stresses can be created in the surrounding austenite as a result of martensitic deformation. The internal stresses, in fact, totally govern the microstructure geometry while causing elastic energy to be generated. The minimum free energy principle governs phase transformation in elastic materials. This indicates that the system is attempting to use as little energy as possible. The product phase must have suitable geometry and orientation, and energy can be saved by combining different martensitic variants.

The presence of microcracks or inclusions in the parent material is the most crucial cause of stress-induced processes. The creation of these microcracks in the martensitic structure can also continue while they appear exclusively in the martensite, both in the transition zone between two plates and perpendicular to the plate directions. This is depicted in Fig. 3.4, which shows a micrograph of an austenite-martensite microstructure with cracks. The brittle martensitic structure and high interlayer stresses in this structure provide an ideal environment for microcrack formation and re-impact on the initial martensitic structure.

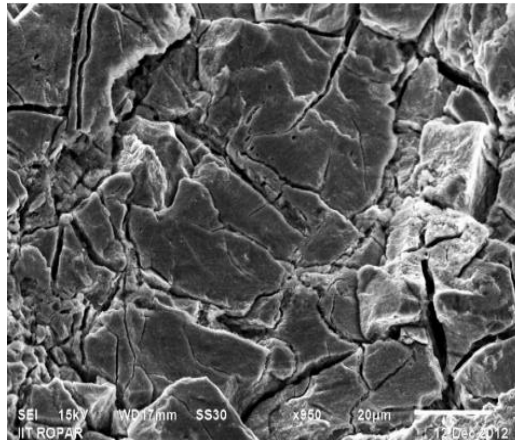


**Figure 3.4: SEM fractography of martensitic steel showing brittle fracture [47]**

This study consists of four primary sections. The initial focus of this research is the phase transformation from austenite to martensite in an athermal process. Afterward, an attempt has been made to connect this phenomenon to fracture mechanisms. This means that in the second part, concepts related to fracture mechanics were studied using the phase-field method. Since martensitic phase change and fracture mechanics are two coupled phenomena, new equations have been developed in the third section, considering the interaction between these two phenomena. In these three investigations, it was presumed that the process was carried out at an athermal condition. In the fourth section, the problem has been defined to include temperature as an independent parameter in the equations by adding the heat transfer equation into the systems. This means that equations including martensitic transformation, fracture mechanics, and thermomechanical analysis have been thoroughly developed in the fourth section.

### **3.2 Phase-field approach for a martensitic phase transformation**

PF modeling is a relatively new paradigm; it has almost become the method of favorite for simulation of interfacial problems under different concepts (e.g., compositional gradients, temperature, stress/strain, phase transformation [48], solidification [49], fracture [50], and so

on) in materials science and physics. PF modeling is also now finding ever-expanding applications in biology, medicine, and earth sciences, as well as filling the much-needed gap between the atomistic scale and continuum level of modeling. The motion of phase boundaries has attracted interest among materials scientists and engineers. Classical methods, which are known as sharp interface approaches, have been used to describe the kinetics of diffusional problems. Solving these sets of nonlinear equations is extremely difficult, stemming from the interface interactions with various complex concepts (such as merging, dissolution, and discontinuity) during the problem. PF method has overcome these difficulties through the inclusion in its formalism of a different interface description [51-53]. A PF model explains a microstructure (both the compositional and/or structural domains) with a set of field variables. The field variables are assumed to be continuous across the interfacial regions, which is the opposite of that in sharp interface models where they are discontinuous (Fig. 3.5).

In general, PFA has provided a mathematical development for the problems which involve any combination of conserved and non-conserved field variables to describe the microstructure and its evolution fully. In addition, PF is an appropriate numerical method to carry out simulations to elucidate the temporal and spatial developments relevant to the experimentally observed time and length scales. Numerous investigations have been conducted in recent years to model the MPT using the PFA. The TDGL equation describes the evolution of the order parameter [15].

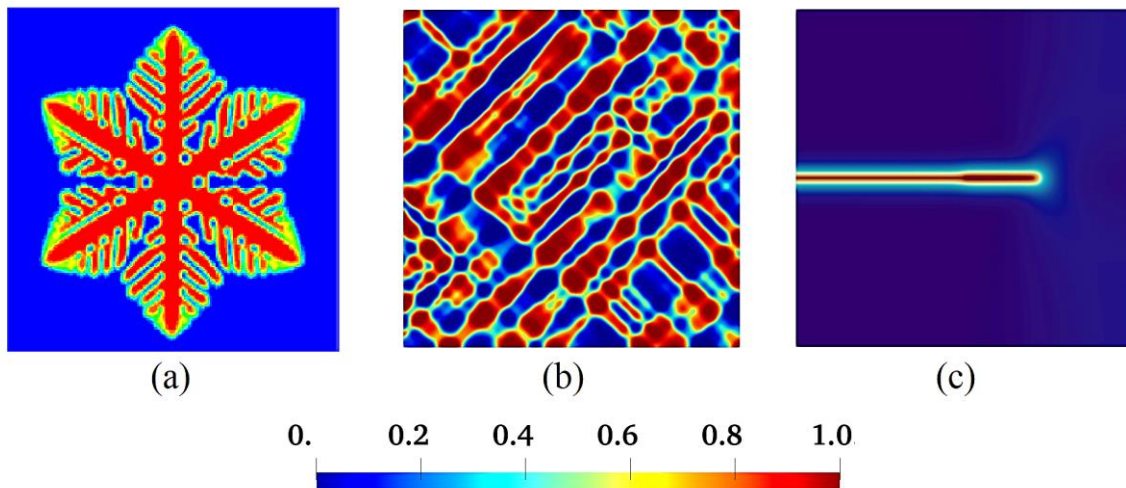


**Figure 3.5: Interfacial problems by PFA. a): Solidification [49]  
b): Phase transformation c): Fracture**

This relation linearly connected the order parameter rate of change to the thermodynamic driving forces conjugated, which are the functional derivatives of the Helmholtz free energy with respect to the order parameter [16, 17]. Levitas and Preston [18, 20] presented a Landau theory for multivariant stress-induced MPT. For arbitrary crystal symmetries, the model

incorporates temperature-dependent thermomechanical features of both austenite and martensite phases, including higher-order elastic constants. Wang and Khachaturyan [17] investigated the multi-scale phase-field approach to MPT. Zhang et al. [54] investigated the structural process of heterogeneous nucleation and growth during the martensitic change from face-centered cubic (fcc) to body-centered cubic (bcc). Yamanaka et al. [19] examined the fcc to bcc martensitic transformation in Fe-Ni polycrystalline alloys using two-dimensional elastoplastic PFA. The effects of plastic accommodation on the transformation kinetics and morphology of martensitic microstructure were investigated in their work. Levitas suggested a large strain-based phase-field theory for multivariant MPTs and simulated phase transformations in NiAl, boron nitride, and graphite to diamond [20]. Schmitt et al. [21] presented a PFA for multivariant martensitic transformations of stable and metastable phases. Their simulations illustrated that martensitic phases occur according to theoretical research and crystallographic theories, but the model's nucleation properties are flexible. Mamivand et al. [22] proposed a two-dimensional elastic PFA to simulate external stress effect on zirconia tetragonal-to-monoclinic phase transition. Schoof et al. [55] investigated the microstructure evolution of ferritic-martensitic dual-phase steels using elastic multi-phase-field modeling. She et al. [56] established a finite element framework for the PFA for MPT based on TDGL equations and used it to examine the link between heterogeneous nucleation and microscopic flaws. Babaei et al. [57] proposed a PFA for stress-induced MPT that considers the crystal lattice instability conditions derived by atomistic simulations. Mirzakhani and Javanbakht [58] solved the coupled set of time dependent PFA and elasticity equations for MPT at the nanoscale using a nonlinear finite element method (FEM).

This section continues the discussion of the PFA and its application to multivariant MPT. Following that, we will address the fundamental formulations of the second-order phase-field model for quasi-static fracture in a martensitic microstructure. Considering a multivariant microstructure composed of austenite and  $n$  symmetry-related martensitic variants that can be described in terms of order parameter dispersion,  $c_i$ . An order parameter ranging from zero to unity is defined via the PFA, where  $c_i=1$  represents the  $i_{th}$  martensitic orientation variant,  $c_i=0$  defines the austenitic phase, and  $0 < c_i < 1$  denotes an interface between two neighboring phases (Fig. 3.6).

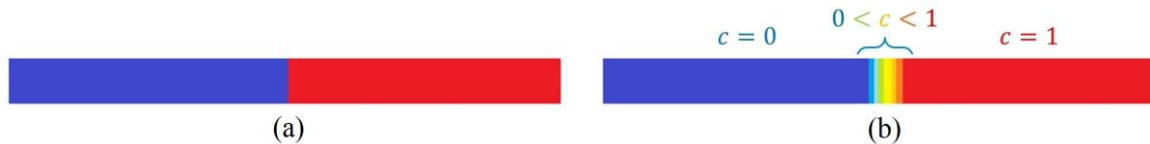


**Figure 3.6: a): Sharp interface b): Smooth interface (Phase-field)**

The transition of the crystal microstructure from the fcc structured austenitic phase to the body-centered tetragonal (bct) structured martensitic phase minimizes the Helmholtz free energy density of a martensitic transformation under isothermal conditions. The Helmholtz



free energy density  $\psi_t$  is assumed to be a function of the strain components, the gradients of the order parameters,  $c_{i,j}$  and the order parameters,  $c_i$ . As a result, the system total Helmholtz free energy,  $\psi_t$ , is given as [17]

$$\psi_t = \int_V \psi(\boldsymbol{\varepsilon}, \boldsymbol{\varepsilon}_i, \boldsymbol{\varepsilon}_{i,j}) dV \quad (3.2)$$

with

$$\psi(\boldsymbol{\varepsilon}, \boldsymbol{\varepsilon}_i, \boldsymbol{\varepsilon}_{i,j}) = W(\boldsymbol{\varepsilon}, c_i) + \psi^{grad}(c_{i,j}) + \psi^{sep}(c_i) \quad (3.3)$$

where  $W$  denotes the energy density of elastic strain. The gradient energy density generated by the sharpness of the interfaces is denoted by  $\psi^{grad}$ . As an assumption in this study,  $\psi^{sep}$  represents the chemical free energy density of an unstressed system at the temperature in question, which is invariant with respect to any rotation and symmetry of the parent phase crystal lattice. The chemical free energy density is given by using the second-order Landau polynomial expansion [16, 59]

$$\psi^{sep}(c_i) = \int_V k_s \frac{G_c}{L_c} f(c_i) dV \quad (3.4)$$

where

$$f(c_i) = 1 + \frac{A}{2}(c_1^2 + c_2^2) - \frac{B}{3}(c_1^3 + c_2^3) + \frac{D}{4}(c_1^2 + c_2^2)^2 \quad (3.5)$$

The characteristic interface energy density is denoted by the  $G_c$ . The width of the interface zone between the phases is dominated by  $L_c$ . A calibration constant is represented by  $k_s$ . The order  $i$ th parameter relating the continuous dispersion of the martensitic phase  $i$ th orientation variant is denoted by  $c_i$ . The total number of martensite variants is given by  $n$ . The Landau polynomial expansion coefficients are  $A$ ,  $B$ , and  $D$ . Due to the transformation, two distinct orientation options are considered in the case of 2-D martensitic transformation, assuming plane strain conditions. As a result, in this investigation,  $i=1$  and 2 correspond to two different orientational variants. As shown in Fig. 3.7.a, the plot of Landau polynomial expansion shows three distinct points: a saddle point at (0, 0) representing the metastable austenitic phase, and two global minimum points at (1, 0) and (0, 1), respectively, corresponding to the stable martensitic orientation variants 1 and 2.  $A = 0.15$ ,  $B = 3A + 12$ , and  $D = 2A + 12$  have been

chosen in this work to overcome the energy barrier and achieve the transformation from metastable austenite to stable martensite [19, 60, 61].

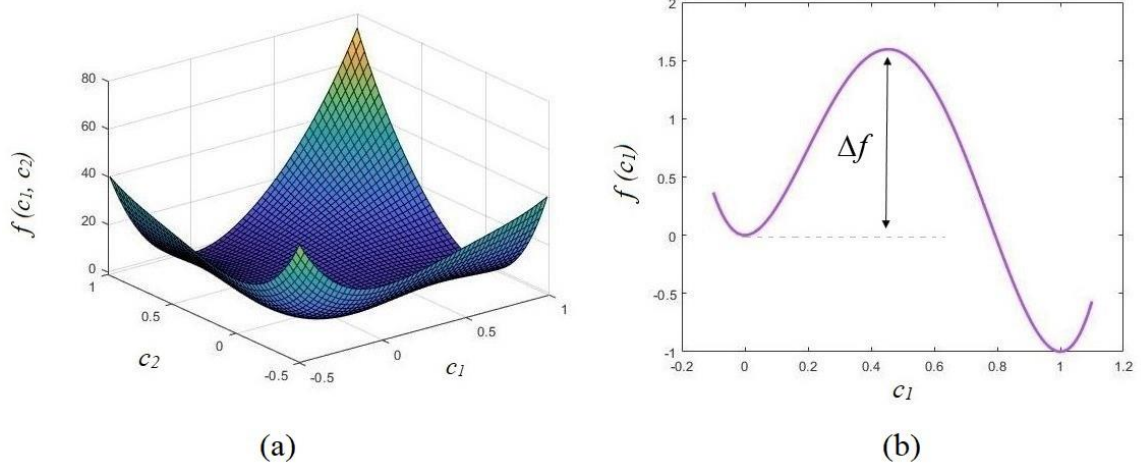


**Figure 3.7: Landau polynomial expansion: a:  $f(c_1, c_2)$  b:  $f(c_1)$**

Only the Landau polynomial expansion as a function of  $c_i$  where,  $i=1$  is studied and illustrated in Fig. 3.7.b for the purpose of simplicity. The system must overcome an energy barrier,  $\Delta f$ , in order to transition from the austenitic to the martensitic phase, that is, to transform  $c_i=0$  to  $c_i=1$ .

The elastic energy density  $W$  considers the transformation-induced eigenstrain  $\boldsymbol{\varepsilon}^{pt}(c_i)$ , which is caused by a crystallographic mismatch between the austenitic and martensitic phases. The order parameters  $c_1, c_2$  have a linear relationship with the eigenstrain tensor  $\boldsymbol{\varepsilon}_i^0$  and the elasticity tensor  $\mathbf{C}$  which is depicted schematically in Fig. 3.2. The elastic energy density is defined as [62]

$$W(\boldsymbol{\varepsilon}, c_i) = \frac{1}{2} [\boldsymbol{\varepsilon} - \boldsymbol{\varepsilon}^{pt}(c_i)] : \mathbf{C}(c_i) \frac{1}{2} [\boldsymbol{\varepsilon} - \boldsymbol{\varepsilon}^{pt}(c_i)] \quad (3.6)$$

where  $\boldsymbol{\varepsilon}^{pt}(c_i) = c_1 \boldsymbol{\varepsilon}_1^0 + c_2 \boldsymbol{\varepsilon}_2^0$ . The elastic stiffness is denoted by the material tensor  $\mathbf{C}(c_i)$  as

$$\mathbf{C}(c_i) = (1 - c_1 - c_2) \mathbf{C}_A + (c_1 + c_2) \mathbf{C}_M \quad (3.7)$$

The indices  $A$  and  $M$ , respectively, denote the austenitic and martensitic phases. Furthermore, the linearized strain tensor associated with the local displacement vector  $\mathbf{u}$  is denoted by

$$\boldsymbol{\varepsilon}(\mathbf{u}) = \frac{1}{2} [\nabla \mathbf{u} + (\nabla \mathbf{u})^T] \quad (3.8)$$

The Bain model is used to compute the eigenstrain  $\boldsymbol{\varepsilon}_i^0$  of the martensitic phases using the lattice parameters available from molecular dynamics. The eigenstrain tensor of the first variant is derived from the geometrical relations in the x-z plane in Fig. 3.1, assuming plane strain conditions. The eigenstrain tensor of the second variant is obtained by rotating the coordinate system perpendicularly.

$$\boldsymbol{\varepsilon}_1^0 = \begin{bmatrix} \frac{\sqrt{2}L_{bct} - L_{fcc}}{L_{fcc}} & 0 \\ 0 & \frac{L_{bct} - L_{fcc}}{L_{fcc}} \end{bmatrix}, \quad \boldsymbol{\varepsilon}_2^0 = \begin{bmatrix} \frac{L_{bct} - L_{fcc}}{L_{fcc}} & 0 \\ 0 & \frac{\sqrt{2}L_{bct} - L_{fcc}}{L_{fcc}} \end{bmatrix}. \quad (3.9)$$

The gradient energy is defined as the sum of gradient energies due to order parameter inhomogeneity [17].

$$\psi^{grad}(c_{i,j}) = \int_V \sum_{i=1}^2 \frac{1}{2} k_g G_c L_c |\nabla c_i|^2 dV \quad (3.10)$$

where  $k_g$  represents a calibration constant.

The reliance of the free energy on the gradient of the order parameters,  $\nabla c_i$ , is another subject that has been presented. The motivation for this is as follows. Thin surfaces with interface energy separate bulk phases in a typical microstructure. The dependency of the free energy on  $\nabla c_i$  allows one to include interface energy in the theory because the gradient of the order parameters is concentrated at the interfaces and zero within homogeneous phases. Furthermore, because the description of the phase transformation is linked to material instability and, as a result, strain (and other parameters) localization, the width of the interface will be zero without a gradient term, because the theory lacks any characteristic length. This is similar to how shear band localization is described in plasticity theory, where the thickness of a shear band is zero if the gradient term is not included. From a mathematical standpoint, such a problem is known as ill-posed, and the addition of the gradient factor causes the problem to be regularized, or well-posed. The width of the interface in numerical simulations of the ill-posed problem is equal to the size of a single finite element or finite difference mesh, indicating that the solution is mesh dependent. Because the theory does not possess a characteristic size and the actual interface width is zero, this is the case. By introducing

gradient dependency on the order parameters, one introduces a characteristic size into the theory; the interface width is limited and is defined by energy minimization. [39]

The TDGL relation characterizes the evolution of the microstructure by minimizing the system Helmholtz free energy in terms of the order parameter,  $c_i$  as defined in [17]. With regard to  $c_1$  and,  $c_2$  the variational derivatives of the PFA potential  $\psi_t$  produce

$$\frac{\partial c}{\partial t} = -M_c \frac{\delta \psi_t}{\delta c_i} = -M_c \left[ \frac{\partial W}{\partial c_i} + G_c \left( \frac{k_s}{L_c} \frac{\partial f}{\partial c_i} - k_g L_c \Delta c_i \right) \right] \quad i = 1, 2 \quad (3.11)$$

when  $M_c$  is a kinetic parameter. The mechanical quantities come into play when the elastic energy density enters the PFA potential. These must satisfy the linear momentum balance, which leads to the equilibrium condition.

$$\nabla \cdot \boldsymbol{\sigma} = 0 \quad (3.12)$$

where  $\boldsymbol{\sigma}$  is the tensor of Cauchy stress derived from the constitutive expression as

$$\begin{aligned} \boldsymbol{\sigma} &= \frac{\partial \psi_t}{\partial \boldsymbol{\varepsilon}^{el}} = \mathbf{C}(c_i)(\boldsymbol{\varepsilon}^{el}) \\ \boldsymbol{\varepsilon}^{el} &= \boldsymbol{\varepsilon} - \boldsymbol{\varepsilon}^{pl}(c_i) \end{aligned} \quad (3.13)$$

The model established in the previous section is implemented into a finite element framework in this section, with the known variables being the displacements  $\mathbf{u}$ , MPT order parameter  $c_i$ . With virtual displacements  $\mathbf{u}$  and virtual variables  $c_i$ , the weak forms can be derived from the main equation obtained in the previous section. The weak formulation of the problem is achieved by multiplying the field equations by the arbitrary test functions  $\delta \mathbf{u}$  and  $\delta c_i$  and then integrating by parts over the volume  $V$  of the computing domain. The continuous volume  $V$  is discretized spatially by dividing it into  $N_e$  finite elements, each of which occupies a domain  $\Omega_e$  [15, 63, 64]

$$V \simeq V^h = \bigcup_{e=1}^{N_e} \Omega_e \quad (3.14)$$

The mesh parameter  $h$  relates to the element size. The systems assembly is described by the assembly operator  $\cup$ . The nodal degrees of freedom  $\mathbf{u}, c_i$  and the geometry  $\mathbf{x}$  are approximated element by element by the same shape functions  $N_I$  of node  $I$ , where  $n_{el}$  is the total number of nodes per element, according to the isoparametric principle.

$$\mathbf{u}^h = \sum_{I=1}^{n_{el}} N_I \hat{\mathbf{u}}_I, \quad c_i^h = \sum_{I=1}^{n_{el}} N_I \hat{c}_{iI}, \quad \underline{\mathbf{x}}^h = \sum_{I=1}^{n_{el}} N_I \hat{\mathbf{x}}_I \quad (3.15)$$

Galerkin (or Bubnov-Galerkin) is credited with this type of approximation, and the approximate solution process is often referred to as a Galerkin method. It is also possible to use a different approximation for the weighting functions than for the dependent variable, resulting in the Petrov-Galerkin process. In two dimensions, the shape functions for a quadrilateral element with four nodes are as

$$N_I(\xi) = \frac{1}{4}(1 + \xi_1^I \xi_1)(1 + \xi_2^I \xi_2) \quad (3.16)$$

where  $\xi_i^I$  are values of the natural coordinates at node  $I$ . The chain rule can be used to create derivatives for isoparametric elements. As a result, we can have

$$\frac{\partial N_I}{\partial \xi_i} = \frac{\partial N_I}{\partial x_j} \frac{\partial x_j}{\partial \xi_i} = \frac{\partial N_I}{\partial x_j} J_{ij} \quad (3.17)$$

where the Jacobian transformation between coordinates is defined by

$$J_{ij} = \frac{\partial x_j}{\partial \xi_i} \quad (3.18)$$

The above is a series of linear equations that can be solved for the derivatives of shape functions at each natural coordinate value (e.g., quadrature point). Accordingly

$$\frac{\partial N_I}{\partial x_j} = \frac{\partial N_I}{\partial \xi_j} J^{-1} \quad (3.19)$$

Any textbook on the finite element method, such as Hughes [66], Zienkiewicz and Taylor [63], and Wriggers [67], will provide details on the computation of shape functions and derivatives.

A subprogram is written to integrate a finite element development into the general purpose program FEAP. The material parameters must be input, the finite element arrays must be computed, and any desired quantities must be produced. Furthermore, the element routine conducts basic computations to obtain nodal values for element variable contour plots [63].

For node  $I$ , the discretization of the known variables using shape functions, and  $\mathbf{B}_I^c$  are represented as

$$\mathbf{u} = N_I \hat{\mathbf{u}}_I, \quad \boldsymbol{\varepsilon} = \mathbf{B}_I^u \hat{\mathbf{u}}_I, \quad c_i = N_I \hat{c}_{iI}, \quad \dot{c}_i = N_I \hat{\dot{c}}_{iI}, \quad \nabla c_i = \mathbf{B}_I^c \hat{c}_{iI} \quad (3.20)$$

The spatial derivatives in a 2-D setting can be expressed using matrices

$$\mathbf{B}_I^u = \begin{bmatrix} N_{I,x} & 0 \\ 0 & N_{I,y} \\ N_{I,y} & N_{I,x} \end{bmatrix}, \quad \mathbf{B}_I^c = \begin{bmatrix} N_{I,x} \\ N_{I,y} \end{bmatrix} \quad (3.21)$$

The element residuals of node  $I$  in Eqs. (3.22) and (3.23) are, respectively, with virtual displacements  $\eta_u$  and virtual variable  $\eta_{c_i}$ .

$$\mathbf{R}_{e,I}^u = - \int_{\Omega} \nabla \eta_u : \boldsymbol{\sigma} dV + \int_{\Gamma} \eta_u \mathbf{t}^* dA \quad (3.22)$$

$$\mathbf{R}_{e,I}^{c_i} = - \int_{\Omega} \frac{\dot{c}_i}{M_c} \eta_{c_i} dV - \int_{\Omega} \mathbf{q}_{c_i} \nabla \eta_{c_i} dV - \int_{\Omega} \left( \frac{\partial \psi^{sep}}{\partial c_i} + \frac{\partial W}{\partial c_i} \right) \eta_{c_i} dV + \int_{\Gamma} \mathbf{q}_{c_i}^* \eta_{c_i} dA \quad (3.23)$$

where

$$\mathbf{q}_{c_i} = -k_g G_c L_c \nabla c_i. \quad (3.24)$$

Now the structure of the residual equations  $\mathbf{R}$  can be made dependent on the nodal degrees of freedom given by the global vector  $(\hat{\mathbf{d}}, \hat{\dot{\mathbf{d}}})$

$$\mathbf{R}(\hat{\mathbf{d}}, \hat{\dot{\mathbf{d}}}) = \bigcup_{e=1}^{N_e} \mathbf{R}_e \approx 0, \quad \hat{\mathbf{d}}_K = \begin{bmatrix} \hat{\mathbf{u}}_K \\ \hat{\mathbf{c}}_{iK} \end{bmatrix} \quad (3.25)$$

To solve the obtained equations, the stiffness the damping matrix must be properly defined and implemented. After determining the arrays of these matrices, the desired variables can be calculated in each element and at any time. An implicit time integration approach is employed to solve the residual equations at each time step. Using the backward Euler approach, a time step can be discretized.

$$\mathbf{R} = \mathbf{F} - \mathbf{K}\hat{\mathbf{d}}_K - \mathbf{D}\hat{\dot{\mathbf{d}}}_K = 0 \quad (3.26)$$

The stiffness matrix  $\mathbf{K}$  and the damping matrix  $\mathbf{D}$  are calculated on each element in the finite element system. The entries of the  $\mathbf{K}_{I,J,e}$  element stiffness and  $\mathbf{D}_{I,J,e}$  damping matrixes are as

$$\mathbf{K}_{I,J,e} = -\frac{\partial \mathbf{R}_I}{\partial \hat{\mathbf{d}}_J} = \begin{bmatrix} \mathbf{K}_{I,J,e}^{uu} & \mathbf{K}_{I,J,e}^{uc_1} & \mathbf{K}_{I,J,e}^{uc_2} \\ \mathbf{K}_{I,J,e}^{c_1u} & \mathbf{K}_{I,J,e}^{c_1c_1} & \mathbf{K}_{I,J,e}^{c_1c_2} \\ \mathbf{K}_{I,J,e}^{c_2u} & \mathbf{K}_{I,J,e}^{c_2c_1} & \mathbf{K}_{I,J,e}^{c_2c_2} \end{bmatrix} \quad (3.27)$$

$$\mathbf{D}_{I,J,e} = -\frac{\partial \mathbf{R}_I}{\partial \hat{\dot{\mathbf{d}}}_J} = \begin{bmatrix} 0 & 0 & 0 & 0 \\ 0 & 0 & 0 & 0 \\ 0 & 0 & \mathbf{D}_{I,J,e}^{c_1c_1} & 0 \\ 0 & 0 & 0 & \mathbf{D}_{I,J,e}^{c_2c_2} \end{bmatrix} \quad (3.28)$$

$$\mathbf{K}_{I,J,e}^{uu} = \frac{\partial \mathbf{R}_{I,e}^u}{\partial \hat{\mathbf{u}}_J} = \int_{\Omega_e} (\mathbf{B}_I^u)^T (\mathbf{C})(\mathbf{B}_J^u) dV \quad (3.29)$$

$$\mathbf{K}_{I,J,e}^{uc_i} = \frac{\partial \mathbf{R}_{I,e}^u}{\partial \hat{\mathbf{c}}_{iJ}} = \int_{\Omega_e} (\mathbf{B}_I^u)^T (\tilde{\boldsymbol{\sigma}}_i + \boldsymbol{\sigma}_i^0) N_J dV, \quad \tilde{\boldsymbol{\sigma}}_i = \frac{\partial \mathbf{C}}{\partial c_i}(\boldsymbol{\varepsilon}^{el}), \quad \boldsymbol{\sigma}_i^0 = \mathbf{C} \frac{\partial}{\partial c_i}(\boldsymbol{\varepsilon}^{el}) \quad (3.30)$$

$$\mathbf{K}_{I,J,e}^{c_iu} = \frac{\partial \mathbf{R}_{I,e}^{c_i}}{\partial \hat{\mathbf{u}}_J} = \int_{\Omega_e} N_J (\tilde{\boldsymbol{\sigma}}_i + \tilde{\boldsymbol{\sigma}}_j) (\mathbf{B}_I^u) dV \quad (3.31)$$

$$\mathbf{K}_{I,J,e}^{c_i c_i} = \frac{\partial \mathbf{R}_{I,e}^{c_i}}{\partial \hat{\mathbf{c}}_{iJ}} = \int_{\Omega_e} k_g G_c L_c (\mathbf{B}_I^c)^T \mathbf{B}_J^c dV + \int_{\Omega_e} N_I (\boldsymbol{\varepsilon}_i^0)^T (\boldsymbol{\sigma}_i^0 + 2\tilde{\boldsymbol{\sigma}}_i) dV + \int_{\Omega_e} k_s \frac{G_c}{L_c} \frac{\partial^2 f}{\partial c_i^2} N_J dV \quad (3.32)$$

$$\mathbf{K}_{I,J,e}^{c_1c_1} = \frac{\partial \mathbf{R}_{I,e}^{c_1}}{\partial \hat{c}_{ij}} = \int_{\Omega_e} N_I \left( \tilde{\boldsymbol{\sigma}}_i(\boldsymbol{\varepsilon}_i^0 + \boldsymbol{\varepsilon}_j^0) + \boldsymbol{\varepsilon}_j^0 \boldsymbol{\sigma}_i^0 + k_s \frac{G_c}{L_c} \frac{\partial^2 f}{\partial c_i \partial c_j} \right) N_J dV \quad (i \neq j) \quad (3.33)$$

$$\mathbf{D}_{I,J,e}^{c_1c_1} = \mathbf{D}_{I,J,e}^{c_2c_2} = \frac{N_I N_J}{M_c}, \quad I, J = 1, 2, \dots, n_{el} \quad (3.34)$$

### 3.3 Phase-field approach for fracture

The interaction between MPT and fracture is a critical issue in the mechanics of strength, as well as the deformational and transformational properties of materials. Despite the problem critical nature, only a few research [30-33] examined both MPT and fracture as a coupled system with the PFA. Nonetheless, as the initial objective of this work, the formation and propagation of cracks in a martensitic microstructure formed by MPT using uncoupled PFA-based finite element models has been investigated. The displacement history for a fully martensitic phase microstructure produced in the previous section is used as an input for crack start and growth using the PFA in this section.

The prediction of the unstable extension of preexisting cracks, fracture, and their growth path is principal importance of safe operations of engineering material and structures. The micro-mechanistic knowledge of fracture is vital for the improvement of materials that are resistant to premature failure in the presence of crack-like defects. Modeling of crack propagation in materials has long been a challenge in solid-state physics and materials science. The mechanisms of crack nucleation and propagation in materials are troublesome in structural design. Especially in brittle materials cracks behave unstably and propagate rapidly, leading to calamitous destruction. Numerical simulation of the fracture to predict failure behavior plays a key role in engineering. However, some computational techniques also have difficulties in predicting crack propagation, such as sharp crack modeling [68, 69] which traces failure on a single or a finite number of surface interfaces. On the other hand, one of the challenging aspects in this area is the prediction of fracture behavior and propagation without predefining a crack path. Cohesive methods [70-72] and extended finite element [73] are some of the methodologies that have been used to tackle these difficulties using sharp and diffusive crack models. In sharp crack simulations achieving a stable numerical result is problematic because of the discontinuity of the displacement field. Most of the mentioned approaches develop a predefined crack path and need remeshing to predict crack propagation and fracture behavior in materials, which is challenging and often computationally expensive.

The PFA to fracture models, in which crack paths are automatically identified as part of the solution, have received significant attention in the literature in recent years [23]. This technique is based on Francfort and Marigo variational formulation of brittle fracture [24], which was regularized by Bourdin et al. [25], and which extends the classical Griffith's theory of fracture. What makes the technique particularly appealing is its ability to effectively



represent various characteristics of fracture processes, including crack initiation, propagation, merging, and branching, without requiring extra ad-hoc criteria, such as tracking moving boundaries. The evolution of the smooth crack field parameter on a fixed mesh is used to automatically track crack growth. This provides a significant advantage over the discrete fracture description, which requires explicit (in the conventional FEM [74]) or implicit (inside (XFEM) [75]) discontinuity addressing in order to be numerically implemented. Nonetheless, a key limitation of the PFA as a continuous approach [76] for fracture is that it cannot accurately depict a genuine discontinuity. This results in the creation of continuous-discontinuous methodologies, in which a continuous description of cracking has been used (for example, using nonlocal damage models in integral or gradient form) until the last stage of failure is modeled using a discontinuous approach, such as XFEM [77-81].

Kuhn and Müller presented a PFA for quasi-static [82] and dynamic [83] situations based on a regularized version of the variational formulation of brittle fracture. Liu and Juhre [84] developed a PFA for anisotropic fracture which includes the preferential cleavage directions within each randomly oriented crystal, as well as an anisotropic material behavior with cubic symmetries, in order to simulate the complex crack pattern found in polycrystalline silicon. Makvandi et al. [85] presented a combination of gradient elasticity and PFA fracture models based on the idea of strain gradient elasticity. Additionally, Wu [76] proposed a unified PFA theory within the framework of thermodynamics for the mechanics of damage and quasi-brittle failure. De Lorenzis and Gerasimov [86] focused on the treatment of the phase-field irreversibility restriction in phase-field modeling of brittle fracture. The interested reader is referred to Ambati et al. [87] and Wu et al. [76] in the computational mechanics field, and Bourdin et al. [88] in the applied mechanics community, for detailed studies of the PFA to damage models.

Adaptive mesh approaches [89] have been the ideal solution for meeting the significantly fine mesh requirements without significantly increasing the computing cost. Muixi et al. [90] suggested a novel adaptive refinement technique for phase-field models of brittle fracture. The approach provides a computationally efficient answer to PFA high requirement for spatial resolution. The aim was to evaluate two sorts of elements: h-refined elements along fractures, which require a higher level of precision to capture the answer, and standard elements throughout the domain. Lee et al. [91] used an adaptive FE phase-field model to investigate pressure and fluid-driven fracture propagation in porous media. Badnava et al. [92] applied a phase-field model to simulate brittle fracture and thermomechanically generated cracks in homogeneous and heterogeneous materials. The adaptive mesh refinement method was utilized to produce a comprehensive technique which did not require previous information of the crack path. Patil et al. [93] created an adaptive multiscale PFA using a multiscale FEM. Their approach allows for the reversion of fine meshes next to cracks to coarse meshes, resulting in a significant reduction in computational resource use. Pramod et al. [94] presented an adaptive PFA for simulating quasi-static brittle fracture situations. The adaptive refinement in that work was based on an error indicator calculated directly from the scaled boundary

finite element method (SBFEM) solutions, without the use of stress recovery techniques. Additionally, Tian et al. [95] proposed a novel hybrid adaptive FE-PFA method for solving brittle fracture issues under quasi-static and dynamic loads. The PF model applied in this study for crack propagation is based on the variational formulation of Griffith's fracture theory [53].

$$\psi_{\bar{\Gamma}} = \int_{\Omega} W(\boldsymbol{\varepsilon})dV + \int_{\Gamma} G_s d\Gamma \quad (3.35)$$

Where  $\Omega$  denotes the domain volume in 3D or domain area in two-dimensional (2D) analysis,  $G_s$  indicates the critical energy release rate or crack surface energy in Griffith's theory,  $W$  is the elastic energy density,  $\boldsymbol{\varepsilon}$  is the strain tensor as a function of displacement ( $\mathbf{u}$ ).

The introduced variational approach to fracture by Francfort and Marigo [24] has been used to predict the nucleation, propagation, and interaction of cracks by minimizing the  $\psi_t$  energy. Solving this variational problem numerically for discrete cracks can be difficult because the crack path,  $\Gamma$ , is evolving with time. In order to overcome this difficulty, Bourdin et al. [88] proposed a volumetric approximation to the surface integral. This approximation uses a continuous scalar-valued phase parameter,  $0 < s < 1$  to represent the crack field. This phase parameter has a value of one away from the intact and a value of zero at the fully fractured regions. The values between 0 and 1 denote the transition area which is changing smoothly to define as a replacement of sharp interface (see Fig. 3.8).

Based on Francfort and Marigo [24] second order phase-field model for quasi-static brittle fracture, the total potential energy of the system is represented by

$$\psi_t(\boldsymbol{\varepsilon}, s) = \int_{\Omega} \left[ W + G_s \left( \frac{(1-s)^2}{4L_s} + L_s |\nabla s|^2 \right) \right] dV - \int_{\Gamma} \mathbf{t}^* \cdot \mathbf{u} dA \quad (3.36)$$

where  $L_s$  is the crack length-scale parameter, which can be calibrated with experimental data [96, 97].  $\mathbf{t}^* = \boldsymbol{\sigma} \mathbf{n}$  signifies the traction acting on the body exterior boundary,  $\Gamma$ , where  $\mathbf{n}$  is the volume outer normal vector.

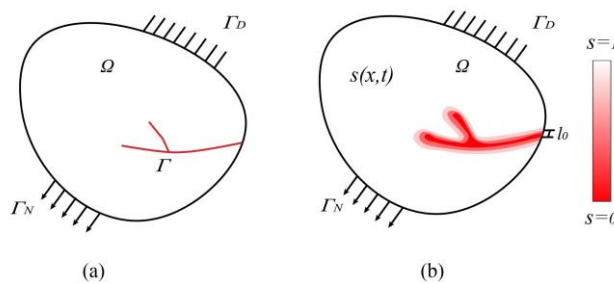


**Figure 3.8: a): Body with internal discontinuity (sharp crack), b): approximation of internal discontinuity by a phase-field model.**

Amor et al. [98] divided the strain tensor trace into positive and negative portions in order to avoid crack interpenetration during compression. As a result, a portion of the elastic energy cannot be released as a result of the formation of new crack surfaces in regions with negative volume change. By contrast, in locations with a positive volume change, elastic energy may contribute to the increase in surface energy. According to Amor et al. [98], the elastic strain energy density is split into three components: a positive volume change  $W^{vol+}$ , a negative volume change  $W^{vol-}$ , and a deviatoric component  $W^{dev}$ , which is given as

$$W = \underbrace{\frac{K(c)}{2} tr^-(\boldsymbol{\varepsilon}^{el})^2}_{W^{vol-}} + (s^2 + \zeta) \left[ \underbrace{\frac{K(c)}{2} tr^+(\boldsymbol{\varepsilon}^{el})^2}_{W^{vol+}} + \underbrace{\mu(c)(\mathbf{e} - \mathbf{e}^{pt}) : (\mathbf{e} - \mathbf{e}^{pt})}_{W^{dev}} \right] \quad (3.37)$$

$W^{eff}$

$$tr^+(\boldsymbol{\varepsilon}^{el}) = \begin{cases} tr(\boldsymbol{\varepsilon}^{el}) & \text{if } tr(\boldsymbol{\varepsilon}^{el}) \text{ is positive} \\ 0, & \text{else} \end{cases} \quad (3.38)$$

$$tr^-(\boldsymbol{\varepsilon}^{el}) = \begin{cases} tr(\boldsymbol{\varepsilon}^{el}) & \text{if } tr(\boldsymbol{\varepsilon}^{el}) \text{ is negative} \\ 0, & \text{else} \end{cases} \quad (3.39)$$

$$\boldsymbol{\varepsilon}^{el} = \boldsymbol{\varepsilon} - \boldsymbol{\varepsilon}^{pt} \quad (3.40)$$

$$\mathbf{e} = \boldsymbol{\varepsilon} - \frac{tr(\boldsymbol{\varepsilon})}{2}, \quad \mathbf{e}^{pt} = \boldsymbol{\varepsilon}^{pt} - \frac{tr(\boldsymbol{\varepsilon}^{pt})}{2} \quad (3.41)$$

$$K(c) = (1 - c_1 - c_2)K_A + (c_1 + c_2)K_M \quad (3.42)$$

$$\mu(c) = (1 - c_1 - c_2)\mu_A + (c_1 + c_2)\mu_M \quad (3.43)$$

To avoid the problem of ill-posedness, a minor value parameter,  $\zeta$ , is inserted into the equation to act as a degradation function,  $(s^2 + \zeta)$  reducing the material elastic strength [83].  $\boldsymbol{\varepsilon}^{pt}(c_i)$  is the strain tensor of the martensitic microstructure as determined in Section 3.1. The bulk and shear moduli are denoted by  $K(c)$  and  $\mu(c)$ , respectively.

According to the TDGL equation for fracture based on extended Griffith's theory [25], the variational derivative of the phase-field potential provides the evolution equation for the crack field parameter  $s$ .

$$\frac{\partial s}{\partial t} = -M_s \frac{\delta \psi_t}{\delta s} = -M_s \left( 2s(W^{vol+} + W^{dev}) - G_s \left( 2L_s \Delta s + \frac{1-s}{2L_s} \right) \right) \quad (3.44)$$

where  $M_s$  indicates the mobility parameter that scales the fracture development kinetics. To avoid the crack healing a strategy has been applied as [99, 100]

$$\dot{s} = 0 \text{ if } \frac{\delta \psi_t}{\delta s} \text{ is negative, so that } \dot{s} \leq 0 \text{ holds} \quad (3.45)$$

The 1D example of a bar of length  $2L$  with a crack in the center is examined to gain a better understanding of the meaning of  $L_s$  (Fig. 3.9).

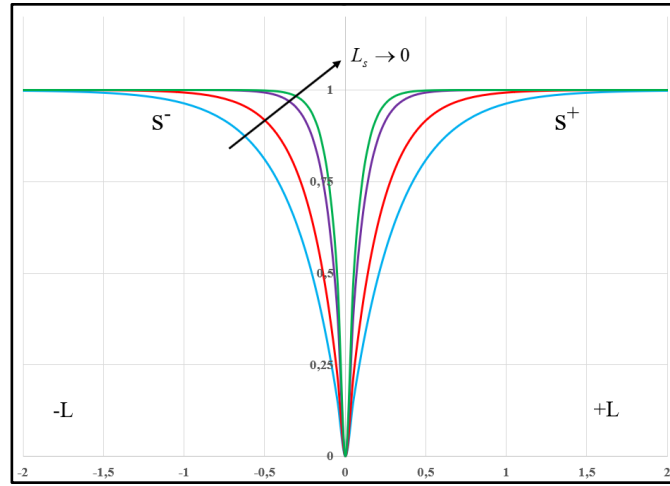


Figure 3.9: Cracked bar

Considering a stationary situation while ignoring elastic energy Eq. (3.36) produces in

$$-\frac{1}{2} = -\frac{s(x)}{2} + 2L_s^2 s''(x), \quad -L \leq x \leq L. \quad (3.46)$$

With a crack in the center (at  $x = 0$ ), the solution is

$$s^\pm(x) = 1 - \cosh\left(\frac{x}{2L_s}\right) \pm \coth\left(\frac{L}{2L_s}\right) \sinh\left(\frac{x}{2L_s}\right) \quad (3.47)$$

It is worth noting that the width of the transition area between intact and broken material is controlled by the  $L_s$  parameter, which has a length dimension. On the one hand, if the parameter  $L_s$  is not small enough in relation to the size of the main domain, which cannot evaluate the discontinuity between solid and broken areas, the shape of the damaged region. on the other hand, large values of the parameter  $L_s$  smoothen the crack field. [83, 99].

Additionally, the body equilibrium equation can be expressed as

$$\begin{aligned} \nabla \cdot \boldsymbol{\sigma} = 0, \quad \boldsymbol{\sigma} = \frac{\partial \psi_t}{\partial \boldsymbol{\varepsilon}^{el}} = K(c)tr^-(\boldsymbol{\varepsilon}^{el})\mathbf{I} + (s^2 + \zeta) \left[ K(c)tr^+(\boldsymbol{\varepsilon}^{el})\mathbf{I} + 2\mu(c)(\mathbf{e} - \mathbf{e}^{pl}) \right] \\ \mathbf{I} = [1 \quad 1 \quad 0]^T \end{aligned} \quad (3.48)$$

At this step, Eqs. (3.44) and (3.48) are implemented into ‘‘FEAP’’ within a finite element framework along with an implicit time integration scheme for the transient terms. In order to implement and solve the equations in the FEAP, the residual vector components, stiffness, and damping matrices must be constructed via a subroutine. The contributions of element  $e$  to the global residuum at node  $I$  are as

$$\mathbf{R}_{I,e}^u = \int_{\Omega_e} -(\mathbf{B}_I^u)^T \boldsymbol{\sigma} dV + \int_{\Gamma_e} N_I t^* dA \quad (3.49)$$

$$\mathbf{R}_{I,e}^s = \int_{\Omega_e} \left( -2(\mathbf{B}_I^s)^T \hat{s} L_s G_s \nabla \hat{s} - N_I (2\hat{s} W^{eff} - \frac{G_s}{2L_s} (1 - \hat{s})) \right) dV \quad (3.50)$$

The stiffness and damping matrices must be precisely defined to take a comprehensive solution. The components of these matrices are presented in the following.

$$\mathbf{u} = N_I \hat{\mathbf{u}}_I, \quad \boldsymbol{\varepsilon} = \mathbf{B}_I^u \hat{\mathbf{u}}_I, \quad s = N_I \hat{s}_I, \quad \dot{s} = N_I \dot{\hat{s}}_I, \quad \nabla s = \mathbf{B}_I^s \hat{s}_I \quad (3.51)$$

$$\mathbf{B}_I^u = \begin{bmatrix} N_{I,x} & 0 \\ 0 & N_{I,y} \\ N_{I,y} & N_{I,x} \end{bmatrix}, \quad \mathbf{B}_I^s = \begin{bmatrix} N_{I,x} \\ N_{I,y} \end{bmatrix} \quad (3.52)$$

$$\mathbf{K}_{I,J,e} = -\frac{\partial \mathbf{R}_I}{\partial \hat{\mathbf{d}}_J} = \begin{bmatrix} \mathbf{K}_{I,J,e}^{uu} & 0 & 0 & \mathbf{K}_{I,J,e}^{us} \\ 0 & 0 & 0 & 0 \\ 0 & 0 & 0 & 0 \\ \mathbf{K}_{I,J,e}^{su} & 0 & 0 & \mathbf{K}_{I,J,e}^{ss} \end{bmatrix} \quad (3.53)$$

$$\mathbf{D}_{I,J,e} = -\frac{\partial \mathbf{R}_I}{\partial \hat{\mathbf{d}}_J} = \begin{bmatrix} 0 & 0 & 0 & 0 \\ 0 & 0 & 0 & 0 \\ 0 & 0 & 0 & 0 \\ 0 & 0 & 0 & \mathbf{D}_{I,J,e}^{ss} \end{bmatrix}, \quad \mathbf{D}_{I,J,e}^{ss} = \frac{N_I N_J}{M_c} \quad (3.54)$$

$$\mathbf{K}_{IJ,e}^{uu} = \int_{\Omega_e} (\mathbf{B}_I^u)^T \frac{\partial \boldsymbol{\sigma}}{\partial \boldsymbol{\varepsilon}^{el}} (\mathbf{B}_I^u) dV \quad (3.55)$$

$$\mathbf{K}_{IJ,e}^{us} = \int_{\Omega_e} (\mathbf{B}_I^u)^T \frac{\partial \boldsymbol{\sigma}}{\partial s} N_J^s dV \quad (3.56)$$

$$\mathbf{K}_{IJ,e}^{su} = \int_{\Omega_e} 2N_I^s \left[ \frac{\partial W^{eff}}{\partial \boldsymbol{\varepsilon}^{el}} \right]^T (\mathbf{B}_J^u) dV \quad (3.57)$$

$$\mathbf{K}_{IJ,e}^{ss} = \int_{\Omega_e} \left( (\mathbf{B}_I^s)^T (2L_s G_s) (\mathbf{B}_J^s) + N_I (2W^{eff} + \frac{G_s}{L_s}) N_J^s \right) dV \quad (3.58)$$

### 3.4 A coupled phase-field approach of martensitic phase transformation and fracture

In this part of the study modeling a coupled problem in elastic materials involving crack nucleation and propagation and multivariant stress-induced MPT has been provided. An integrated Ginzburg-Landau-static-elasticity model is used to study changes in the distribution of austenite and two martensitic variations, along with crack growth in terms of the order parameters that go along with them.

Despite the problem crucial significance, only a few studies used the PF approach to consider both MPT and fracture as a couple of systems. Clayton and Knap [30] described and implemented in finite element calculations a PF theory incorporating both fracture and deformation twinning behaviors in crystalline solids. When the surface energies of the two mechanisms are equal, their results show a tendency for fracture before twinning, and a tendency for twinning to delay fracture when the fracture energy significantly exceeds the twin boundary energy. Schmitt et al. [31] proposed a combined continuum PF model for MPT and fracture. Only one variation of MPT was investigated in that study. The crack growth behavior in a purely austenitic specimen was compared to the effect of MPT combined with crack initiation and propagation. It has been reported that during the MPT, an eigenstrain in the martensitic phase increases as a result of the volume change and lattice distortion, resulting in a different stress field than a homogeneous austenitic specimen with the same load applied. Jafarzadeh et al. [32] proposed a PF approach for the interaction of fracture and MPT, which

includes the change in surface energy during MPT and the impact of unexplored scale parameters proportionate to the ratio of the crack surface and phase interface widths, both at the nanometer scale. A coupled PF model was used by Zhao et al. [101] to explore the tetragonal to monoclinic phase transformation and its toughening influence on Mode I fracture propagation in single crystalline zirconia. The numerical results in that study showed that phase change commences at the crack tip for both lattice orientations (0 and 90). The twinning forms vertically in the case of  $\theta = 0$  and is parallel to the fracture, whereas it develops horizontally in the case of  $\theta = 90$ . Moshkelgosha and Mamivand [29] investigated phase-field modeling of crack propagation in shape memory ceramics. The martensitic transformation was not combined with the variational formulation of brittle fracture in that study. Cisse and Asle Zaeem [33] presented a non-isothermal PF model to analyze toughening owing to tetragonal to monoclinic martensitic transformation in CuAlBe shape memory alloy. That work was limited to static cracks, and a stress was applied that was large enough to induce transformation but not high enough to cause significant plasticity.

The model developed in this work includes of a coupled system of three TDGL equations that define the evolution of the damage variable, two martensitic variants, and the quasi-static equilibrium equation. The positive dilatational component of the transition strain that occurs during the MPT from austenite to martensite phase leads to an eigenstrain within the martensitic phase, according to this section. Due to the fact that the eigenstrain generates both tensile and compressive loads, the models assume the sign of the dilatational component. This work focuses on the interactions between microcrack initiation and propagation and cubic to tetragonal phase transformation, which, according to the literature search has not been extensively discussed previously.

In this case, the local driving force for the formation of martensite is determined by the kinetic parameter  $M_c$  and the variational derivative  $\frac{\delta\psi_t}{\delta c_i}$ .

$$\psi_t(\boldsymbol{\varepsilon}, c_i, \nabla c_i) = W(\boldsymbol{\varepsilon}, c_i) + \psi^{grad}(\nabla c_i) + \psi^{sep}(c_i) + W^{es} \quad (3.59)$$

$$W^{es} = \frac{G_s(1-s)^2}{4L_s} + G_s L_s |\nabla s|^2 \quad (3.60)$$

The total PF potential is decomposed as follows, considering the contribution of the damage order parameter to the complete PF potential.

$$\psi_t = \underbrace{W^{vol-} + \psi^{grad} + \psi^{sep}}_{\psi_{ns}} + \underbrace{W^{vol+} + W^{dev} + W^{es}}_{\psi_s} \quad (3.61)$$

The coupled model established in this section is implemented into a finite element framework in this section, with the displacements  $\mathbf{u}$ , MPT order parameter  $c_i$ , and damage order parameter  $s$  providing as known variables.

$$\int_{\Omega} \nabla \eta_u : \boldsymbol{\sigma} dV = - \int_{\Gamma} \eta_u \mathbf{t}^* dA \quad (3.62)$$

$$\begin{aligned} & \int_{\Omega} \frac{\dot{c}_i}{M_c} \eta_{c_i} dV - \int_{\Omega} \mathbf{q}_{c_i} \cdot \nabla \eta_{c_i} dV + \int_{\Omega} (s^2 + \zeta) \frac{\partial(W^{vol+} + W^{dev})}{\partial c_i} \eta_{c_i} dV + \int_{\Omega} \frac{\partial(\psi^{sep} + W^{vol-})}{\partial c_i} \eta_{c_i} dV \\ & = - \int_{\Gamma} \mathbf{q}_{c_i}^* \eta_{c_i} dA \end{aligned} \quad (3.63)$$

$$\begin{aligned} & \int_{\Omega} \frac{\dot{s}}{M_s} \eta_s dV - \int_{\Omega} \mathbf{q}_s \cdot \nabla \eta_s dV + \int_{\Omega} \left( 2s(W^{vol+} + W^{dev}) - \frac{G_s(1-s)}{2L_s} \right) \eta_s dV \\ & = - \int_{\Gamma} \mathbf{q}_s^* \eta_s dA \end{aligned} \quad (3.64)$$

where

$$\mathbf{q}_s = -G_s L_s \nabla s. \quad (3.65)$$

Using the discretization Eq. (3.51), we can derive the nodal residuals as a function of the nodal degrees of freedom for Eqs. (3.62), (3.63) and (3.64).

$$\mathbf{R}_{I,e}^u = \int_{\Omega} (\mathbf{B}_I^u)^T \boldsymbol{\sigma} dV \quad (3.66)$$

$$\mathbf{R}_{I,e}^{c_i} = \int_{\Omega} N_I \frac{\dot{c}_i}{M_c} dV - \int_{\Omega} (\mathbf{B}_I^c)^T \mathbf{q}_{c_i} dV + \int_{\Omega} N_I \left( (s^2 + \zeta) \frac{\partial(W^{vol+} + W^{dev})}{\partial c_i} + \frac{\partial(\psi^{sep} + W^{vol-})}{\partial c_i} \right) dV \quad (3.67)$$

$$\mathbf{R}_{I,e}^s = \int_{\Omega} N_I \frac{\dot{s}}{M_s} dV - \int_{\Omega} (\mathbf{B}_I^s)^T \mathbf{q}_s dV + \int_{\Omega} N_I \left( 2s(W^{vol+} + W^{dev}) - \frac{G_s(1-s)}{2L_s} \right) dV \quad (3.68)$$

As explained previously, the residual the stiffness and damping matrix elements must be properly evaluated in order to obtain a complete solution, and these elements are shown below.



$$\mathbf{K}_{I,J,e} = -\frac{\partial \mathbf{R}_I}{\partial \hat{\mathbf{d}}_J} = \begin{bmatrix} \mathbf{K}_{I,J,e}^{uu} & \mathbf{K}_{I,J,e}^{uc_1} & \mathbf{K}_{I,J,e}^{uc_2} & \mathbf{K}_{I,J,e}^{us} \\ \mathbf{K}_{I,J,e}^{c_1u} & \mathbf{K}_{I,J,e}^{c_1c_1} & \mathbf{K}_{I,J,e}^{c_1c_2} & \mathbf{K}_{I,J,e}^{c_1s} \\ \mathbf{K}_{I,J,e}^{c_2u} & \mathbf{K}_{I,J,e}^{c_2c_1} & \mathbf{K}_{I,J,e}^{c_2c_2} & \mathbf{K}_{I,J,e}^{c_2s} \\ \mathbf{K}_{I,J,e}^{su} & \mathbf{K}_{I,J,e}^{sc_1} & \mathbf{K}_{I,J,e}^{sc_2} & \mathbf{K}_{I,J,e}^{ss} \end{bmatrix} \quad (3.69)$$

$$\mathbf{K}_{I,J,e}^{uu} = \int_{\Omega} (\mathbf{B}_I^u)^T \frac{\partial}{\partial \mathbf{u}} \left( \frac{\partial W}{\partial \boldsymbol{\varepsilon}^{el}} \right) dV \quad (3.70)$$

$$\mathbf{K}_{I,J,e}^{uc_i} = \mathbf{K}_{I,J,e}^{c_iu} = \int_{\Omega} (\mathbf{B}_I^u)^T (s^2 + \zeta) (\tilde{\boldsymbol{\sigma}} + \boldsymbol{\sigma}_{c_i}^0) N_J dV \quad (3.71)$$

$$\mathbf{K}_{I,J,e}^{us} = \mathbf{K}_{I,J,e}^{su} = \int_{\Omega} (\mathbf{B}_I^u)^T \frac{\partial W}{\partial s} N_J dV \quad (3.72)$$

$$\mathbf{K}_{I,J,e}^{c_i c_i} = \int_{\Omega} \left[ k_g G_c L_c (\mathbf{B}_I^c)^T (\mathbf{B}_I^c) + N_I \left( (s^2 + \zeta) \frac{\partial^2 (W^{vol+} + W^{dev})}{\partial c_i^2} + \frac{\partial^2 (\psi^{sep} + W^{vol-})}{\partial c_i^2} \right) \right] N_J dV \quad (3.73)$$

$$\mathbf{K}_{I,J,e}^{c_i c_j} = \mathbf{K}_{I,J,e}^{c_j c_i} = \int_{\Omega} N_I \left( (s^2 + \zeta) \frac{\partial^2 (W^{vol+} + W^{dev})}{\partial c_i \partial c_j} + \frac{\partial^2 (\psi^{sep} + W^{vol-})}{\partial c_i \partial c_j} \right) N_J dV \quad i \neq j \quad (3.74)$$

$$\mathbf{K}_{I,J,e}^{c_i s} = \mathbf{K}_{I,J,e}^{s c_i} = \int_{\Omega} N_I \left( 2s \frac{\partial (W^{vol+} + W^{dev})}{\partial c_i} \right) N_J dV \quad (3.75)$$

$$\mathbf{K}_{I,J,e}^{ss} = \int_{\Omega} \left[ G_s L_s (\mathbf{B}_I^s)^T (\mathbf{B}_I^s) + N_I \left( 2(W^{vol+} + W^{dev}) + \frac{G_s}{2L_s} \right) N_J \right] dV \quad (3.76)$$

where

$$\tilde{\boldsymbol{\sigma}} = (K_M - K_A) tr^- (\boldsymbol{\varepsilon} - \boldsymbol{\varepsilon}^{pl}) + (s^2 + \zeta) \left( (K_M - K_A) tr^+ (\boldsymbol{\varepsilon} - \boldsymbol{\varepsilon}^{pl}) + 2(\mu_M - \mu_A) (\mathbf{e} - \mathbf{e}^{pl}) \right) \quad (3.77)$$

$$\boldsymbol{\sigma}_{c_i}^0 = K(c) \frac{\partial tr^- (\boldsymbol{\varepsilon} - \boldsymbol{\varepsilon}^{pl})}{\partial c_i} + (s^2 + \zeta) \left( K(c) \frac{\partial tr^+ (\boldsymbol{\varepsilon} - \boldsymbol{\varepsilon}^{pl})}{\partial c_i} + 2\mu(c) \frac{\partial (\mathbf{e} - \mathbf{e}^{pl})}{\partial c_i} \right) \quad (3.78)$$

Furthermore, the damping matrix  $\mathbf{D}_{IJ}$  is as follow

$$\mathbf{D}_{I,J,e} = -\frac{\partial \mathbf{R}_I}{\partial \hat{\mathbf{d}}_J} = \begin{bmatrix} 0 & 0 & 0 & 0 \\ 0 & \frac{N_I^2}{M_c} & 0 & 0 \\ 0 & 0 & \frac{N_I^2}{M_c} & 0 \\ 0 & 0 & 0 & \frac{N_I^2}{M_s} \end{bmatrix} \quad (3.79)$$

### 3.5 A phase-field approach for fracture coupled with martensitic transformation and heat transfer

In the previous section a PFA has been considered to simulate a coupled crack propagation and martensitic phase transformation. The model was a five-degree of freedom problem which consists of a crack parameter, two variants of phase transformation and constitutive equations [102].

In this section, the effect of temperature as another degree of freedom has been considered. It has been supposed to model a coupled problem with crack field, two martensitic variants, temperature, and mechanical displacements (Fig. 3.10). The concept of thermodynamic driving force, the elastic energy, interfacial energy, heat transfer equation and the kinetic of phase-field equations are introduced to have the temperature field, martensitic evaluation, fracture domain and displacements [103].

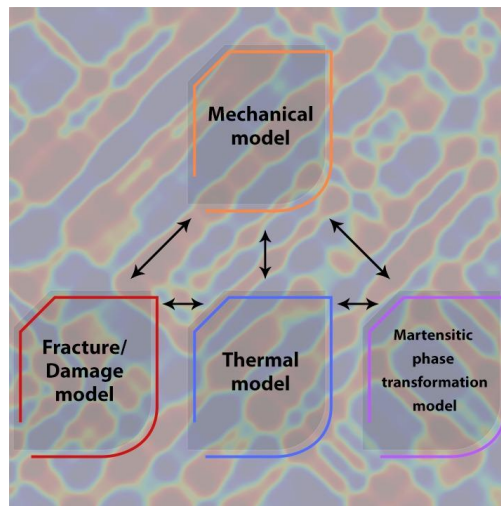


Figure 3.10: Coupling of different physics in thermo-mechanical fracture and martensitic phase transformation.

Because of high amount the stress at the tip of crack, the martensitic transformation can start and propagate thorough the austenitic structure. The internal stresses between martensitic layers deviate crack path which leads to change the martensitic formation. Also, temperature plays a key role in this phenomenon in two aspects; first changing temperature can generate thermal stresses and second has effect on martensitic transformation parameters. Increasing the temperature causes more energy to be needed for the phase transformation and changes the martensitic formation causes a new algorithm for crack growth [2, 104].

The phase-field model has been used to describe the martensitic transformation in metastable austenite, extending the model provided by [21] by include a temperature dependent separation potential and thereby accounting for heat transfer. This enables for the consideration of temperature fields that vary locally and over time. The governing field equations for the fracture, martensitic transformation, and heat transfer problem are given here. First, a general explanation of kinematics is provided. Following are discussions of concepts related to constitutive equations and evolution equations for the martensitic transformation, fracture, and heat transfer.

As degrees of freedom, we consider the displacements  $\mathbf{u} = [u_1, u_2]$ , the martensitic orientation variants  $c = [c_1, c_2]$ , damage  $s$  and the temperature  $T$ . Due to our focus on small strains, the strain tensor is additively divided into three parts

$$\boldsymbol{\varepsilon} = \boldsymbol{\varepsilon}^{el}(\mathbf{u}, c, T) + \boldsymbol{\varepsilon}^{pt}(c) + \boldsymbol{\varepsilon}^{th}(T) \quad (3.80)$$

with  $\boldsymbol{\varepsilon}^{el}$ ,  $\boldsymbol{\varepsilon}^{pt}$  and  $\boldsymbol{\varepsilon}^{th}$  denoting elastic strain, phase transformation and thermal strain, respectively. An extra inelastic strain arises when materials are subjected to temperature variations. A linear thermal expansion has been considered by [105]

$$\boldsymbol{\varepsilon}^{th} = \alpha(T - T^0) \quad (3.81)$$

The coefficient of thermal expansion  $\alpha$  is independent of temperature  $T$ . The coefficient is known to vary with temperature. However, in the temperature range of 200 to 850 K [106], the thermal expansion coefficient does not alter significantly. Furthermore, the thermal strain  $\boldsymbol{\varepsilon}^{th}$  is low in comparison to the transformation strain  $\boldsymbol{\varepsilon}^{pt}$ . It is worth noting that thermal expansion is only connected to a volumetric change. The temperature change  $T - T^0$  is proportional to the thermal strain  $\boldsymbol{\varepsilon}^{th}$ , where  $T^0$  is the initial temperature of the structure.

The heat transfer and constitutive equations along with phase-field models for fracture and martensitic transformation have been combined to simulate the three coupled physical processes. The total free energy is written as Eq. (3.61) by considering the effect of the thermal strain energy.

$$W^{vol+} = \left\{ \begin{array}{l} (s^2 + \zeta) \frac{K(c)}{2} tr(\boldsymbol{\varepsilon} - \boldsymbol{\varepsilon}^{pt} - \boldsymbol{\varepsilon}^{th})^2 \quad \text{if } tr(\boldsymbol{\varepsilon} - \boldsymbol{\varepsilon}^{pt} - \boldsymbol{\varepsilon}^{th}) \text{ is positive} \\ 0, \text{ else} \end{array} \right\} \quad (3.82)$$

$$W^{vol-} = \left\{ \begin{array}{l} \frac{K(c)}{2} tr(\boldsymbol{\varepsilon} - \boldsymbol{\varepsilon}^{pt} - \boldsymbol{\varepsilon}^{th})^2 \quad \text{if } tr(\boldsymbol{\varepsilon} - \boldsymbol{\varepsilon}^{pt} - \boldsymbol{\varepsilon}^{th}) \text{ is negative} \\ 0, \text{ else} \end{array} \right\} \quad (3.83)$$

$$W^{dev} = (s^2 + \zeta) \mu(c) (\mathbf{e} - \mathbf{e}^{pt} - \mathbf{e}^{th}) (\mathbf{e} - \mathbf{e}^{pt} - \mathbf{e}^{th}) \quad (3.84)$$

$$\mathbf{e} = \boldsymbol{\varepsilon} - \frac{tr(\boldsymbol{\varepsilon})}{2}, \quad \mathbf{e}^{pt} = \boldsymbol{\varepsilon}^{pt} - \frac{tr(\boldsymbol{\varepsilon}^{pt})}{2}, \quad \mathbf{e}^{th} = \boldsymbol{\varepsilon}^{th} - \frac{tr(\boldsymbol{\varepsilon}^{th})}{2} \quad (3.85)$$

The phase separation potential, corresponding to the chemical free energy

$$\psi^{sep} = \int_V k_s \frac{G_c}{L_c} f(c_i, T) dV \quad (3.86)$$

$$f(c_i, T) = 1 + \frac{A(T)}{2} (c_1^2 + c_2^2) - \frac{B(T)}{3} (c_1^3 + c_2^3) + \frac{D(T)}{4} (c_1^2 + c_2^2)^2 \quad (3.87)$$

$$B(T) = 3A(T) + 12, \quad D(T) = 2A(T) + 12 \quad (3.88)$$

The phase separation potential is considered to be temperature dependent, as described in [17, 107]. For low temperatures, we acquire a metastable austenitic phase and a stable martensitic phase. On the other hand, high temperatures reverse the relation, resulting in a stable austenitic and a metastable martensitic phase. This suggests that there is a temperature  $T_{eq}$  at which both phases are equally preferred.

For the parameter  $A$  we consequently assume that [104, 108]

$$\begin{aligned} \lim_{T \rightarrow T_{eq}} A(T) &\rightarrow \infty \\ A(T=0) &= 0 \end{aligned} \quad (3.89)$$

However, the dynamics close to  $T=0$  are not in the focus of interest. Using the conditions described in Eq. (3.88) a function for  $A$  is constructed, see also Fig. 3.11 [104]:

$$A(T) = \theta \frac{T(2T_{eq} - T)}{|T_{eq} - T|^\gamma} \quad (3.90)$$

where  $\theta$  and  $\gamma$  are the slope and curvature measurements, respectively. Experimental data should be used to provide the best approximation when calculating function 4. In reality, it can be noted that different values of constant parameters in Eq. (3.89) must be calibrated using laboratory data for each type of material.

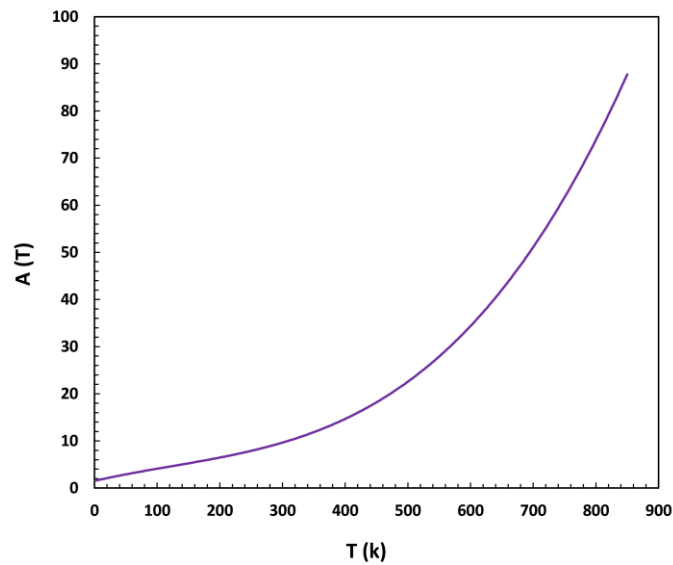


**Figure 3.11: Parameter  $A(T)$  vs. temperature  $T$  for  $\theta = 1.03$ ,  $\gamma = 0.88$  and  $T_{eq} = 823.76$  k. Crosses indicate  $A$  for different temperatures obtained by [104, 108].**

Increasing the temperature makes the phase transformation from austenite to martensite more difficult. In fact, as the temperature rises, the energy barrier between these two phases rises, requiring more energy in proportion to the temperature increase. [2] The relation between temperature and energy barrier increase in metastable austenite and stable martensite is graphically depicted in Fig. 3.12.

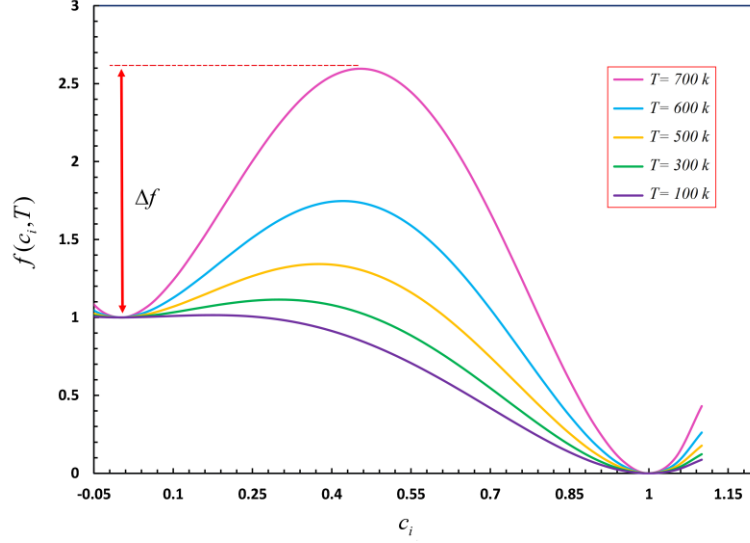


**Figure 3.12: Different level of energies according to the different temperature in a martensitic transformation of stable martensite and metastable austenite**

The work has been developed as a six-degree-of-freedom problem, which means that the six primary equations must be defined in the problem overall design. We can eventually obtain the displacements of each point ( $u_1, u_2$ ), the volume fraction of martensitic variants ( $c_1, c_2$ ), the nodes temperature ( $T$ ), and the material fracture field ( $s$ ) by solving these equations. These fundamental equations include the constitutive equations, the TDGL equations for determining the martensitic phase and damage field and the transient heat transfer [109, 110], which are given as below.

$$\nabla \cdot \boldsymbol{\sigma} = 0, \quad \boldsymbol{\sigma} = \frac{\partial W}{\partial \boldsymbol{\varepsilon}^{el}} = K(c) \text{tr}^-(\boldsymbol{\varepsilon}^{el}) \mathbf{I} + (s^2 + \zeta) \left[ K(c) \text{tr}^+(\boldsymbol{\varepsilon}^{el}) \mathbf{I} + 2\mu(c)(\boldsymbol{e}^{el}) \right] \quad (3.91)$$

$$\boldsymbol{\varepsilon}^{el} = \boldsymbol{\varepsilon} - \boldsymbol{\varepsilon}^{pt} - \boldsymbol{\varepsilon}^{th}, \quad \boldsymbol{e}^{el} = \boldsymbol{e} - \boldsymbol{e}^{pt} - \boldsymbol{e}^{th}$$

$$\frac{\partial c_i}{\partial t} = -M_c \frac{\partial \psi_t}{\partial c_i}, \quad (3.92)$$

$$\rho c_p \dot{T} + (s^2 + \zeta) \kappa \nabla^2 T = 0, \quad (3.93)$$

$$\frac{\partial s}{\partial t} = -M_s \frac{\partial \psi_t}{\partial s} \quad (3.94)$$

In this section, the equations obtained in the previous section are solved by the finite elements method. For this purpose, the weak form of the equations must first be calculated. Then the residual vectors are carefully implemented according to the weak form of each equation and the stiffness and damping matrices. On a global time scale, the transient terms  $\dot{T}$ ,  $\dot{c}_i$  and  $\dot{s}$  are

discretized [110]. The implicit Euler system is used for integration. Multiplying the field equations with a test function  $\eta$  yields the weak forms of Eqs. (3.91), (3.92), (3.93) and (3.94).

$$\int_{\Omega} \nabla \eta_u : \boldsymbol{\sigma} dV = - \int_{\Gamma} \eta_u \mathbf{t}^* dA \quad (3.95)$$

$$\begin{aligned} & \int_{\Omega} \frac{\dot{c}_i}{M_c} \eta_{c_i} dV - \int_{\Omega} \mathbf{q}_{c_i} \cdot \nabla \eta_{c_i} dV + \int_{\Omega} (s^2 + \zeta) \frac{\partial(W^{vol+} + W^{dev})}{\partial c_i} \eta_{c_i} dV + \int_{\Omega} \frac{\partial(\psi^{sep} + W^{vol-})}{\partial c_i} \eta_{c_i} dV \\ & = - \int_{\Gamma} \mathbf{q}_{c_i}^* \eta_{c_i} dA \end{aligned} \quad (3.96)$$

$$\int_{\Omega} (\eta_{th} \rho c_p \dot{T} - (s^2 + \zeta) \nabla \eta_{th} \cdot \mathbf{q}) dV = - \int_{\Gamma} \mathbf{q}_{th}^* \eta_{th} dA \quad (3.97)$$

$$\begin{aligned} & \int_{\Omega} \frac{\dot{s}}{M_s} \eta_s dV - \int_{\Omega} \mathbf{q}_s \cdot \nabla \eta_s dV + \int_{\Omega} \left( 2s(W^{vol+} + W^{dev}) - \frac{G_s(1-s)}{2L_s} \right) \eta_s dV \\ & = - \int_{\Gamma} \mathbf{q}_s^* \eta_s dA \end{aligned} \quad (3.98)$$

The residual vectors can be calculated using the weak form of the obtained equations. The first residuum corresponds to mechanical equilibrium, while the second and third are related to the TDGL equations for phase transformation and heat conduction respectively. The last one refers to the TDGL equation for the fracture.

$$\mathbf{R}_{I,e}^u = \int_{\Omega} (\mathbf{B}_I^u)^T \boldsymbol{\sigma} dV \quad (3.99)$$

$$\mathbf{R}_{I,e}^{c_i} = \int_{\Omega} \left[ N_I \frac{\dot{c}_i}{M_c} - (\mathbf{B}_I^c)^T \mathbf{q}_{c_i} + N_I \left( (s^2 + \zeta) \frac{\partial(W^{vol+} + W^{dev})}{\partial c_i} + \frac{\partial(\psi^{sep} + W^{vol-})}{\partial c_i} \right) \right] dV \quad (3.100)$$

$$\mathbf{R}_{I,e}^{th} = \int_{\Omega} (\rho c_p N_I N_J \dot{T} + \kappa (s^2 + \zeta) (\mathbf{B}_I^T)^T \nabla T) dV \quad (3.101)$$

$$\mathbf{R}_{I,e}^s = \int_{\Omega} N_I \frac{\dot{s}}{M_s} dV - \int_{\Omega} (\mathbf{B}_I^s)^T \mathbf{q}_s dV + \int_{\Omega} N_I \left( 2s(W^{vol+} + W^{dev}) - \frac{G_s(1-s)}{2L_s} \right) dV \quad (3.102)$$

The nodal stiffness matrix  $\mathbf{K}_{IJ}$  is the derivative of the residual  $\mathbf{R}_I$  with respect to the nodal degrees of freedom. Following the, the stiffness matrix  $\mathbf{K}_{IJ} \in \mathbb{R}^{6 \times 6}$  is

$$\mathbf{K}_{I,J,e} = -\frac{\partial \mathbf{R}_I}{\partial \mathbf{d}_J} = \begin{bmatrix} \mathbf{K}_{I,J,e}^{uu} & \mathbf{K}_{I,J,e}^{uc_1} & \mathbf{K}_{I,J,e}^{uc_2} & \mathbf{K}_{I,J,e}^{uT} & \mathbf{K}_{I,J,e}^{us} \\ \mathbf{K}_{I,J,e}^{c_1u} & \mathbf{K}_{I,J,e}^{c_1c_1} & \mathbf{K}_{I,J,e}^{c_1c_2} & \mathbf{K}_{I,J,e}^{c_1T} & \mathbf{K}_{I,J,e}^{c_1s} \\ \mathbf{K}_{I,J,e}^{c_2u} & \mathbf{K}_{I,J,e}^{c_2c_1} & \mathbf{K}_{I,J,e}^{c_2c_2} & \mathbf{K}_{I,J,e}^{c_2T} & \mathbf{K}_{I,J,e}^{c_2s} \\ \mathbf{K}_{I,J,e}^{Tu} & \mathbf{K}_{I,J,e}^{Tc_1} & \mathbf{K}_{I,J,e}^{Tc_2} & \mathbf{K}_{I,J,e}^{TT} & \mathbf{K}_{I,J,e}^{Ts} \\ \mathbf{K}_{I,J,e}^{su} & \mathbf{K}_{I,J,e}^{sc_1} & \mathbf{K}_{I,J,e}^{sc_2} & \mathbf{K}_{I,J,e}^{sT} & \mathbf{K}_{I,J,e}^{ss} \end{bmatrix} \quad (3.103)$$

$$\mathbf{K}_{I,J,e}^{uu} = \int_{\Omega} (\mathbf{B}_I^u)^T \frac{\partial}{\partial \mathbf{u}} \left( \frac{\partial W}{\partial \boldsymbol{\varepsilon}^{el}} \right) dV \quad (3.104)$$

$$\mathbf{K}_{I,J,e}^{uc_i} = \mathbf{K}_{I,J,e}^{c_iu} = \int_{\Omega} (\mathbf{B}_I^u)^T (s^2 + \zeta) (\tilde{\boldsymbol{\sigma}}^{th} + \boldsymbol{\sigma}_{c_i}^{th_0}) N_J dV \quad (3.105)$$

$$\mathbf{K}_{I,J,e}^{uT} = \int_{\Omega} (\mathbf{B}_I^u)^T \frac{\partial \boldsymbol{\sigma}}{\partial T} N_J dV \quad (3.106)$$

$$\mathbf{K}_{I,J,e}^{us} = \mathbf{K}_{I,J,e}^{su} = \int_{\Omega} (\mathbf{B}_I^u)^T \frac{\partial \boldsymbol{\sigma}}{\partial s} N_J dV \quad (3.107)$$

$$\begin{aligned} \mathbf{K}_{I,J,e}^{c_i c_i} &= \int_{\Omega} (s^2 + \zeta) k_g G_c L_c (\mathbf{B}_I^c)^T (\mathbf{B}_I^c) dV + \\ &\int_{\Omega} N_I \left( (s^2 + \zeta) \frac{\partial^2 (W^{vol+} + W^{dev})}{\partial c_i^2} + \frac{\partial^2 (\psi^{sep} + W^{vol-})}{\partial c_i^2} \right) N_J dV \end{aligned} \quad (3.108)$$

$$\mathbf{K}_{I,J,e}^{c_i c_j} = \mathbf{K}_{I,J,e}^{c_j c_i} = \int_{\Omega} N_I \left( (s^2 + \zeta) \frac{\partial^2 (W^{vol+} + W^{dev})}{\partial c_i \partial c_j} + \frac{\partial^2 (\psi^{sep} + W^{vol-})}{\partial c_i \partial c_j} \right) N_J dV \quad i \neq j \quad (3.109)$$

$$\mathbf{K}_{I,J,e}^{c_i T} = \int_{\Omega} \left[ N_I \left( (s^2 + \zeta) \frac{\partial^2 (W^{vol+} + W^{dev})}{\partial c_i \partial T} + \frac{\partial^2 (\psi^{sep} + W^{vol-})}{\partial c_i \partial T} \right) N_J \right] dV \quad (3.110)$$

$$\mathbf{K}_{I,J,e}^{c_i s} = \mathbf{K}_{I,J,e}^{s c_i} = \int_{\Omega} N_I \left( 2s \frac{\partial (W^{vol+} + W^{dev})}{\partial c_i} \right) N_J dV \quad (3.111)$$



$$\mathbf{K}_{I,J,e}^{Ts} = \int_{\Omega} N_J \left( 2s\kappa(\mathbf{B}_I^T) \right)^T \nabla T dV \quad (3.112)$$

$$\mathbf{K}_{I,J,e}^{TT} = \int_{\Omega} \left( (s^2 + \zeta)\kappa(\mathbf{B}_I^T) \right)^T \mathbf{B}_I^T dV \quad (3.113)$$

$$\mathbf{K}_{I,J,e}^{sT} = \int_{\Omega} N_I \left( 2s \frac{\partial(W^{vol+} + W^{dev})}{\partial T} \right) N_J dV \quad (3.114)$$

$$\mathbf{K}_{I,J,e}^{ss} = \int_{\Omega} \left[ G_s L_s (\mathbf{B}_I^s)^T (\mathbf{B}_I^s) + N_I \left( 2(W^{vol+} + W^{dev}) + \frac{G_s}{2L_s} \right) N_J \right] dV \quad (3.115)$$

$$\mathbf{K}_{I,J,e}^{Tu} = \mathbf{K}_{I,J,e}^{Tc_i} = 0 \quad (3.116)$$

where

$$\tilde{\boldsymbol{\sigma}}^{th} = (K_M - K_A) tr^-(\boldsymbol{\varepsilon}^{el}) + (s^2 + \zeta) \left( (K_M - K_A) tr^+(\boldsymbol{\varepsilon}^{el}) + 2(\mu_M - \mu_A)(\boldsymbol{e}^{el}) \right) \quad (3.117)$$

$$\boldsymbol{\sigma}_{c_i}^{th_0} = K(c) \frac{\partial tr^-(\boldsymbol{\varepsilon}^{el})}{\partial c_i} + (s^2 + \zeta) \left( K(c) \frac{\partial tr^+(\boldsymbol{\varepsilon}^{el})}{\partial c_i} + 2\mu(c) \frac{\partial(\boldsymbol{e}^{el})}{\partial c_i} \right) \quad (3.118)$$

The damping matrix is defined as the derivative of the nodal residuals  $\mathbf{R}_I$  with respect of the nodal degrees of freedom rates. The damping matrix is as follows:

$$\mathbf{D}_{I,J,e} = -\frac{\partial \mathbf{R}_I}{\partial \dot{\mathbf{d}}_J} = \begin{bmatrix} 0 & 0 & 0 & 0 & 0 & 0 \\ 0 & 0 & 0 & 0 & 0 & 0 \\ 0 & 0 & \mathbf{D}_{I,J,I}^{c_1} & 0 & 0 & 0 \\ 0 & 0 & 0 & \mathbf{D}_{I,J,I}^{c_2} & 0 & 0 \\ 0 & 0 & 0 & 0 & \mathbf{D}_{I,J,I}^T & 0 \\ 0 & 0 & 0 & 0 & 0 & \mathbf{D}_{I,J,I}^s \end{bmatrix} \quad (3.119)$$

$$\begin{aligned} \mathbf{D}_{I,J,I}^{c_1} &= \frac{\partial \mathbf{R}_I^{c_1}}{\partial \dot{c}_1} = \frac{N_I^2}{M_c}, & \mathbf{D}_{I,J,I}^{c_2} &= \frac{\partial \mathbf{R}_I^{c_2}}{\partial \dot{c}_2} = \frac{N_I^2}{M_c}, \\ \mathbf{D}_{I,J,I}^T &= \frac{\partial \mathbf{R}_I^T}{\partial \dot{T}} = \rho c_p N_I N_J, & \mathbf{D}_{I,J,I}^s &= \frac{\partial \mathbf{R}_I^s}{\partial \dot{s}} = \frac{N_I^2}{M_s} \end{aligned} \quad (3.120)$$

The obtained coupled equations are implemented into the FE software “FEAP” using an implicit time integration scheme for the transient terms.



# 4

## Numerical Results and Discussion

This chapter deals with numerical results and discussion of various analyses of martensitic transformation and fracture categorized into three main sections, namely “an uncoupled phase-field approach for martensitic transformation and fracture”, “a coupled phase field approach of martensitic phase transformation and fracture”, and “a phase field approach for fracture coupled with martensitic transformation and heat transfer”. Section 4.1 allocates the results of the uncoupled investigation, divided into subsections named “multi-variant martensitic phase transformation” and “crack initiation and propagation”. Firstly, in section 4.1.1 the concentration is on pure MPT simulation. Then in section 4.1.2 a fracture analysis has been employed on the martensitic structures obtained in section 4.1.1. In the second main section, (section 4.2), the results of the coupled MPT and fracture have been discussed. This section has four subdivisions including the numerical results of the fracture behavior coupled with one martensitic variant, and two martensitic variants, investigating the effect of geometrical inhomogeneities and polycrystalline simulations. In section 4.3 the numerical results of the phase field approach for fracture coupled with martensitic transformation and heat transfer have been presented to provide a possibility for a thermomechanical analysis of the coupled problem.

### **4.1 An uncoupled phase-field approach for martensitic transformation and fracture**

#### **4.1.1 Multi-variant martensitic phase transformation**

Using the formulation presented in Section 3.2, the numerical results have commenced by studying the martensitic phase transformation simulation. The growth of three distinct types of pre-existing martensitic embryos has been investigated: those located in the specimen center (Model 4.1), located in four specified spots (Model 4.2), and distributed randomly throughout the specimen in Model 4.3 (see Fig. 4.1). The model considers a square domain discretized by 40,000 linear 4-node elements. In this simulation, Fe–31 at.% Ni material has been chosen [54]. The material properties including mechanical properties and parameters related to martensitic transformation, are defined according to the following conditions [19, 54].

$$\begin{aligned}
 \mathbf{C}^A &= \begin{bmatrix} 140 & 84 & 0 \\ 84 & 140 & 0 \\ 0 & 0 & 28 \end{bmatrix} \text{GPa}, \quad \mathbf{C}^M = 1.1\mathbf{C}^A, \quad \boldsymbol{\varepsilon}_1^0 = \begin{bmatrix} -0.1 \\ 0.1 \\ 0 \end{bmatrix}, \quad \boldsymbol{\varepsilon}_2^0 = \begin{bmatrix} 0.1 \\ -0.1 \\ 0 \end{bmatrix} \\
 L_c &= 1 \text{ nm}, \quad G_c = 1 \frac{\text{J}}{\text{m}^2}, \quad M_c = 1.0 \times 10^{12} \frac{\text{m}^3}{\text{Js}}
 \end{aligned} \tag{4.1}$$

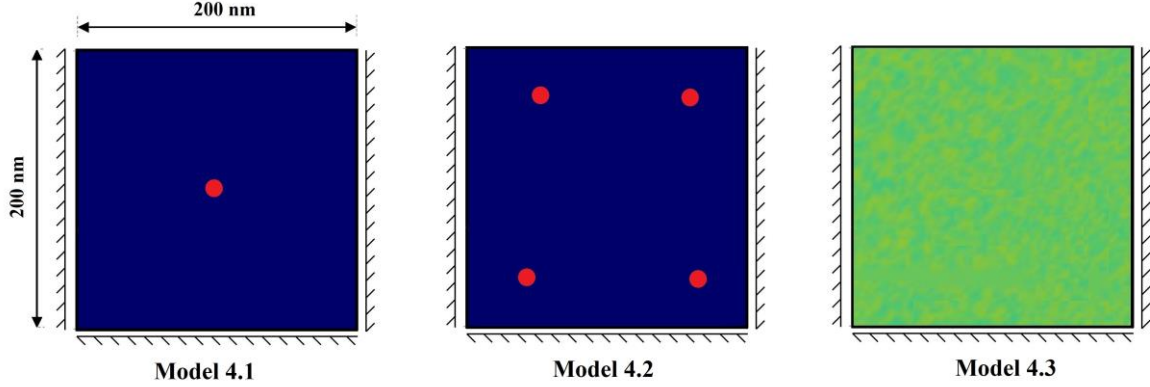
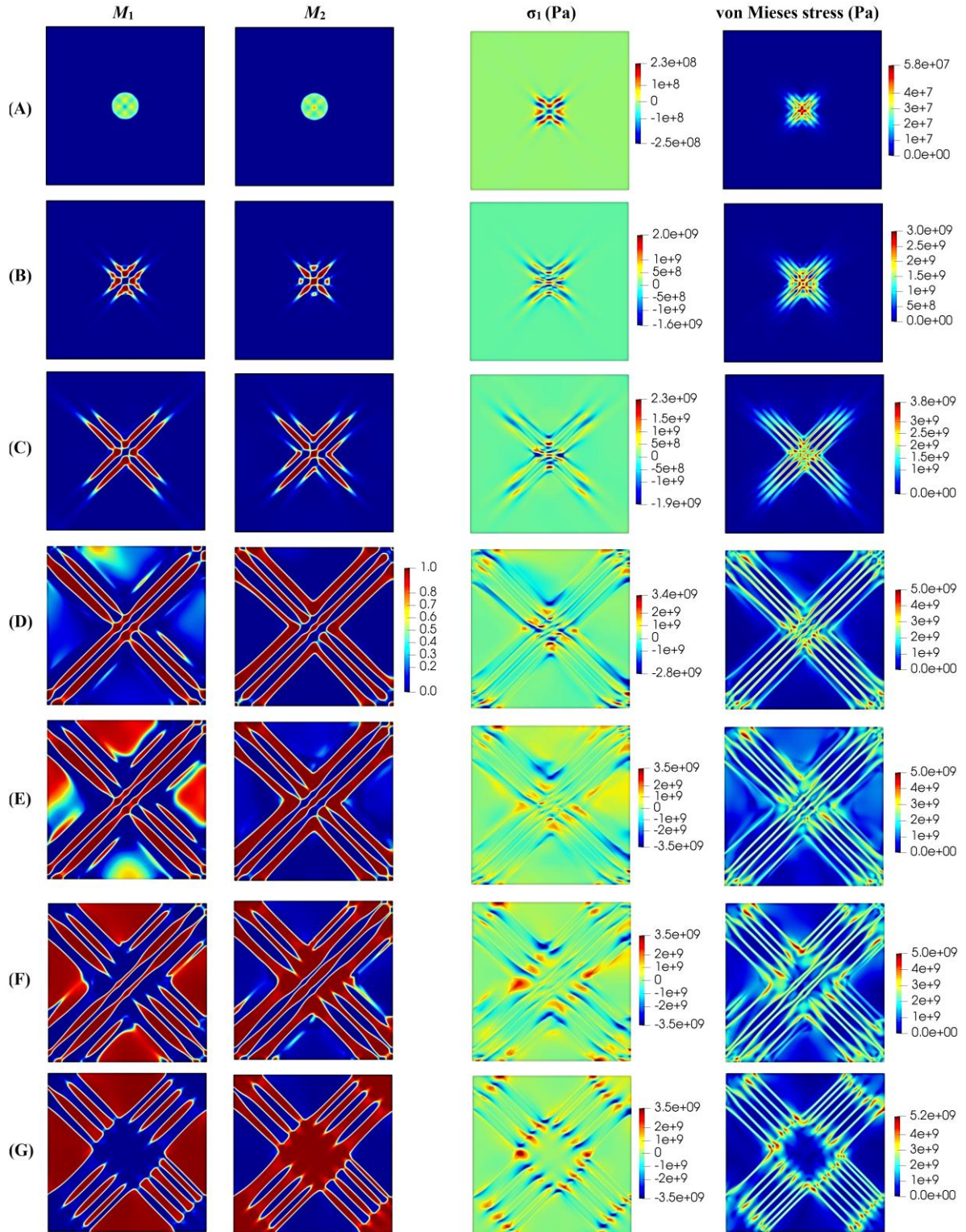


Figure 4.1: Initial and boundary conditions for the three models

where  $A$  and  $M$  denote austenite and martensitic phases. Additionally, the calibration constants  $k_g = 0.696$  and  $k_s = 1.3592$  are chosen. The specimen is initially assumed to be stress-free [19]. The evolution of the martensitic variants ( $M_1$  and  $M_2$ ) for the martensitic embryo positioned in the specimen center (Model 4.1), the stress  $\sigma_I$ , and the von Mises stress are depicted in Fig. 4.2 at different time points of 100 ms, 115 ms, 125 ms, 145 ms, 150 ms, 155 ms, and 350 ms, respectively. The zero-order parameters  $c_1 = c_2 = 0$  (which correspond to the austenite phase) are considered in this figure for the entire specimen except for the initial multivariant martensitic embryo, which has the order parameters  $c_1 = c_2 = 0.5$ . The embryos of both variants develop similarly, as seen in stages (B) and (C). It is worth noting that the martensitic variety  $M_1$  grows both vertically and horizontally, but the martensitic variant  $M_2$  grows primarily under  $45^\circ$  to coordinate axes.

According to Model 4.2, Fig. 4.3 depicts the evolution of the microstructure for martensitic variants, stress  $\sigma_I$ , and von Mises stress. The four martensitic embryos progress into the parent phase during stages (B)-(C), and the specimen is filled with martensitic layers. The elastic strain energy density created by the creation of the martensitic phase [111, 112] is minimized by this shape, which makes a large internal stress field that aids the initiation and growth of the new martensitic phase.



**Figure 4.2: Evolution of the martensitic variants for the martensitic embryo resided in four specific points (Model 4.1), the stress  $\sigma_1$ , and the von Mises stress. Rows (A)-(G) correspond to times 70 ms, 80 ms, 85 ms, 90 ms, 100 ms, 150 ms, and 350 ms.**



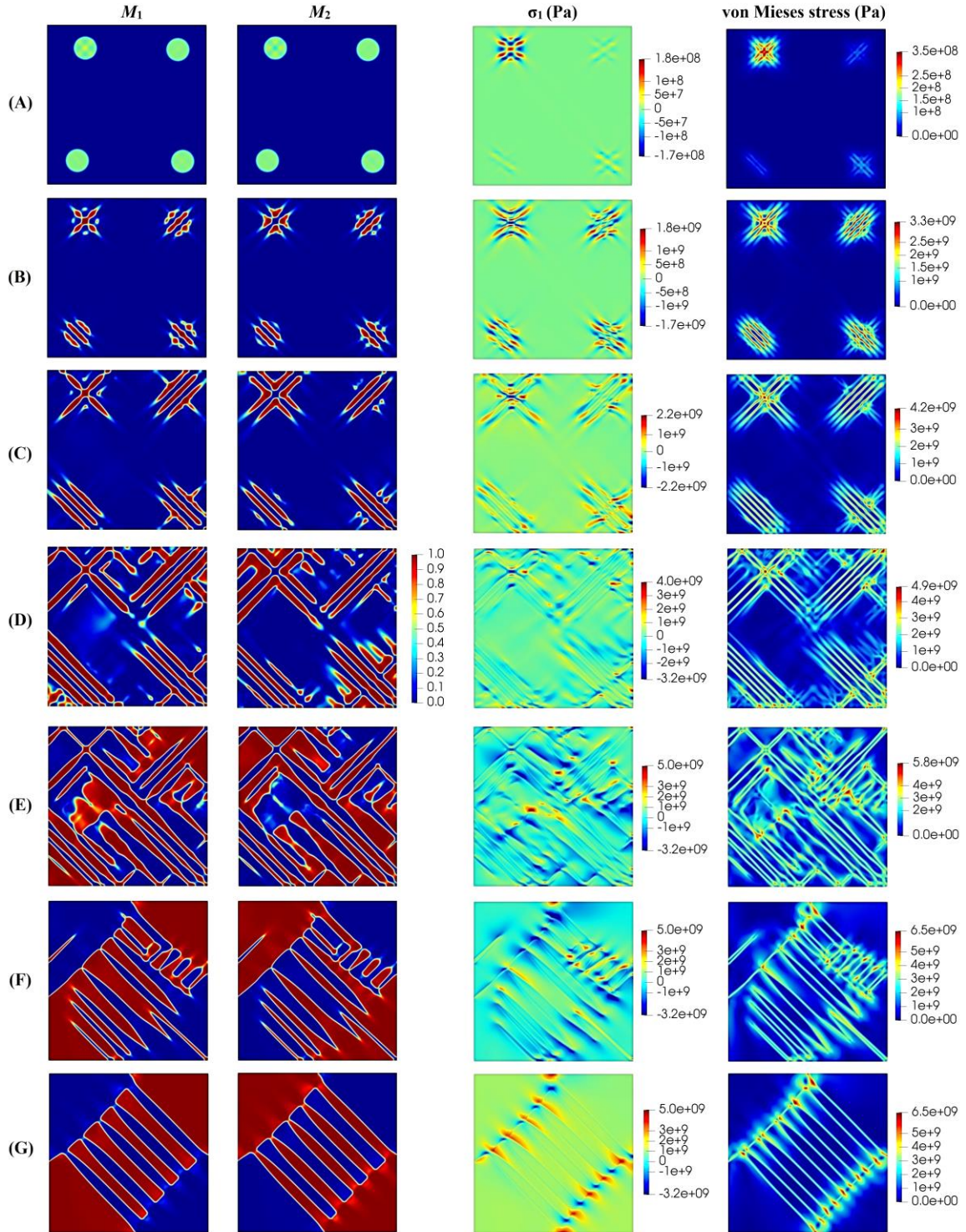


**Figure 4.3: Evolution of the martensitic variants for the martensitic embryo resided in four specific points (Model 4.2), the stress  $\sigma_1$ , and the von Mises stress. Rows (A)-(G) correspond to times 70 ms, 80 ms, 85 ms, 90 ms, 100 ms, 150 ms, and 350 ms**

Fig. 4.4 shows the evolution of the microstructure randomly distributed initial order parameters. The nodal values of the initial order parameters ( $0 < c_1, c_2 < 1$ ) at each node of the finite element mesh are assigned random numbers between zero and unity.



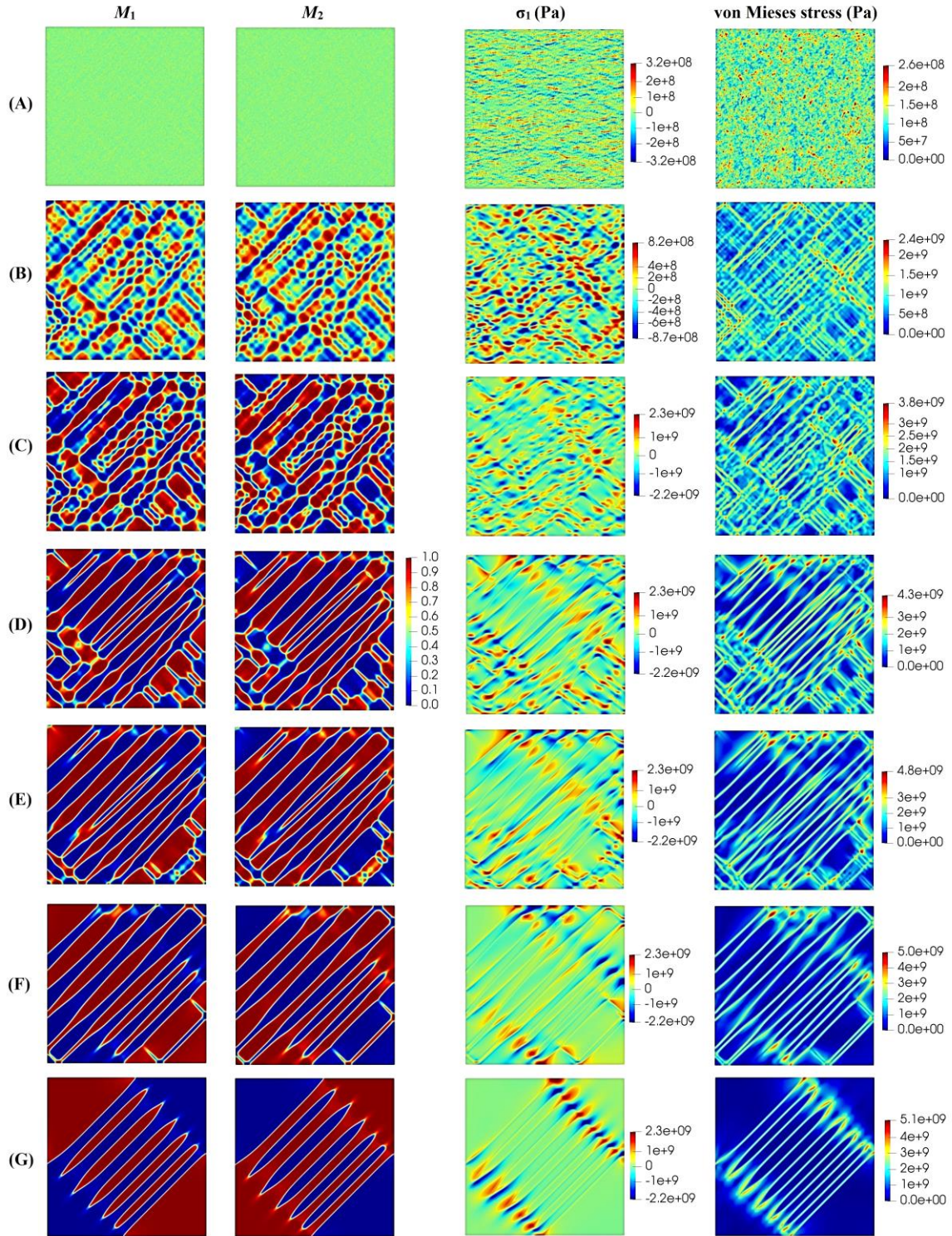


**Figure 4.4: Evolution of the martensitic variants for the martensitic embryo randomly distributed throughout the specimen (Model 4.3), the stress  $\sigma_1$ , and the von Mises stress. Rows (A)-(G) correspond to times 0 ms, 7 ms, 12 ms, 26 ms, 50 ms, 100 ms, and 350 ms.**

As shown in the diagram, the randomly distributed initial order parameters represent complex martensitic plates at stage B, followed by the thickening of martensitic plates aligned at  $45^\circ$  to



coordinate axes throughout stages (C)-(D) (G). It is worth noting that the von Mises stress in the final stationary microstructure for Model 4.3 follows a pattern that is extremely similar to that of Model 4.2.

The volume fraction of each martensitic variant,  $M_1$  or  $M_2$  is defined as follows for a better understanding and analysis of the MPT evolution rate in the microstructure.

$$\text{Volume phase fraction} = \frac{\text{Number of nodes at which } c_i = 1}{\text{Total number of nodes}} \quad (4.2)$$

When a fine-uniform mesh is used for the finite element method, this formula provides suitable estimates of volume fractions. For three different models, Fig. 4.5 shows the change in the volume percentage of the martensitic phases,  $M_1$  and  $M_2$ . As shown in the figure, the concentration of both martensitic phases rises dramatically in all models of martensitic embryos. Model 4.3 has sharp growth; however, it is followed by a relatively linear variation until it hits a plateau. Furthermore, in Model 4.3, the growth rate of both martensitic types is significantly faster than in Models 4.1 and 4.2.

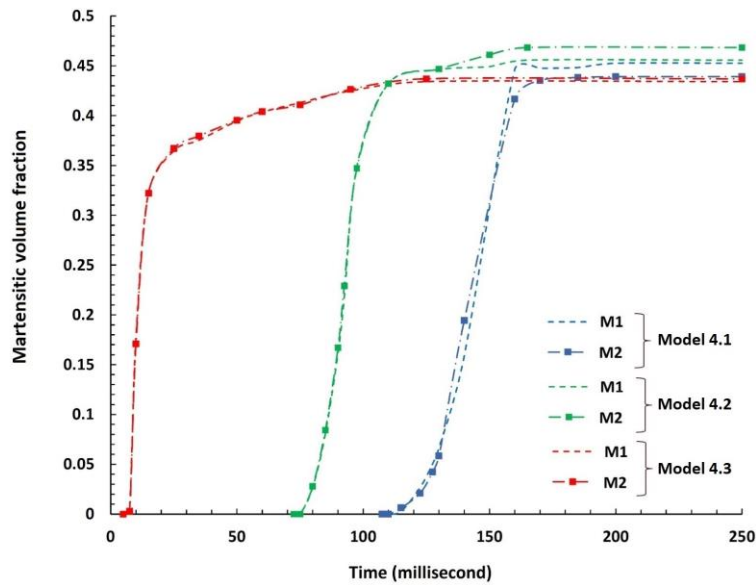


Figure 4.5: Variation of the volume fraction of the martensitic phases,  $M_1$  and  $M_2$  for the three models

Another thing to note is that the difference between the volume fractions of martensitic variants in Model 4.3 is significantly lower than in Models 4.1 and 4.2. Furthermore, in Model 4.3, the growth rate of both martensitic types is considerably faster than in Models 4.1 and 4.2. Another Fig. 4.6 shows how the volume fraction of the austenite phase varies for three different models. Compared to Models 4.1 to 4.3, it can be inferred that the volume fraction of austenite in Model 4.2 at the final stationary state is the lowest.

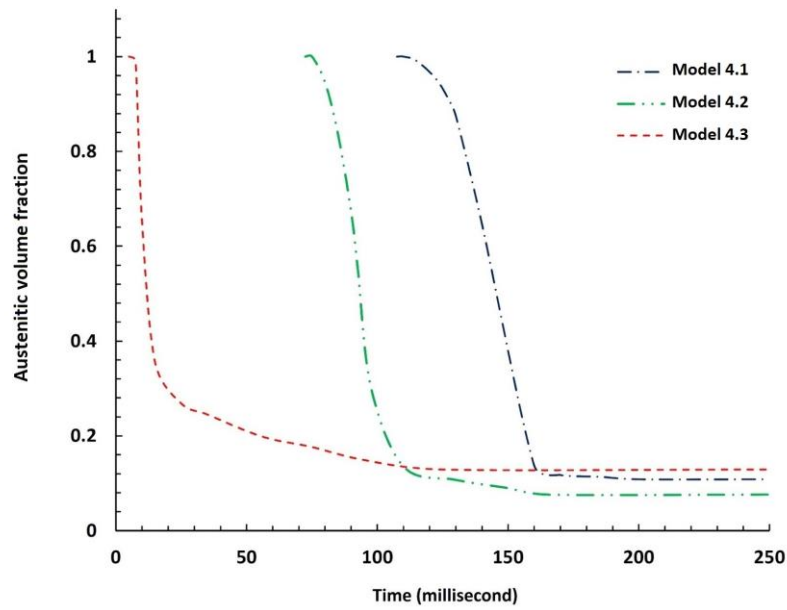
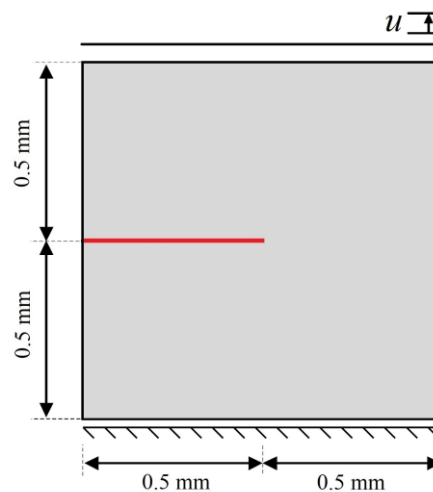


Figure 4.6: Variation of volume fraction of austenite phase for three different models.

#### 4.1.2 Crack initiation and propagation

This section of the simulation originated from the formulation in section 3.3. Because of the lack of proper experimental results for the crack nucleation and propagation in martensitic microstructures for direct comparison, the results obtained for a two-dimensional square plate under uniaxial (mode I) tension loading, as shown in Model 4.4 (Fig. 4.7), are compared with those available in the literature.



Model 4.4

Figure 4.7: Configuration of the specimen with a pre-existing crack based on ref [87, 94]

A vertical displacement at the top surface in the  $y$ -direction is applied to the specimen to simulate a pure mode-I fracture with a displacement  $u = 5 \times 10^{-3}$  mm to failure of the specimen. Fig. 4.8 schematically shows the progress of the crack through the part. Fig. 4.9 compares the load-displacement curve based on the present formulation of those from Refs [87, 94]. Note that in the current model, a uniform mesh with 57,600 4-node quadrilateral elements has been employed while 22,500 and 12,735 4-node quadrilateral elements have been used in Ref. [87] and Ref. [94], respectively. In addition, the length scale parameter is set to 0.015 mm. From Fig. 4.9, one can see that a good agreement exists between the results of the present method and those obtained in Refs. [87, 94].

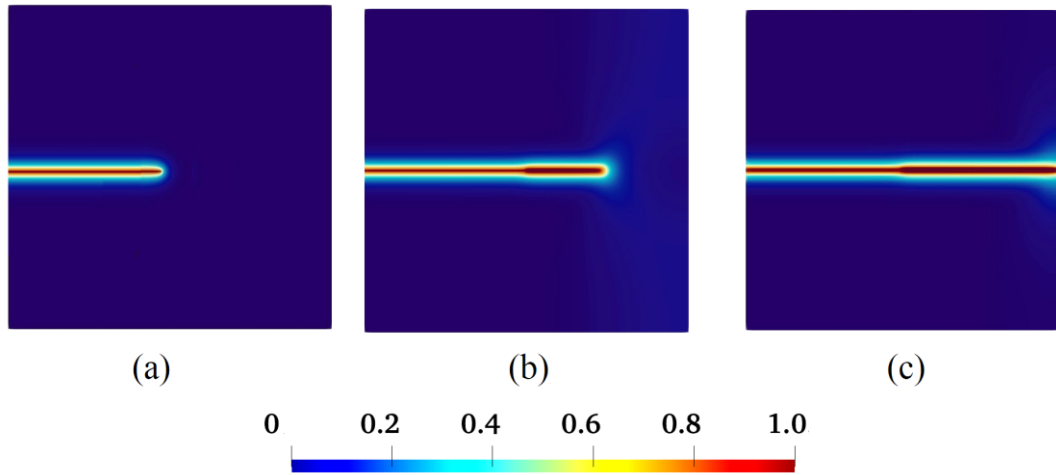


Figure 4.8: Growth of the crack in the specimen with the initial crack according to Model 4.4

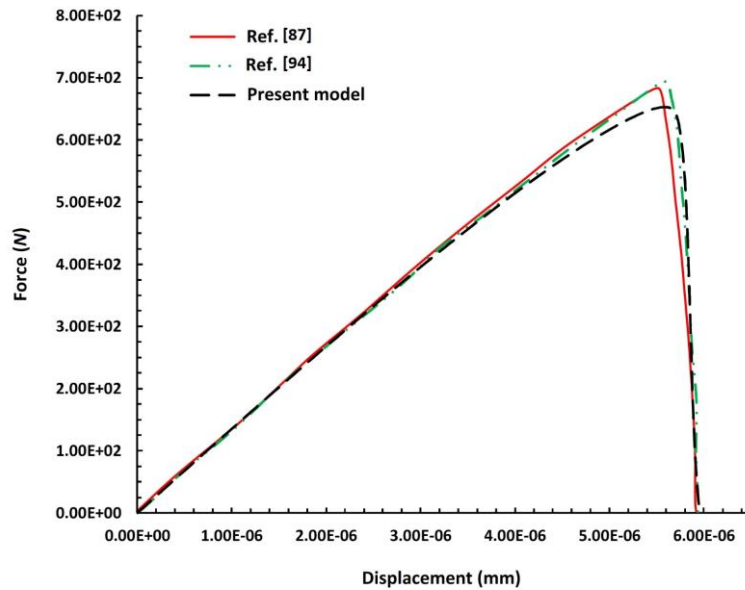
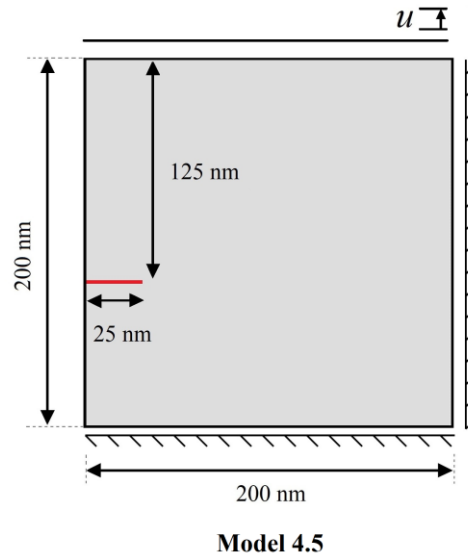


Figure 4.9: Load-displacement curve of an edge crack plate subjected to mode-I tension load.

In the following section, attention has been turned to the initiation and propagation of a crack in the martensitic specimen resulting from the previous section, both with and without an initial crack. This section considers the fracture energy  $G_s = 0.2 \text{ J/m}^2$ , the crack width  $L_s = 2 \text{ nm}$  and the mobility factor  $M_s = 1.0 \cdot 10^{12} \text{ (J}^3/\text{ms)}$ . Additionally, the bulk and shear moduli have been provided as the same as in the previous section. The model configuration with the initial crack is shown in Fig. 4.10.



**Figure 4.10: Configuration of the specimen with a pre-existing crack under mode I loading**

Fig. 4.11 shows the evolution of the fracture field parameter,  $s$ , and, in general, the crack path in completely austenitic and martensitic microstructures according to three models. As can be seen, the crack in the completely austenitic case begins to grow from the initial crack and propagates in a pretty straight path under mode I load. Nonetheless, due to residual stresses generated in the microstructure as a result of MPT, the fracture path in the martensitic microstructure indicates a significant oscillation.

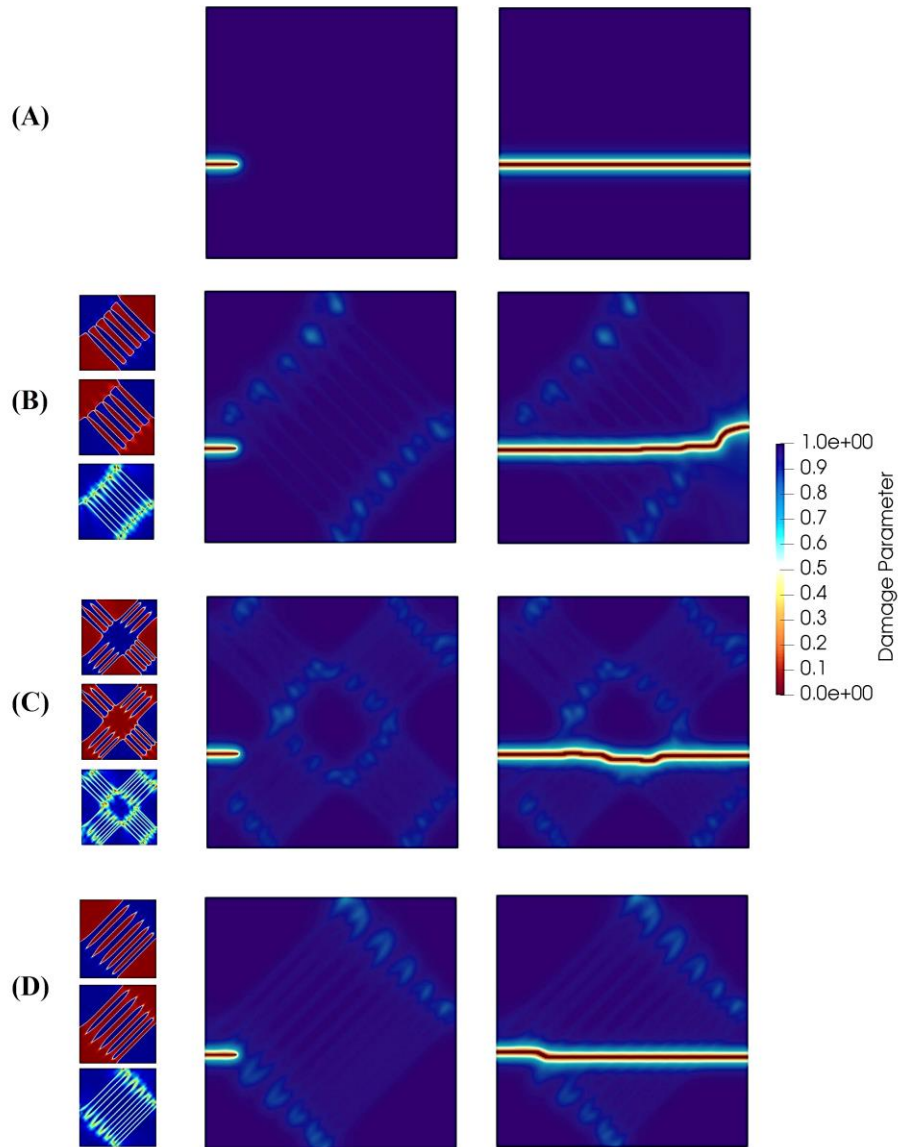


**Figure 4.11: Growth of a crack in the specimen with initial crack: fully austenitic specimen (a), martensitic specimen according to Model 4.1 (B), Model 4.2 (C), and Model 4.3 (D).**

Figs. 4.12, 4.13, and 4.14 show the onset and propagation of a crack in the martensitic microstructure without an initial crack, as determined by Models 4.1, 4.2, and 4.3. According to these figures, a fracture begins at the interface between martensitic variations with high von Mises stresses and propagates in a direction with significantly high residual stresses generated in the martensitic microstructure. However, in Model 4.2 and Model 4.3, this direction is upward and downward, respectively. Furthermore, the fracture in Model 4.1 has a completely different orientation than the cracks in other models, first continuing a reasonably straight course upward before turning into the specimen center, where higher values of the von Mises stress are found.

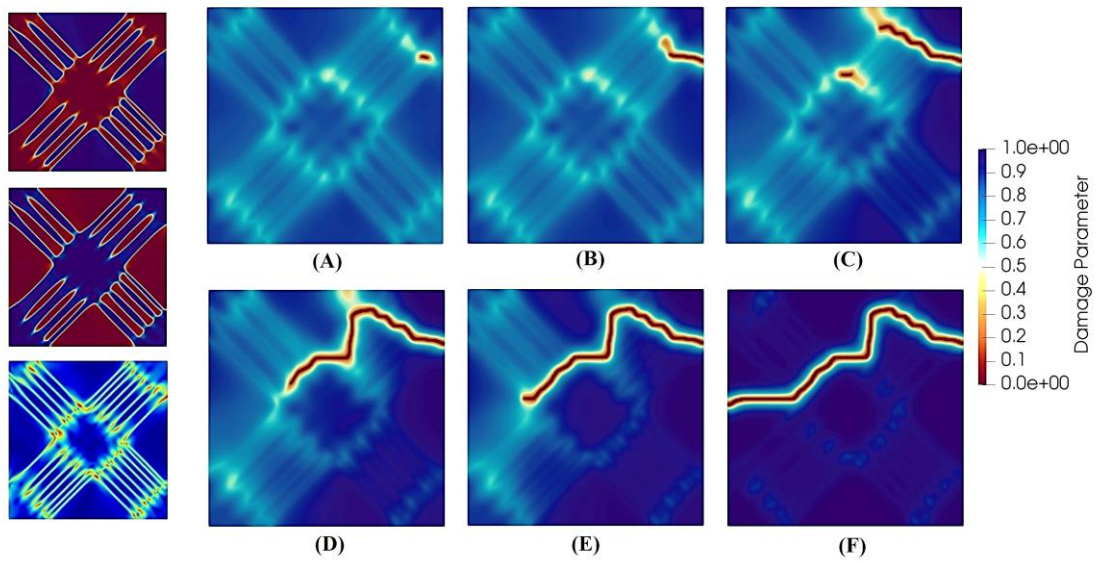


Figure 4.12: Initiation and propagation of a crack in the martensitic specimen without initial crack according to Model 4.1.

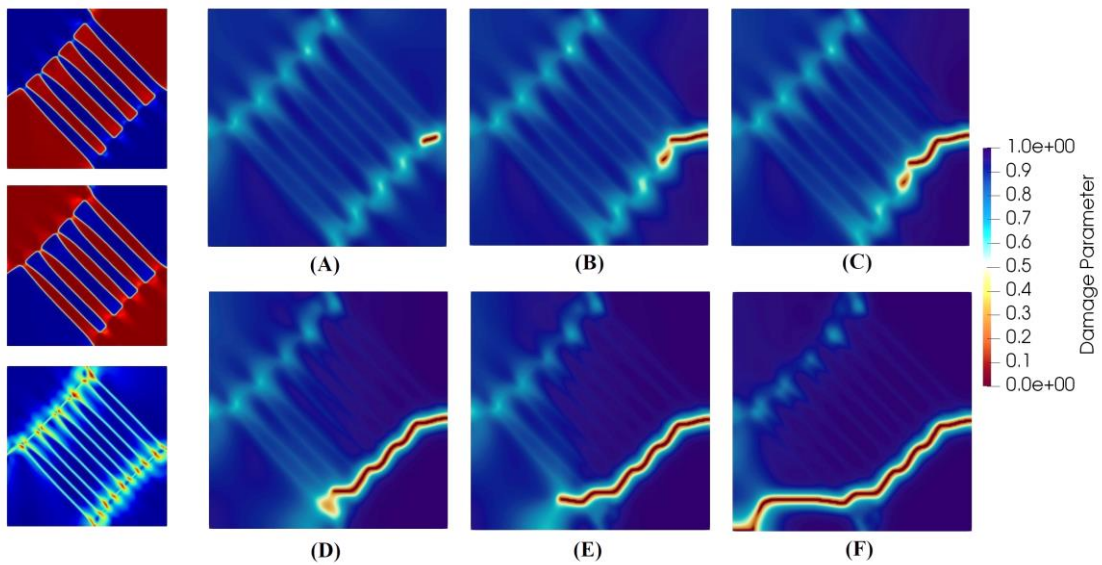
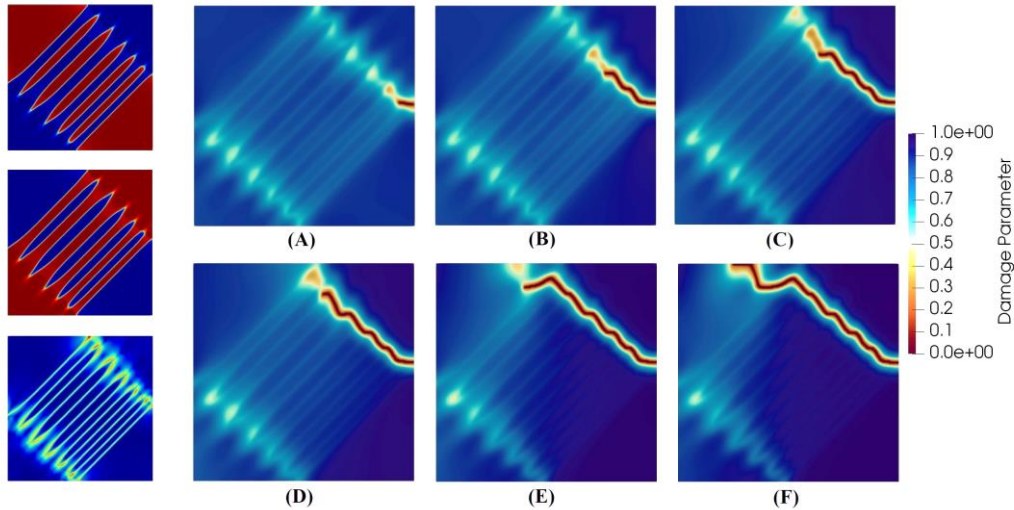


Figure 4.13: Onset and propagation of a crack in the martensitic specimen without initial crack according to Model 4.2.





**Figure 4.14: Initiation and growth of a crack in the martensitic specimen without initial crack according to Model 4.3.**

In this section of the work, an uncoupled PFA-based computational framework was proposed to model crack initiation and propagation in a martensitic microstructure generated by MPT. First, a FEM based on micro-elasticity theory was used to solve a coupled system of the TDGL problem and the quasi-static equation. The evolution of martensitic multi-variant distributions has been examined using three types of pre-existing martensitic embryos: (i) placed in the specimen center (Model 4.1), (ii) resided in four specified spots (Model 4.2), and (iii) randomly distributed throughout the specimen (Model 4.3). Afterward, a damage variable was included in the MPT model to investigate the initiation and growth of a crack in the obtained martensitic specimen, both with and without a pre-existing crack. The main findings are summarized as follows:

- First, a dramatic increase in the concentration of both martensitic phases is observed during the evolution of martensitic variants in all models of martensitic embryos. However, in the model with initially randomly distributed embryos (Model 4.3), a partly linear variation follows this sharp increase until it reaches a plateau.
- The findings revealed that the growth rate of both martensitic variants in Model 4.3 is significantly faster than in Models 4.1 and 4.2. Furthermore, the difference in volume fraction of martensitic variants in Model 4.3 is noticeably lower than in Models 4.1 and 4.2.
- It can be concluded that the volume fraction of austenite in Model 4.2 at the final stationary state is the lowest compared to Models 4.1 and 4.3.
- The results indicate that when a martensitic microstructure with a pre-existing crack is loaded in mode I, the crack grows from the initial crack and propagates along a

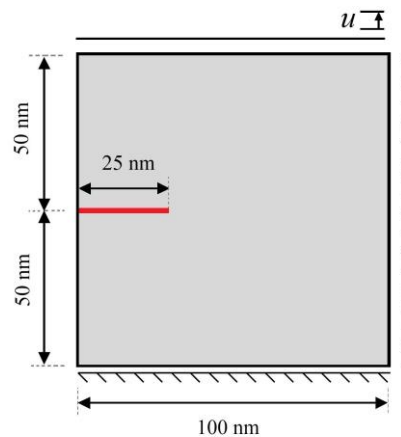
relatively straight course. However, the fracture path in the martensitic microstructure reveals a slight variability as a result of residual stresses induced by MPT.

- It has been concluded that in the absence of an initial crack in the martensitic microstructure, a crack nucleates at the interface between martensitic variants with high von Mises stresses and propagates in a direction characterized by significantly high residual stresses generated in the martensitic microstructure.

## 4.2 The coupled phase field approach of martensitic phase transformation and fracture

### 4.2.1 The one variant of martensitic transformation coupled with fracture (verification of the model)

The findings in this section have been based on the formulation in section 3.4. The validation of the present formulation for one-variant MPT is presented first in this section. Following that, the PF model is applied to a two-variant MPT and fracture in a microstructure with an initial crack, and the results are discussed in detail. Due to a lack of experimental results on crack initiation and growth in microstructures subjected to one-variant MPT, the results obtained for an austenitic plate under mode I loading are compared to those provided [31]. A vertical displacement in the y-direction is applied to the specimen top and bottom edges to simulate a pure Mode I fracture, as seen in Fig. 4.15. The material which has been used is the same material in section 4.1 (Fe–31 at.% Ni).



Model 4.6

**Figure 4.15: Initial configuration of an austenitic specimen with a pre-existing crack under mode I loading is used for validation of the work**

In Fig. 4.2, the evolution of the one-variant martensite phase and crack growth behavior obtained in Ref. [31] are compared to those obtained in this work. As can be seen, there is a good agreement between the results obtained using this method and those obtained using Ref.



[31]. As the figure shows, the crack does not grow straight through the specimen but kinks and propagates vertically. Additionally, it is seen that fracture growth commences once the single-variant martensite phase has propagated through the specimen completely.

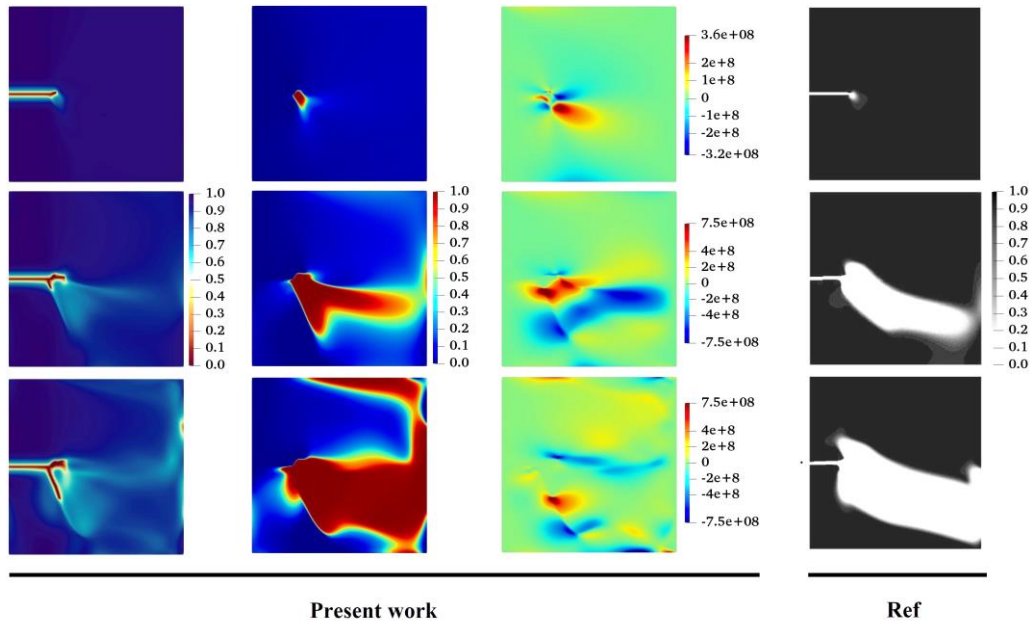


Figure 4.16: Contour plots of evolution of damage variable, martensite variant, and corresponding  $\sigma_{11}$ -component in a coupled problem of one-variant MPT and fracture

#### 4.2.2 The Two-martensitic variants transformation coupled with fracture

In the second example, a square domain with a dimension of 100 nm  $\times$  100 nm is considered, discretized using 161,604 linear 4-node elements, as illustrated in Fig. 4.17. The same material as section 4.1 has been considered.

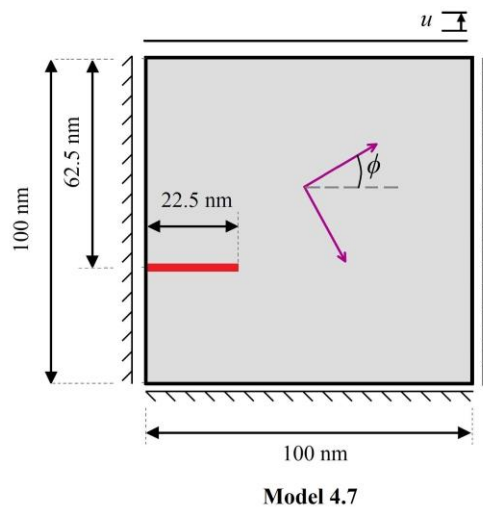


Figure 4.17: Schematic representation of a specimen with an initial crack under Mode I loading

In this case, a transfer operation of the tensorial quantities between the crystal local coordinates and the global coordinate system is required to investigate the effect of different crystal lattice orientations on martensitic variants and crack behavior. The stress-free strain is transformed into the global coordinate system using the rotation operations given by

$$\boldsymbol{\varepsilon}_i^0 = \mathbf{R}_{ik} \mathbf{R}_{jl} \boldsymbol{\varepsilon}_i^{00} \quad (4.3)$$

where  $R_{ik}$  denotes a rotation tensor which, for a grain having an orientation angle  $\phi$  is defined by

$$\mathbf{R}_{ij} = \begin{bmatrix} \cos \phi & \sin \phi \\ -\sin \phi & \cos \phi \end{bmatrix} \quad (4.4)$$

and  $\boldsymbol{\varepsilon}_i^{00}$  is the eigen strain tensor, which is for the martensite variants with a lattice orientation angle of  $45^\circ$  (Eq. 4.1).

Fig. 4.18 depicts the evolution of two martensite variants in an austenitic microstructure with a crystal lattice orientation of  $15^\circ$  prior to fracture propagation. As shown in this diagram, the fracture growth does not begin until MPT has grown almost fully through the microstructure. To understand this phenomenon, take into account that the energy required for MPT is provided by external tension loading prior to the propagation of the fracture in the austenitic specimen. External loading and chemical driving force, in other words, are superior to elastic energy and gradient energy. Conversely, MPT dissipates energy, which is not available for fracture propagation as a result. When martensitic plates develop across the microstructure's width, the elastic energy, which increases due to eigenstrain, can be reduced on the micro-level when the microstructure deforms. The crack tip is then subjected to extra stresses, including shear loading, as a result of the microstructure deformation, resulting in crack propagation.

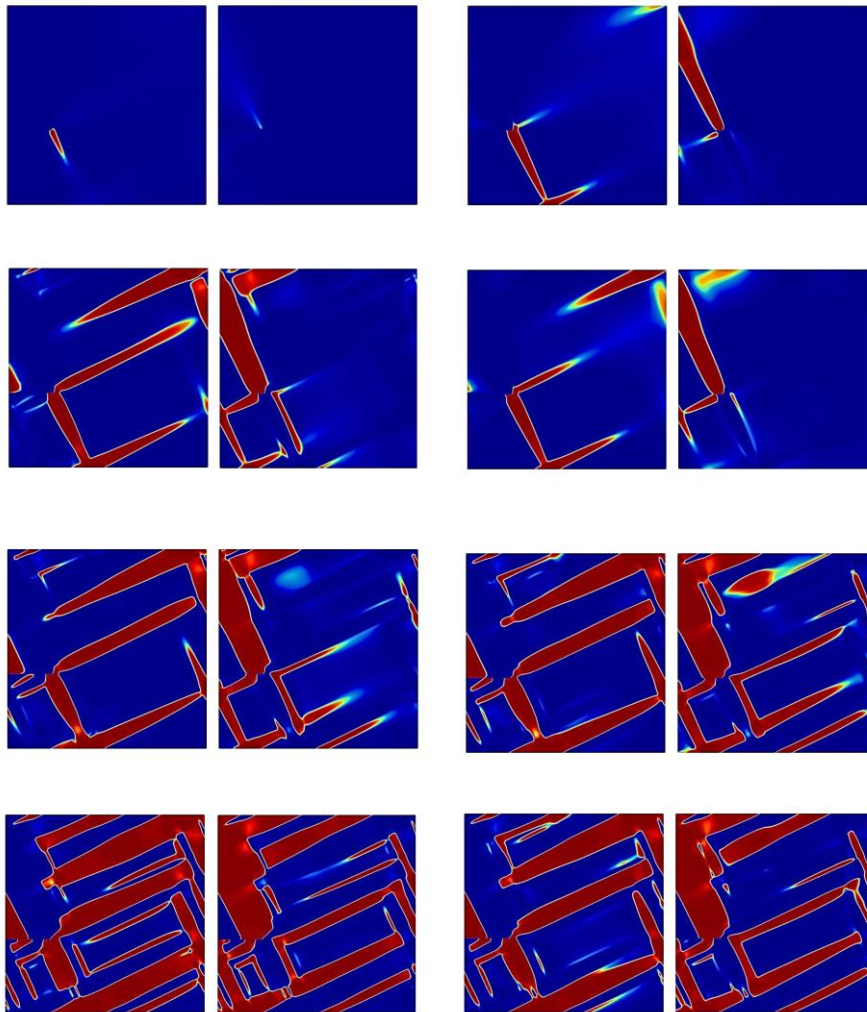


**Figure 4.18: Evolution of two martensite variants prior to crack propagation in the austenitic microstructure with crystal lattice orientation of  $15^\circ$**

Under Mode I loading with a crystal lattice orientation of  $15^\circ$ , Fig. 4.19 shows the growth of the initial crack and the evolution of martensite variants in the austenitic microstructure. Due to the high-stress concentration at the initial fracture tip, MPT occurs in the area in front of the crack tip in the initial state by applying the loading, as seen in this figure. Mamivand et al. [22] observed a similar tendency near the fracture tip in tetragonal-to-monoclinic MPT. Following the initial production of martensite variants, the initial fracture propagates in such a way that the martensite variant formation characteristics, the orientation and direction of the martensite plates, and the stress concentration between martensite plates mostly influence its path. As shown in Fig. 4.19, the stress concentration ahead of the crack tip affects the evolution of martensite variants. On the other hand, the direction of the crack propagation changes when plate-like martensite forms ahead of the crack tip. Notably, the crack tends to propagate across martensite layers, with a larger von Mises stress than other places.

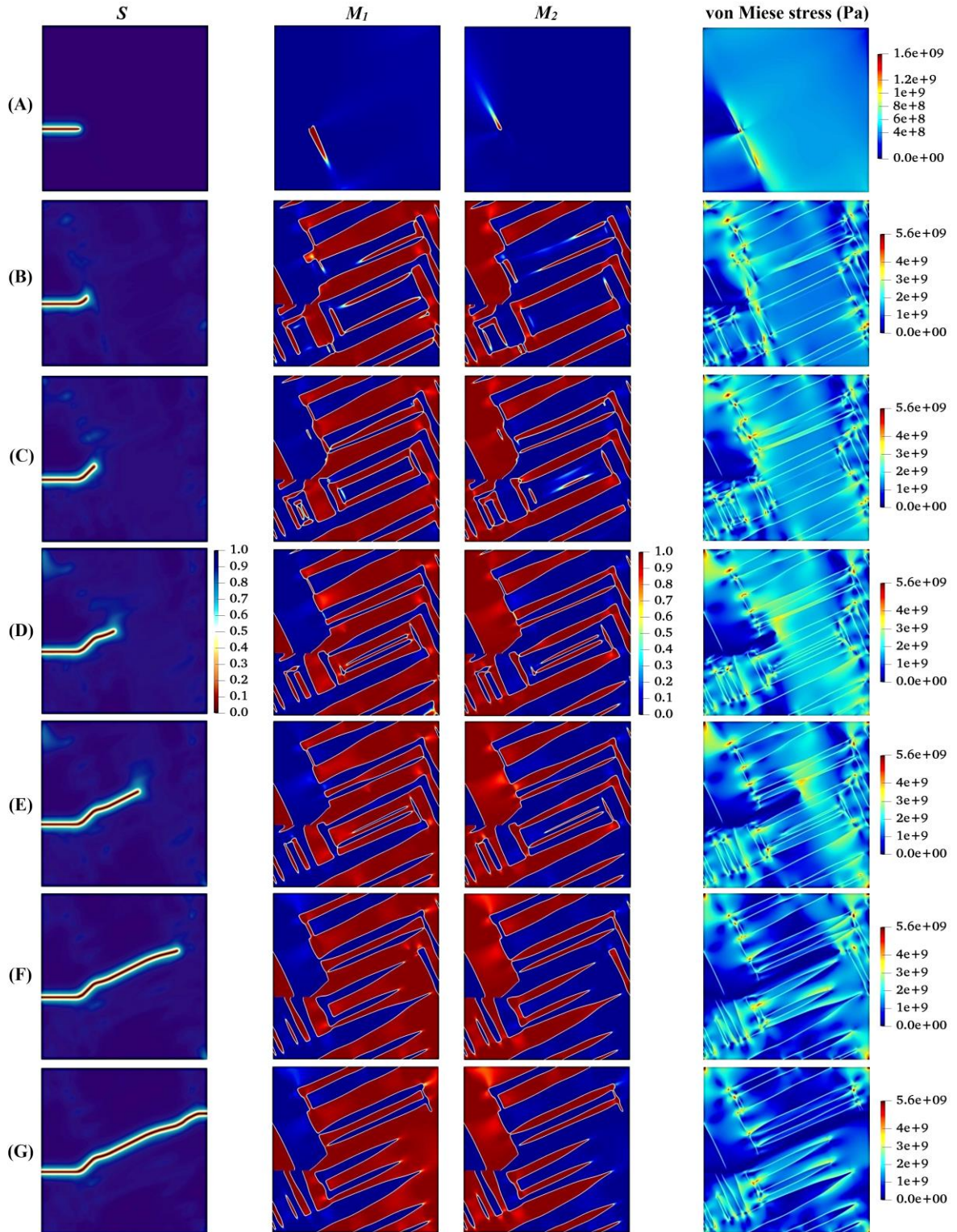


Figure 4.19: Evolution of damage variable, two martensite variants, and von Mises stress in the austenitic microstructure under Mode I loading with crystal lattice orientation of  $15^\circ$



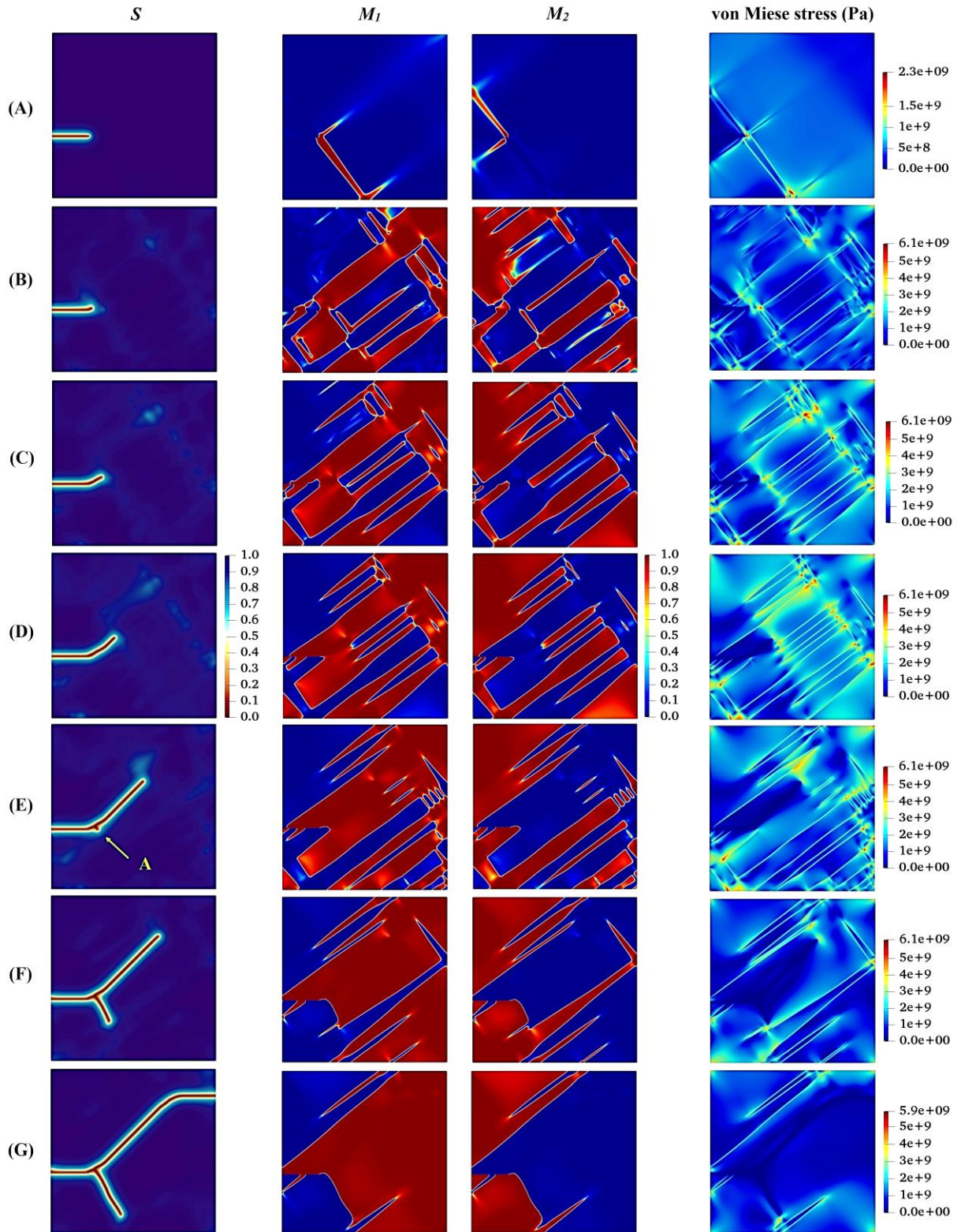


Figure 4.20: Evolution of damage variable, two martensite variants, and von Mises stress in the austenitic microstructure with crystal lattice orientation of  $30^\circ$

The following presents the crack propagation behavior and martensite variants evaluations for four different lattice orientation angles of  $30^{\circ}$ ,  $45^{\circ}$ ,  $60^{\circ}$ , and  $90^{\circ}$  in Figs. 4.20 to 4.23 and compared with those with the lattice orientation angle of  $15^{\circ}$ . It can be inferred from Fig. 4.20 that as the crack propagates between layers of two martensite variants, it results from high-stress concentration at the intersection of martensite variants on the crack surface at point A, and crack-branching takes place.

In Fig. 4.21, the microstructure with the lattice orientation angle of  $45^{\circ}$  shows the fracture propagation behavior of the microstructure. As seen in Fig. 4.22, a fracture generated by the lattice orientation angle of  $60^{\circ}$  depicts an entirely different behavior from other lattice orientation angles, following a rather straight path until the middle of the specimen. Another interesting point to mention is that the crack propagates with the martensite phase without reaching the boundary between the martensite variants, which coincides with the findings reported in the experimental work of Stolarz et al. [113].

It can be observed from Fig. 4.23 that the crack initially grows within the martensite phase and deviates towards the locations, adjacent to the crack tip, with high-stress concentrations. Afterward, the crack tends to propagate between martensite variants, and at the same time, due to the high-stress concentration formed at point A, as shown in Fig. 4.23.D, a new crack initiates and grows. Then, the two cracks approach each other irrespective of the boundary between martensite variants and eventually intersect each other.

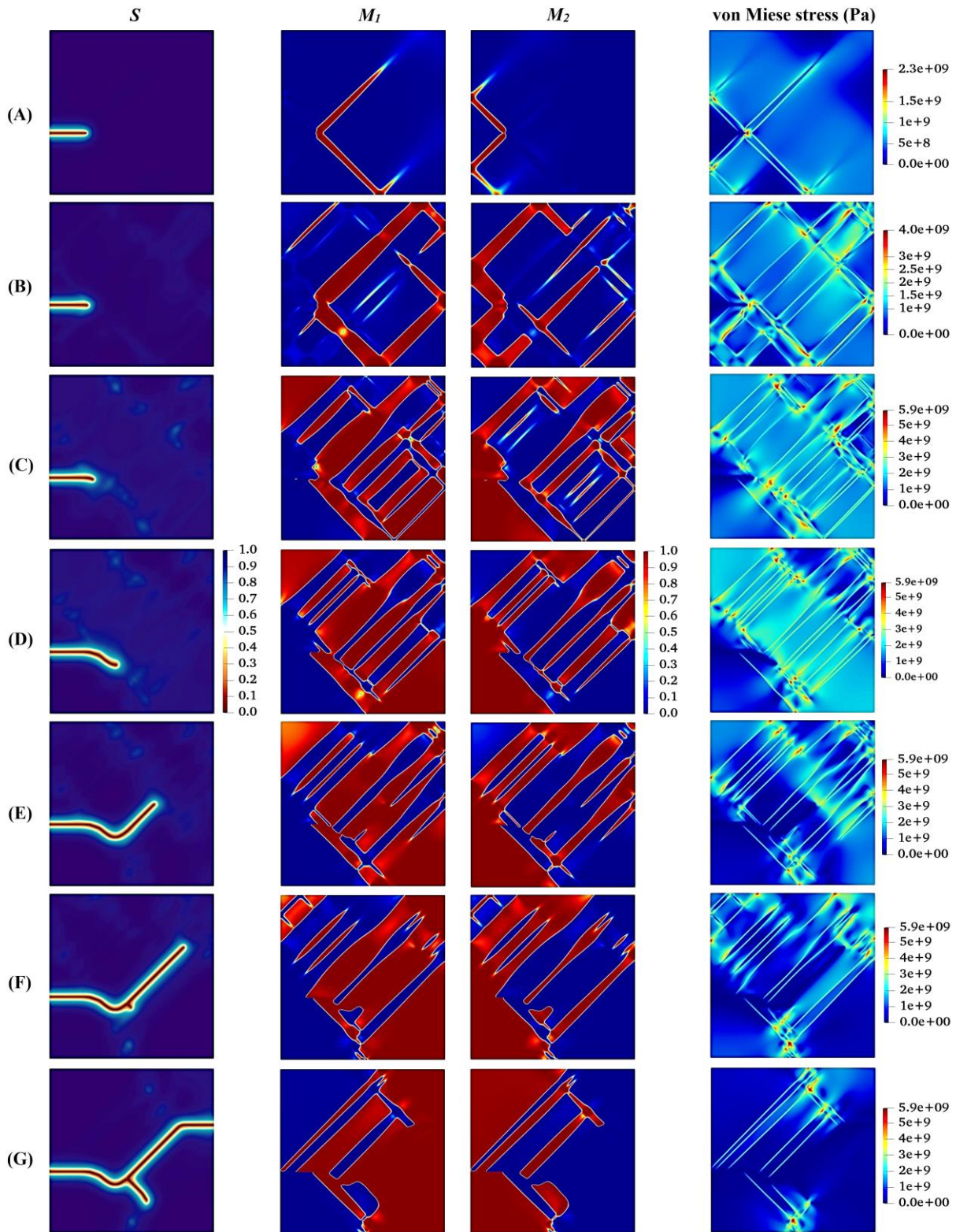


Figure 4.21: Evolution of damage variable, two martensite variants, and von Mises stress in the austenitic microstructure under Mode I loading with crystal lattice orientation of  $45^\circ$



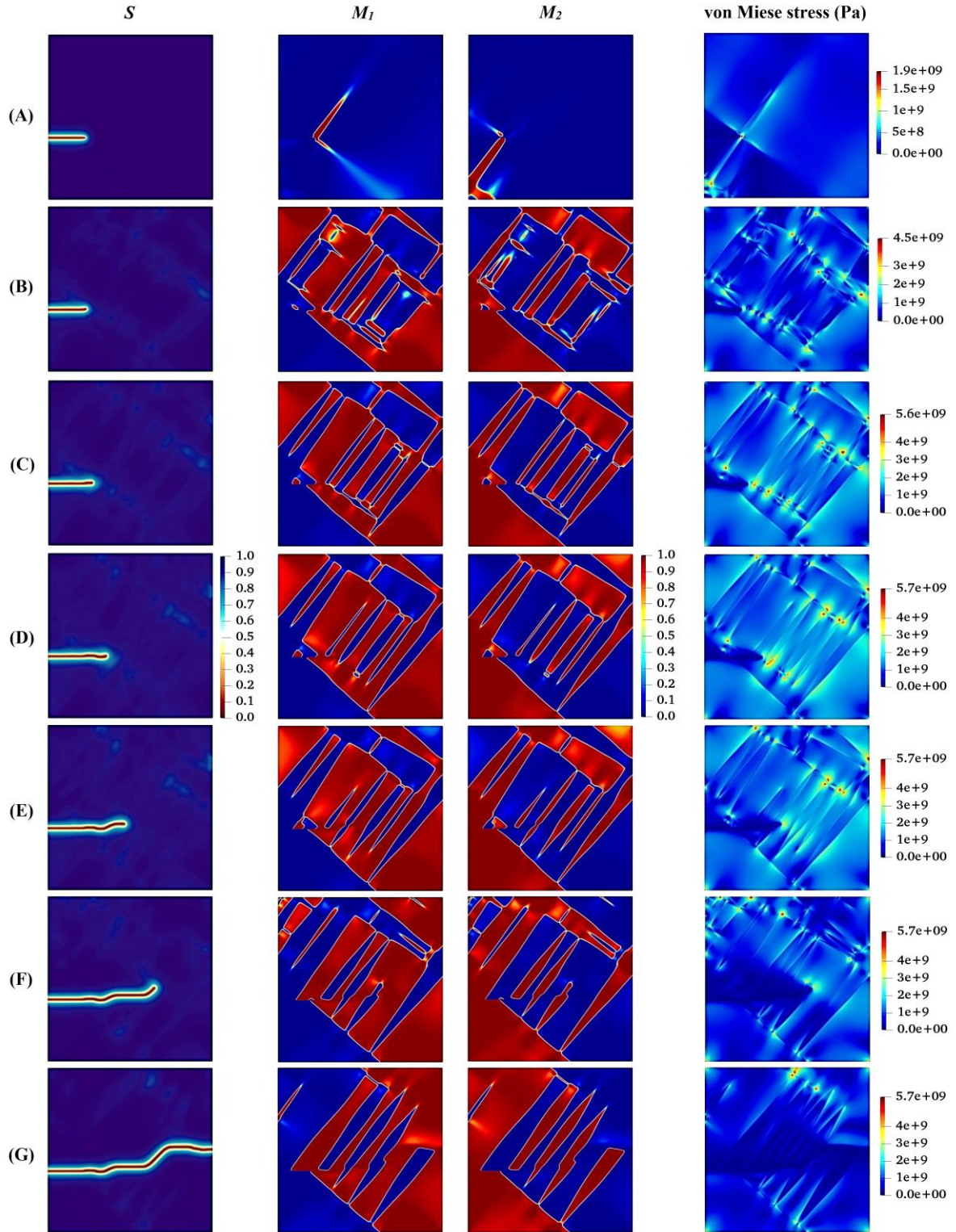


Figure 4.22: Evolution of damage variable, two martensite variants, and von Mises stress in the austenitic microstructure under Mode I loading with crystal lattice orientation of  $60^\circ$



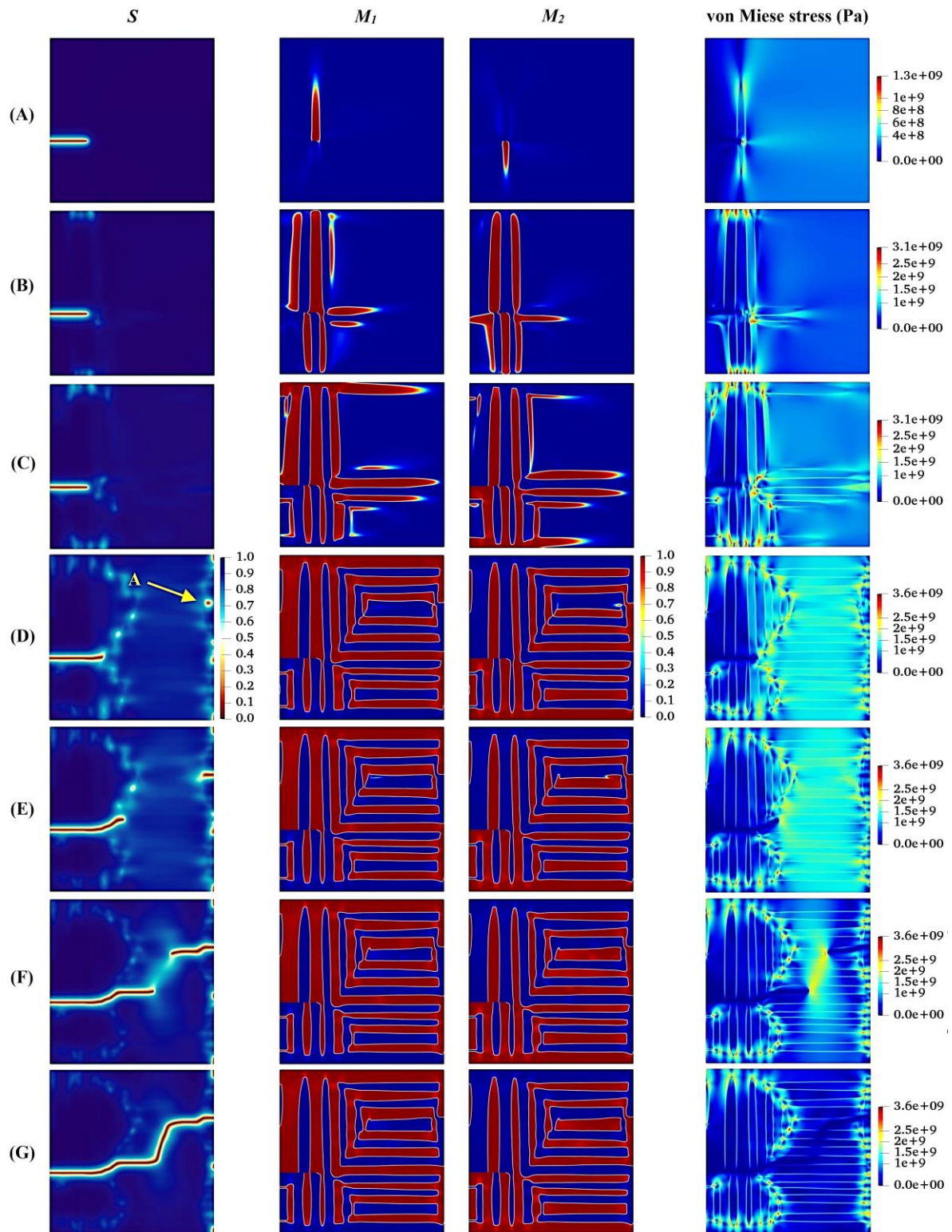


Figure 4.23: Evolution of damage variable, two martensite variants, and von Mises stress in the austenitic microstructure with crystal lattice orientation of  $90^\circ$

### 4.2.3 The coupled martensitic transformation and fracture in view of geometrical inhomogeneities

In this section, another type of condition that leads to material failure is discussed. Fracture most often occurs in materials due to geometrical inhomogeneities [114]. In this case, there may be geometric imperfections in the structure, such as porosity which, by causing a stress concentration in certain locations, lead the crack to the onset and propagate through the material until eventual failure [115,116]. In problems such as the one in which the failure is completely coupled by phase transformation, the inhomogeneity can also play a role as an initiator areas of phase change. As a result of the high-stress concentration in these areas, a significant stress field is formed, which supplies the energy required to phase transformation during a stress-induced process [117].

Simultaneously with this phase change, as mentioned, crack also triggers in the material, and the behavior of fracture and phase transformation completely affect each other. In most cases, phase change and fracture begin in areas with high-stress concentrations and propagate throughout the material.

In this section, in order to better investigate the concepts, Model 4.8 (see Fig. 4.24) has been created. This model has a square geometric inhomogeneity in which the domain is loaded under the first failure mode and the boundary conditions are shown.

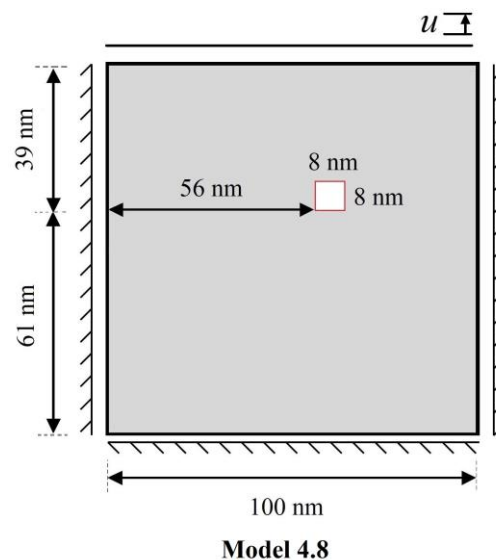


**Figure 4.24: Configuration of the specimen as a geometrical inhomogeneous structure under mode I**

Fig. 4.25.A depicts the beginning of the phase transformation in the vicinity of the square hole, which was subjected to high levels of stress concentration. The initial martensitic structure is formed as a result of a stress-induced martensitic transformation in the material. Cracks start appearing in the corners of this square and propagate outward from there. The cracks can deviate from their intended direction at any time, and this causes changes to the microstructure

of the material according to the arrangement of the martensitic layers and its internal stresses. Fig. 4.25.G shows the final step of fracture in the material and the final martensitic structure, which is completely different from its initial formation.

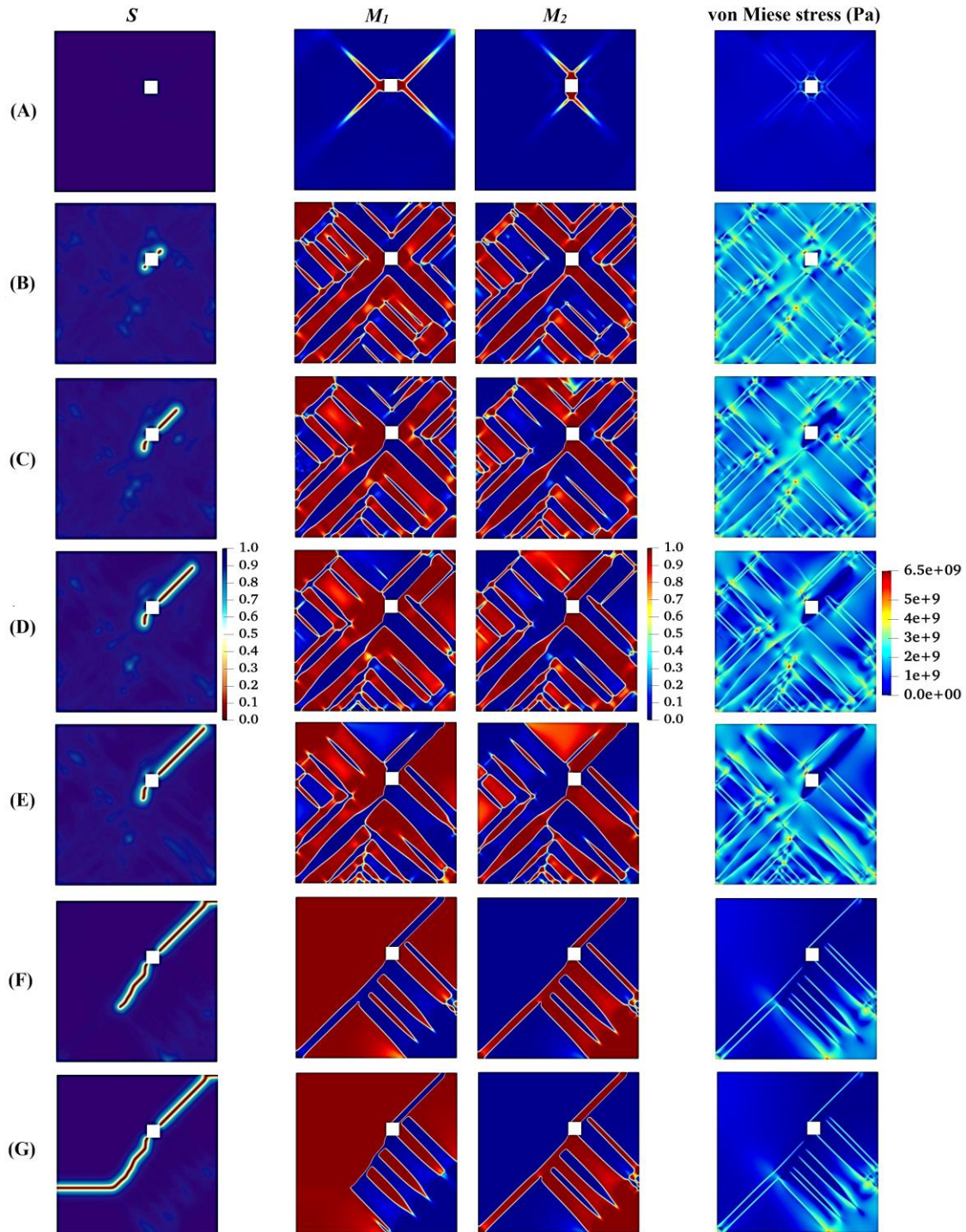


Figure 4.25: Evolution of damage variable, two martensite variants, and von Mises stress in the austenitic microstructure in the geometrical inhomogeneous structure



Fig. 4.26 graphically analyses the formation of martensite variants in the austenitic field. The first variant is the dominating variable in this structure, as shown in the diagram, always occupying a larger percentage of volume. Up to 150 milliseconds, both martensite variants have an ascending trend, with the first and second variants of martensite having a volume fraction of 48 and 35 percent, respectively.

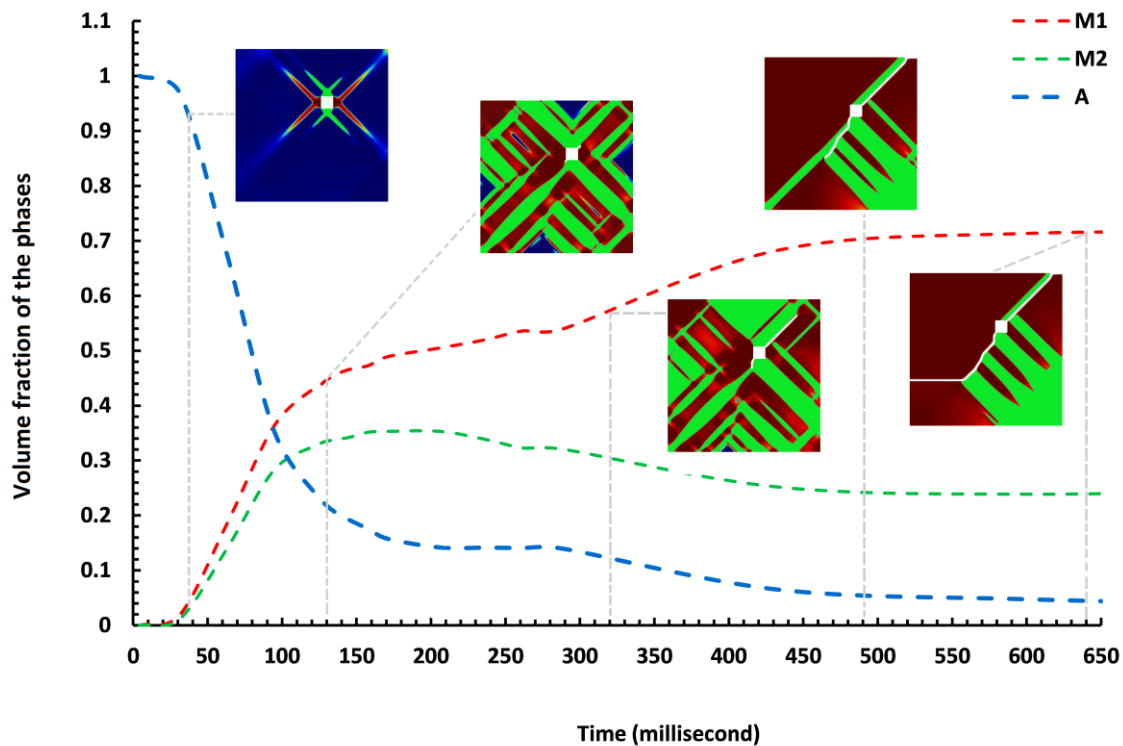


Figure 4.26: Variation of volume fraction of austenite and martensite phases for Model 4.5

After this period, the process of forming the second variable shifts downward, implying that the emergence of cracks in the material creates local stress, converting the second variant into the first. Gradually, the volumetric percentage of the second martensitic variant decreases, and at the end of the fully fractured structure, the first variant contains about 71% of the microstructure, which is about 26% for the second variant.

#### 4.2.4 The coupled martensitic transformation and fracture in polycrystalline structures

After studying the fracture behavior in areas with different martensitic orientations, the idea of working on polycrystalline problems came up. The polycrystalline forms of metals and ceramics are used in the majority of structural applications. Grain size and morphology, grain boundary character, lattice orientation, and defects that may segregate at boundaries or reside

within crystals are all factors that influence mechanical qualities, including hardness, strength, and ductility. Predicting material strength and failure by modeling damage and microcracking at the microscopic level is a significant task for studying the durability of structures more precisely. Numerous technical materials, including ceramics, alloys, rocks, and metals, are heterogeneous, consisting of an assembly of numerous unevenly shaped phases or crystallites that are randomly distributed. Microstructural aspects of polycrystalline materials, such as topology, orientation, and grain boundary characteristics, have a significant effect on both the failure causes and macroscopic mechanical response of these materials. Grain boundary interfaces have a substantial influence on properties as grain size decreases: as the surface area to volume ratio of such interfaces increases, the relative volume fraction of material adjacent to interfaces increases. In ceramics, grain boundaries frequently contain amorphous/glassy phases of material that exhibit properties distinct from those of the surrounding crystals [118-121].

Individual crystals are numerically resolved in continuum polycrystal models, which are helpful in studying possible connections between microstructure characteristics and mechanical response. Perhaps the most often utilized approach for simulating fracture over the last two decades has been cohesive finite element systems. Many numerical approaches have been developed to study the fracture of polycrystalline solids. Sukumar et al [122] utilized the XFEM to investigate the transition from intergranular to transgranular fracture by varying the fraction of toughness between the grain boundary and grain interior. Simulating fracture nucleation in XFEM, on the other hand, is a challenging endeavor. Furthermore, this technique necessitates the construction of level-set functions to define the crack, which can be time-consuming when interacting with several cracks and/or 3D implementation [123, 124].

Meanwhile, quantitative models have been developed to characterize the toughening effect of phase change in polycrystalline structures. It is generally known that the toughening effect is influenced by the transformation strains' dilatational and shear components [125-128]. Most quantitative theoretical models are based on a stress-based transformation criterion or macroscopic constitutive relations to predict geometric aspects of the transformation zone. The extra energy used owing to phase transformation or the change in the stress intensity factor is then evaluated to characterize the toughening effect.

In the continuation of this section, two polycrystalline models have been built to study the coupled approach of fracture and phase transformation. These structures are arranged completely randomly so that in each crystal there is the potential for the growth of martensitic layers at different angles, as seen in Fig. 4.27. In this investigation, the effects of the grain boundaries have not been considered as separated behaviors, which can be a good idea for future studies. To better examine the behavior of grain boundaries the PFA can even be combined with other numerical methods such as the cohesive zone method and XFEM.

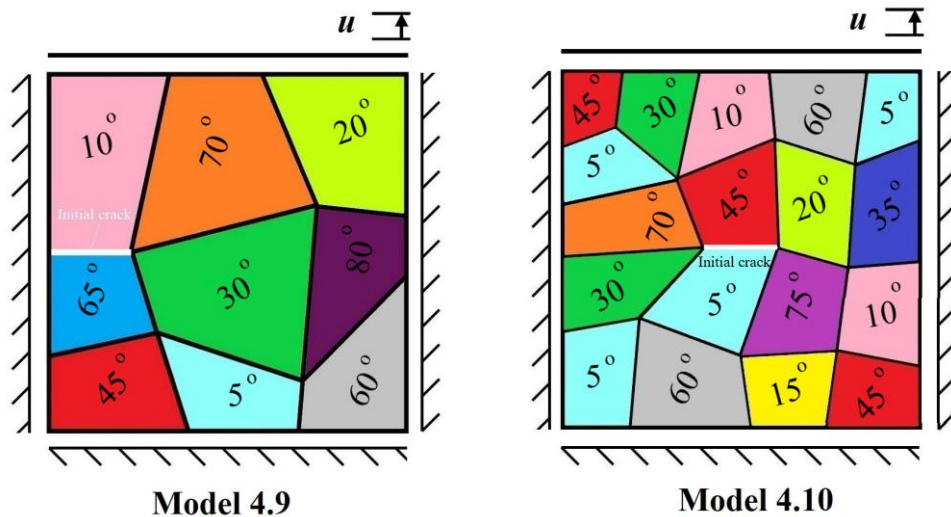


Figure 4.27: Configuration of the two polycrystalline specimens with a pre-existing crack under mode I

As shown in Figs. 4.28 and 4.29, the formation of martensitic layers begins under a stress-induced process from the crack tip. Each crystal provides a condition for the growth of martensitic layers at different angles, which are formed before the growth of cracks in the initial martensitic structure. After forming the initial martensitic structure in the material, the crack begins to propagate through the material. Crack growth depends on factors such as each crystal orientation, the arrangement of the martensitic layers, maximum stresses, and the stress concentration in the regions.

There will be noticeable changes in the creation of the new martensitic structure when crack growth begins. The martensitic variants can be converted to each other in areas subjected to stress. It is clear from Figs. 4.28 and 4.29 the final martensitic structure radically differs from the initial structure before the fracture effect. Another noteworthy feature is that the crack behavior, which is proportional to the arrangement of the martensitic layers, is always changing since the fracture is modifying the structure of the martensite at every moment.

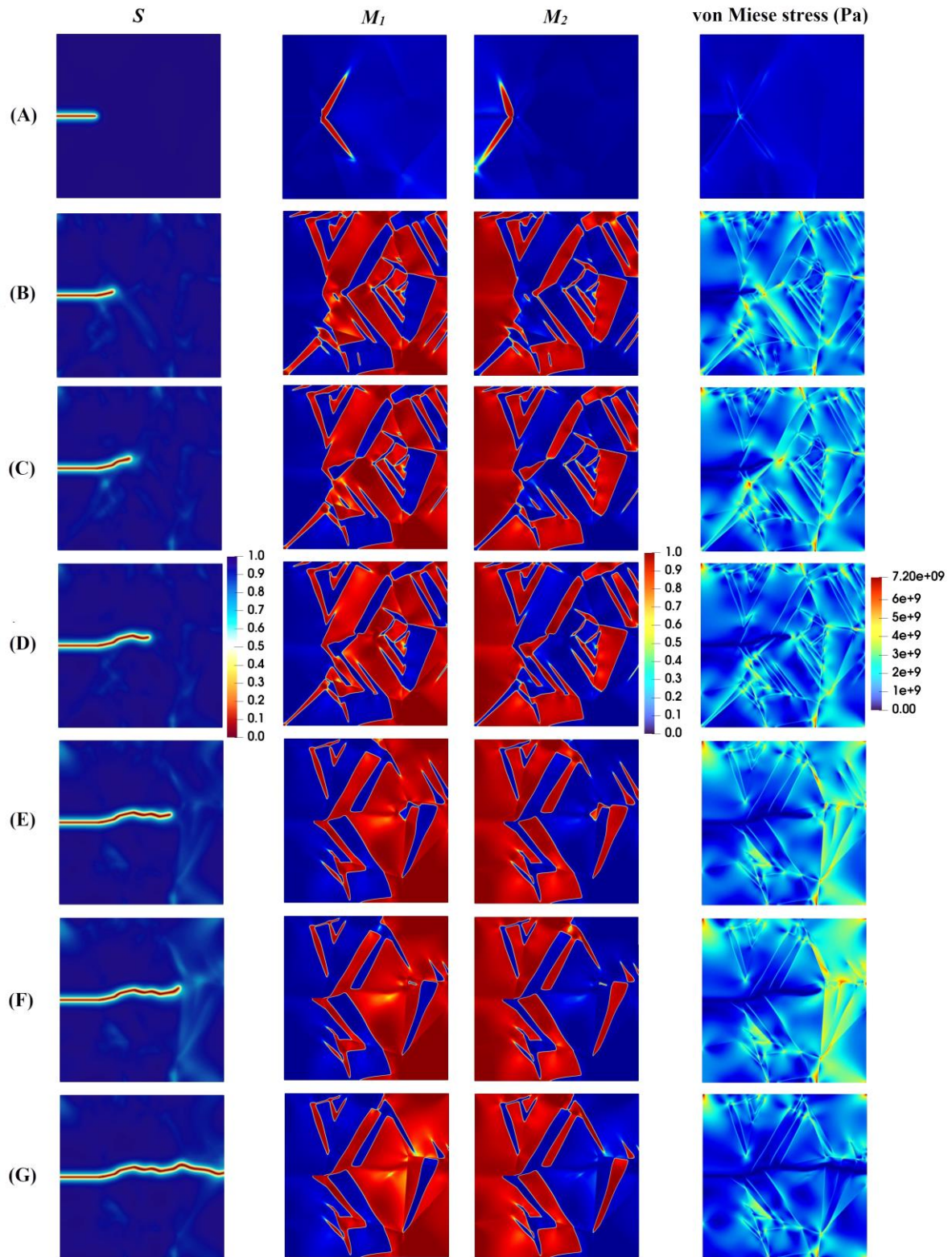


Figure 4.28: Evolution of damage variable, two martensite variants, and von Mises stress in the austenitic microstructure in the first polycrystalline structure according to Model 4.9



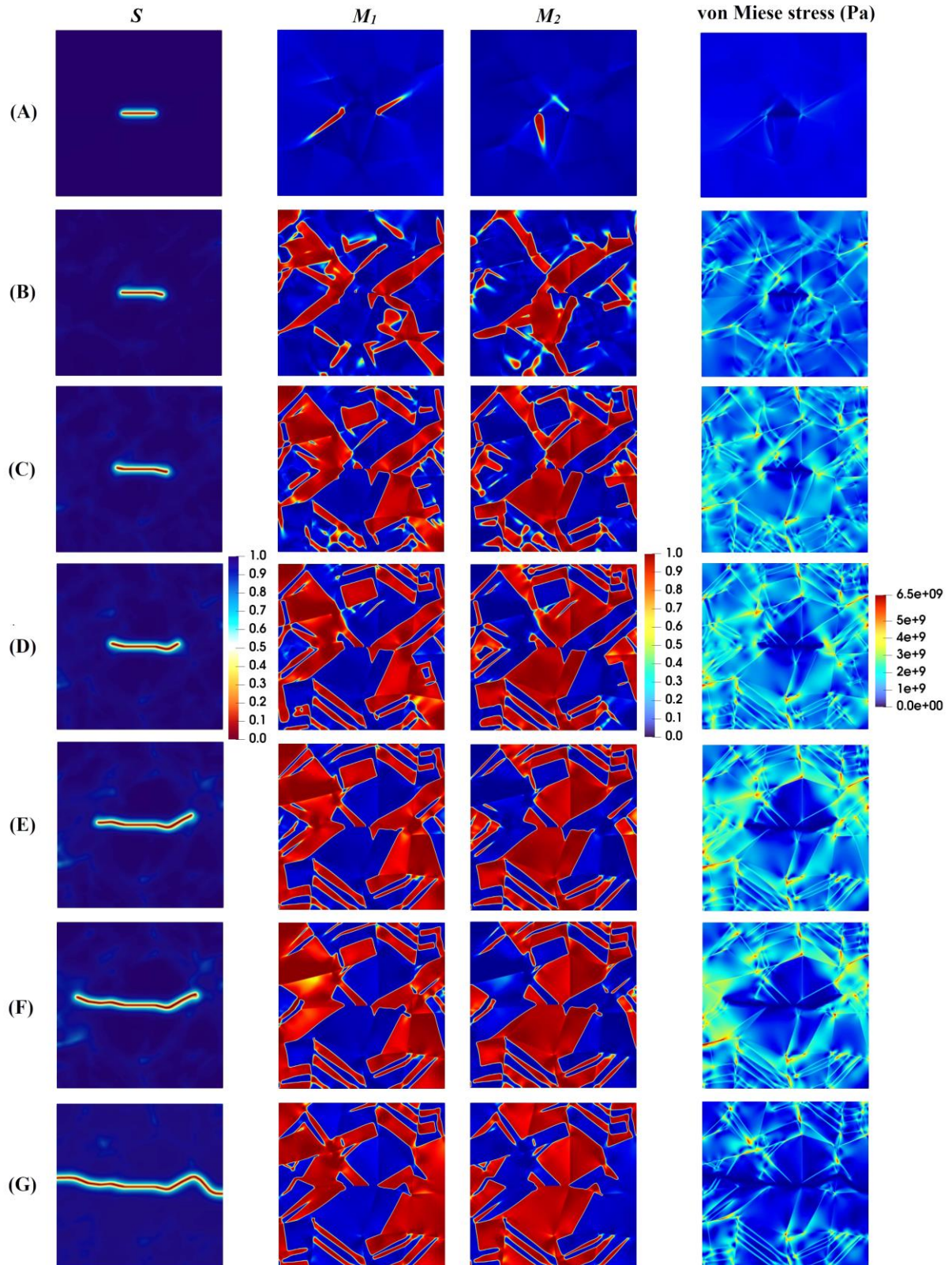


Figure 4.29: Evolution of damage variable, two martensite variants, and von Mises stress in the austenitic microstructure in the second polycrystalline structure according to Model 4.10



The volume fraction changes of the austenite and martensite phases at any given time are depicted for Model 4.9 and Model 4.10 in Figs. 4.30 and 4.31 respectively.

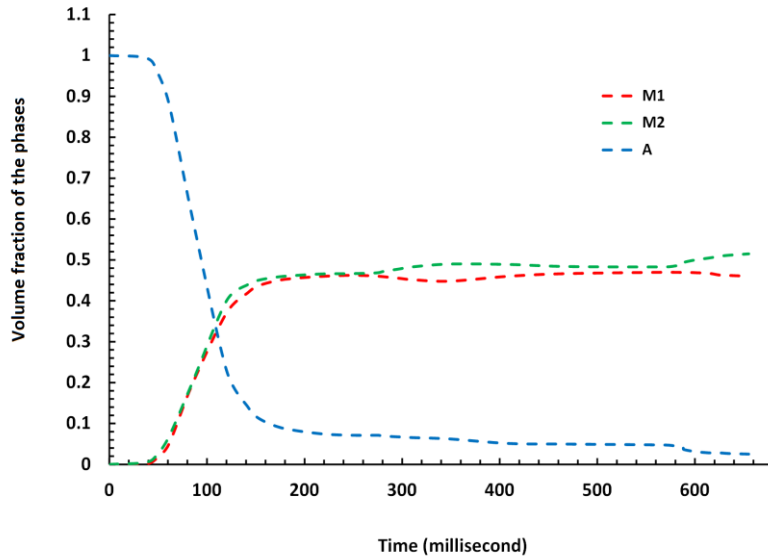


Figure 4.30: Variation of volume fraction of austenite and martensite phases for Model 4.9.

As we know, the problem begins in a completely austenitic domain, where the proportion of austenite steadily reduces as the crack expands, producing martensitic variants. Figs. 4.30 and 4.31 clearly present that after crack growth not much austenite remains in the material as we will observe an almost entirely martensitic structure to the end.

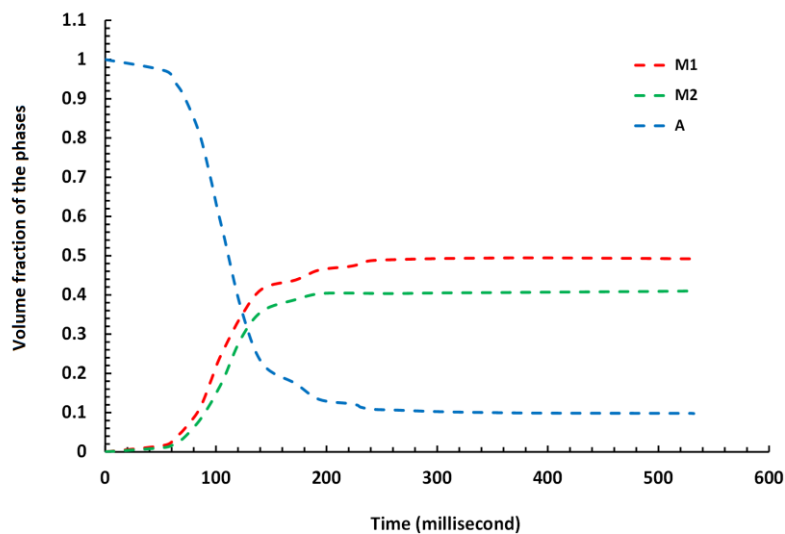


Figure 4.31: Variation of volume fraction of austenite and martensite phases for Model 4.10

In brief in this section of the work, a coupled problem of crack nucleation and propagation combined with two-variant MPT has been investigated based on PFA formulations. The model established includes a coupled system of three TDGL equations, which describe the evolution of the damage variable and two martensitic variants, the quasi-static equilibrium equation. This work has accounted for the positive dilatational component of the transformation strain, which accompanies the MPT from austenite to the martensite phase, leading to an eigenstrain within the martensitic phase. Since the eigenstrain results in both tensile and compressive parts, the model considers the sign of the dilatational component. In particular, this study concentrated on the interactions between microcrack initiation and propagation and cubic to tetragonal phase transformation. The main results can be summarized as follows:

- The results reveal that the crack growth does not begin until MPT has grown almost completely through the microstructure. This can be mainly attributed to the fact that MPT dissipates energy, which is accordingly not available for crack propagation.
- Subsequent to the initial formation of the martensite variants, the initial crack propagates in such a way that its path mainly depends on the feature of martensite variants formations, the orientation and direction upon which the martensite plates are aligned together, and the stress concentration between martensite plates.
- The results showed that in the case of the lattice orientation angle of  $30^\circ$  and  $45^\circ$ , as the crack propagates between layers of two martensite variants, due to high-stress concentration at the intersection of martensite variants on the crack surface, a crack-branching takes place.
- In the case of the lattice orientation angle of  $90^\circ$ , it can be concluded that the crack tends to propagate between martensite variants, and at the same time due to high-stress concentration formed at a location far from the main crack, a new crack initiates and grows. After that, the two cracks approach each other irrespective of the boundary between martensite variants and eventually intersect each other.
- Geometric flaws in materials are also a significant cause of fracture. These geometric imperfections, such as porosity or a tiny hollow, are also referred to as contributing elements to the failure phenomena. High-stress concentrations in the vicinity of geometric flaws trigger crack growth, providing the energy required for martensitic transformation. In these kinds of coupled problems typically the martensitic transformation takes place in priority. The crack finds its path in proportion to the first phase generated, and while affecting the martensite phase again, it develops a new structure that will affect the crack path again.

- Polycrystalline structures have a significantly more complex structure than single crystal materials, making studying fracture behavior and phase change of the material more difficult. In this type of structure, in addition to the different orientations of the martensite layers, the interlayer stresses of the martensite and austenite and the concentration of stress between them affect the behavior of the material, and the discontinuity of grain boundaries has a great effect on crack behavior and phase transformation. The crack behavior and martensitic variants arrangement alter as a result of these discontinuities, which are caused by both the geometric effect and the angular behavior of the material characteristics.

### **4.3 A phase field approach for fracture coupled with martensitic transformation and heat transfer**

In this section, the results of a fully thermomechanical coupled phase-field (PF) model are presented to see the mechanism of austenite-to-martensite phase transformation (MPT) and crack initiation and propagation in pure austenitic microstructures. The results are according to the equations discussed in section 4.4. This section is divided into two main categories. Initially, for simplification in modeling as well as better analysis of the results and the relation between temperature, fracture, and martensitic transformation, it was decided to consider only the effect of one of the martensitic variants modeling. After analyzing and interpreting the results, in the second part, the problem is solved completely by adding the effect of the second martensitic variant. The key contributions of this work are to shed light on the impact of thermal boundary conditions on the coupled process of MPT and crack initiation and growth. The numerical results presented demonstrate that the model can be applied to study the fracture mechanism of austenitic microstructures under a thermomechanical field in a multiphysics environment. It has been noted that the higher thermal boundary condition has a tremendous impact on the growth rate of both martensitic variants and, as a result, on the crack growth path.

#### **4.3.1 The one variant of martensitic transformation coupled with fracture and heat transfer**

Fig. 4.32 shows the geometry, initial conditions, mechanical and temperature boundary conditions, and loading. The tensile loading in the first fracture mode of this sample has been investigated. In order to study the effect of temperature on this coupling problem, this analysis is conducted for three different models which differ in terms of temperature boundary conditions. The evolution of coupled one-variant MPT and crack growth for Model 4.11, in which the entire specimen is at a constant temperature of 280 K, is shown in Fig. 4.33.

As previously stated, temperature changes can affect the results in a variety of ways, the most important of which is the generating of thermal strain and changes in the energy level necessary for MPT.

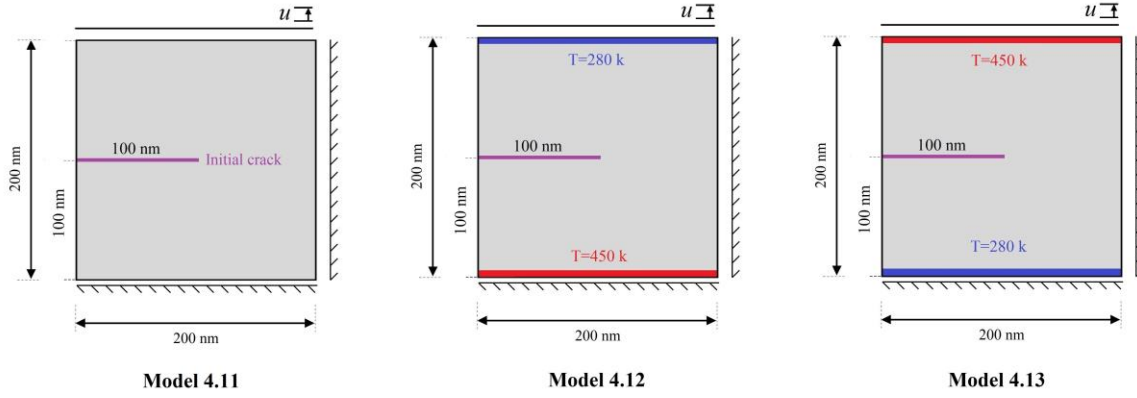


**Figure 4.32: Geometry, boundary conditions, and initial crack position for the three models**

For this simulation, material properties including mechanical and thermal properties and parameters related to martensitic transformation are defined according to the following conditions. The parameter  $A(T)$  in Fig. 4.6, which plays a major role in the formation of separation energy, should be defined as temperature dependent, which is used in accordance with the concepts discussed in Section 4.4 in modeling. The models have been discretized using 161,604 linear 4-node elements [19]

$$\begin{aligned}
 K_A &= 1.73 \times 10^5 \text{ MPa}, & \mu_A &= 0.8 \times 10^5 \text{ MPa} \\
 K_M &= 1.1 K_A, & \mu_M &= 1.1 \mu_A \\
 \rho &= 5850 \text{ kg/m}^3, & \kappa &= 55 \text{ W/mk}, & c_p &= 480 \text{ J/kg}^\circ\text{k}, & \alpha &= 1.4 \times 10^{-5} / ^\circ\text{k} \\
 L_c &= 1 \text{ nm}, & G_c &= 1 \frac{\text{J}}{\text{m}^2}, & M_c &= 1.0 \times 10^{12} \frac{\text{m}^3}{\text{Js}} \\
 L_s &= 1 \text{ nm}, & G_s &= 1 \frac{\text{J}}{\text{m}^2}, & M_s &= 1.0 \times 10^{12} \frac{\text{m}^3}{\text{Js}}
 \end{aligned} \tag{4.5}$$

The results of these three simulations are presented below. The process of martensitic formation and crack growth, which are coupled together, is presented in these results. The martensitic phase transformation starts from the crack tip and chooses its path for growth in accordance with the boundary between the martensitic and austenitic layers and the stresses created under this process.

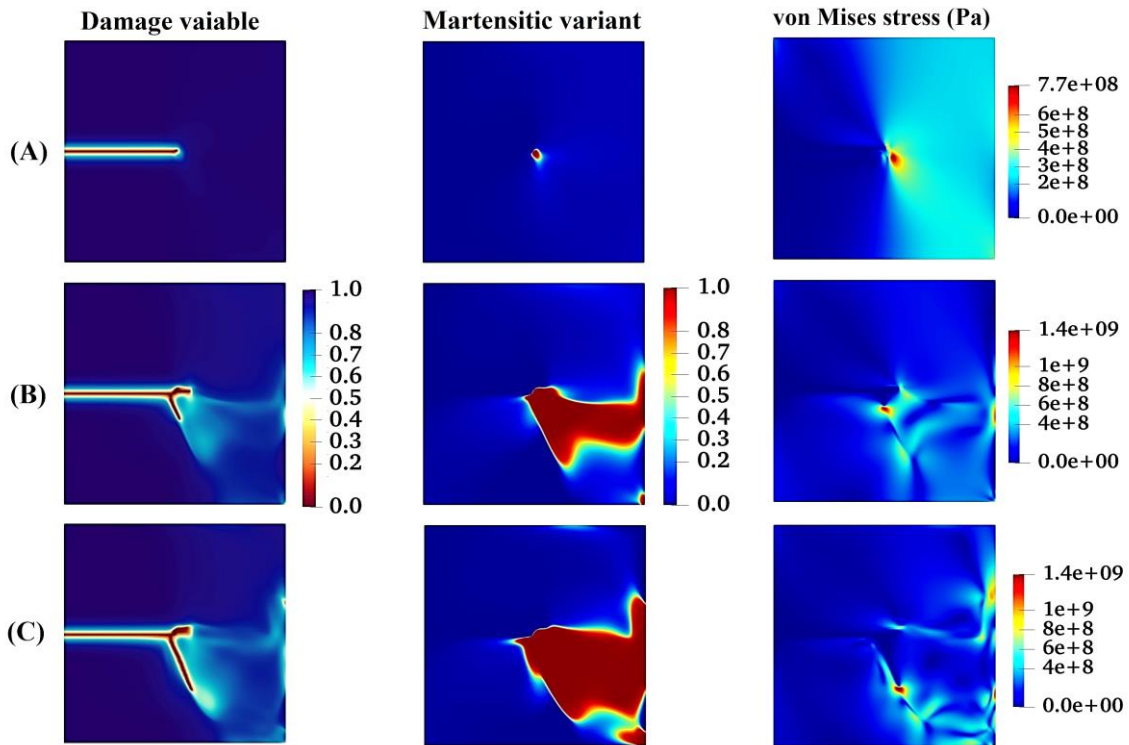


**Figure 4.33: Evolution of the crack field, martensitic variant and von Mises stress without thermal boundary condition (Model 4.11)**

The results of the second and third model simulations are shown in Figs. 4.34 and 4.35, respectively. To better compare the results and investigate the effect of temperature on the results, the fracture field, the martensitic variable, and the temperature distribution in the material are presented. When the findings are compared, it is obvious that different temperature distributions result in different algorithms for the generation of martensitic structure and, as a result, fracture growth in the material.

According to Figs. 4.34 and 4.35, as the temperature of the points rises, the energy level required for martensitic transformation increases, which means that this phase change becomes more difficult. This increase in temperature causes the energy released in the stress-induced process at the crack tip, to be insufficient for the transformation. Lack of energy supply causes these areas to remain in the austenite phase and in areas with lower temperatures, the chance of martensite formation is higher.

It can be said that increasing the temperature in addition to creating thermal strain leads to changing the boundaries between martensite and austenite, which in turn has a significant effect on the crack path.

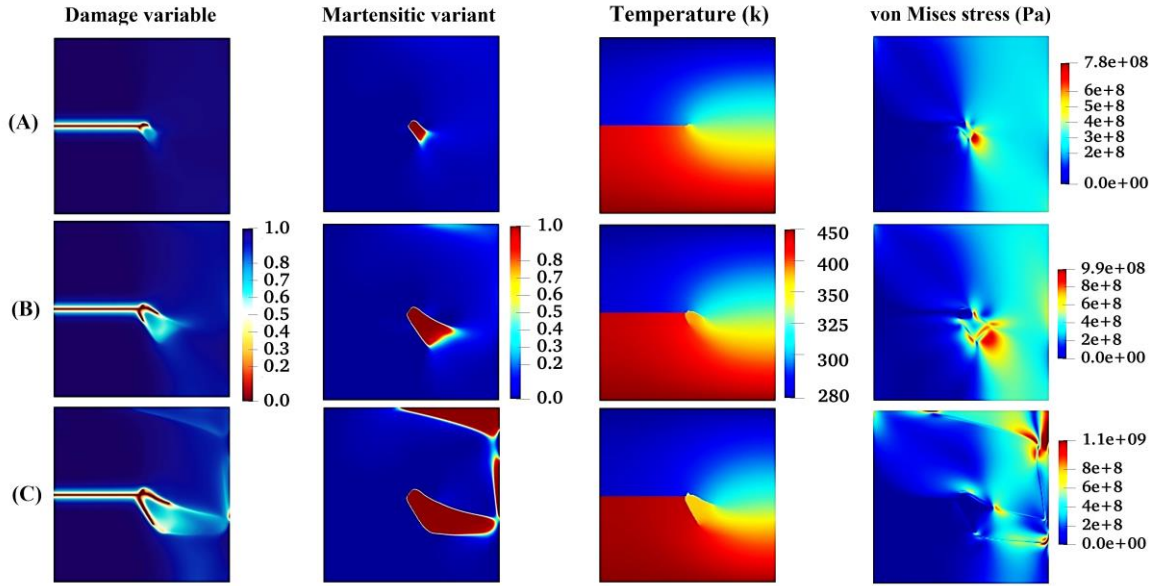


Figure 4.34: Evolution of the crack field, martensitic variant, temperature field and von Mises stress (Model 4.12)

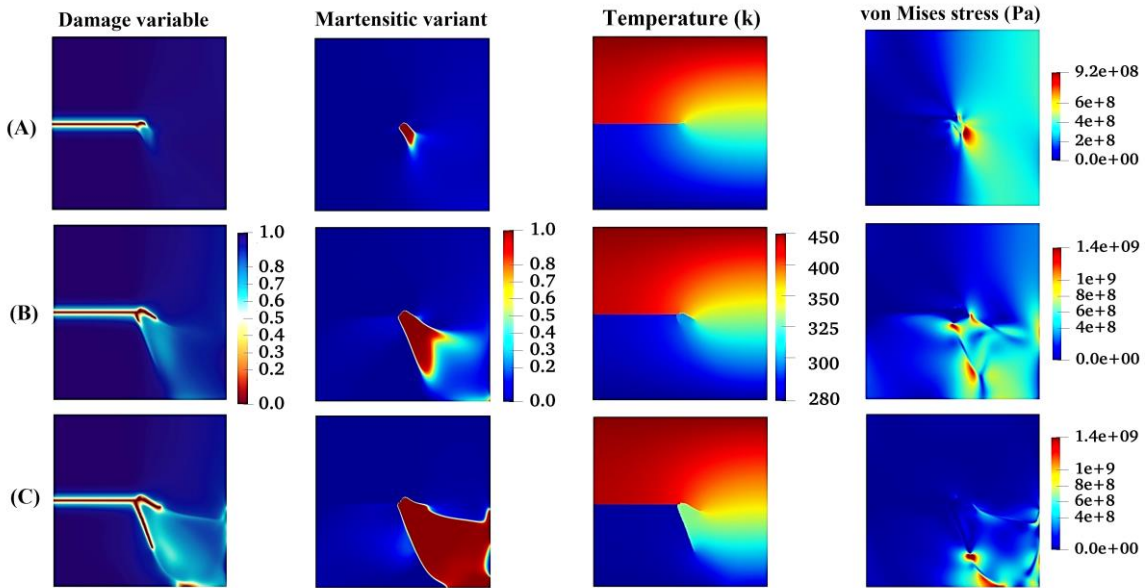
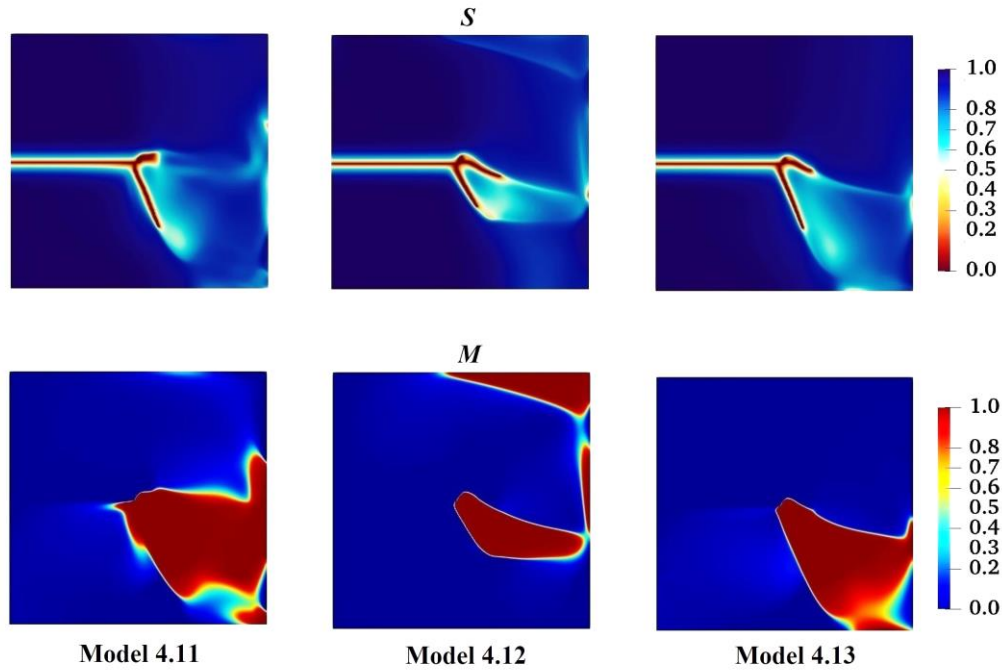


Figure 4.35: Evolution of the crack field, martensitic variant, temperature field and von Mises stress (Model 4.13)

Fig. 4.36 compares the results of three models in which the selection of different temperature boundary conditions in the models results in different fracture behaviors in the material. What all models have in common is that the crack tends to move along the boundary of the areas between martensite and austenite.



**Figure 4.36: Comparison of fracture variable and martensitic formation obtained from the three models**

In accordance with the results of Models 4.12 and 4.13, increasing the temperature has reduced the chance of martensitic formation, and in fact, high temperatures have caused the austenite phase to dominate the volume fraction in this transformation. It should also be noted that the highest volume percentage of the martensitic phase belongs to the first model, which is in lower temperature conditions than the other two models.

### 4.3.2 The two-variant martensitic transformation coupled with fracture and heat transfer

In order to take the simulation results closer to reality, the effect of the second martensitic variant has been added to the analysis. This means the model has six degrees of freedom whose output will be displacement  $u_1$ ,  $u_2$ , martensitic variants  $c_1$ ,  $c_2$  fracture variable  $s$ , and temperature  $T$  at any given time. The material properties include mechanical and thermal properties, and concepts related to martensitic phase transformation and fracture are similar to the previous section. In order to have a better understanding of the effect of temperature changes on this coupled problem, two identical models with different temperature boundary conditions have been defined, which are shown in Fig. 4.37. As can be seen in the figure, the second model is subject to higher temperature conditions, in the effect of this temperature increase on the martensitic transformation and fracture behavior has been investigated.



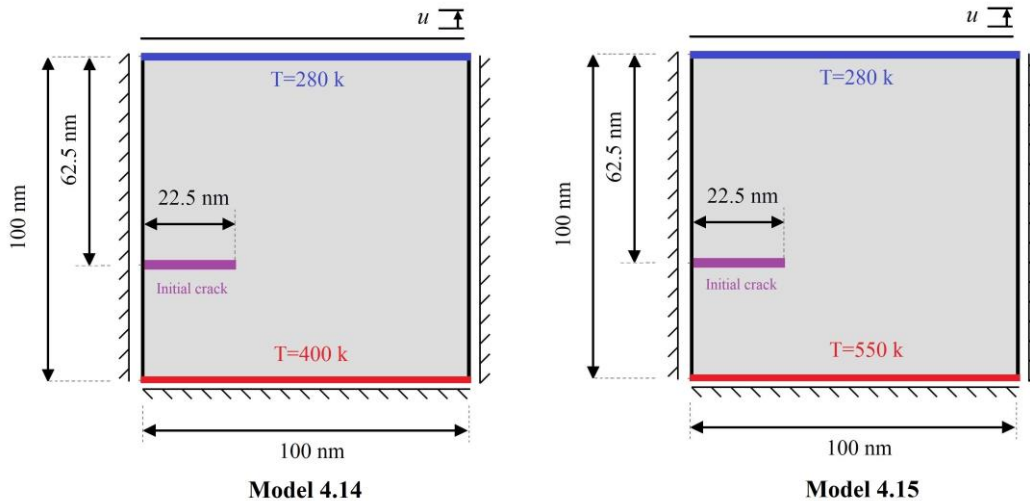


**Figure 4.37: Geometry, boundary conditions, and initial crack position for the two models**

The results of Model 4.14 are shown in Fig. 4.38. The fracture field, the formation of martensitic variants, the temperature distribution, and the von Mises stress are all displayed in columns 1 to 5, respectively. The martensitic transformation occurs at the crack tip, as seen in Fig. 4.38. A before the material begins to crack propagation. The process of forming martensitic variables at the lower section of the material is more difficult because the lower edge of the material is at a higher temperature than the top edge (second and third columns). As can be observed in the figure, martensitic variables develop at a slower rate and have a lower martensitic volume fraction in the lower part of the material, however, this tendency is reversed in the upper section, which is at a lower temperature.

The crack begins to expand once the first martensitic structure is formed in the material, and its behavior is determined by the initial structure. The fracture evolution can alter the microstructure and result in the formation of new structures. It can be argued that temperature changes in the material that lead to the generation of a different martensitic structure in the material (compared to a constant temperature state) will influence fracture behavior.

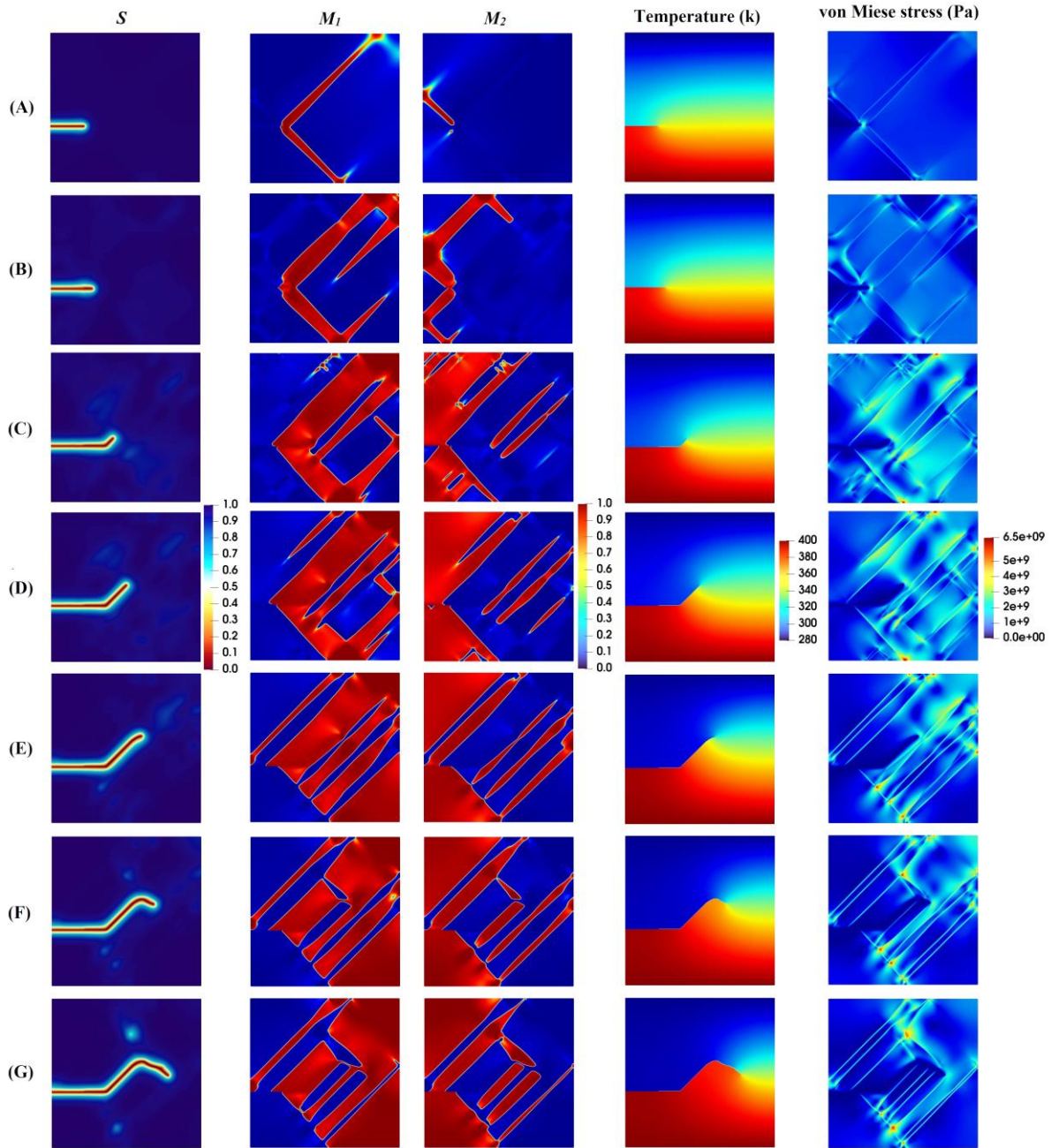


**Figure 4.38: Evolution of damage variable, two martensite variants, temperature, and von Mises stress in the austenitic microstructure in Model 4.14**

Under a coupling process, cracks continue to propagate throughout the material, and the material final results in the formation of martensitic structure, temperature distribution, and interlayer stress distribution are ultimately observed in Fig. 4.38.G. Findings show that stress concentration, martensitic orientations, and the presence of interlayer stress are the most critical factors influencing fracture behavior, as previously stated.

Fig. 4.39 graphically focuses on the process of formation of martensitic variants before and after crack growth. As shown in the figure, before the time of 100 milliseconds, the energy needed to start the martensitic transformation is not provided. After the time and energy required for this phase change at the crack, the tip has been supplied, the martensitic variants propagate throughout the material, progressively decreasing the volume percentage of austenite.

By reviewing the findings visually, it can be observed that the first martensitic variant is the dominating phase in this process, which continues until the end. As is monitored, less than 7% of the austenite phase material is included at the end of the simulation, compared to 50% and 43% for the first and second martensitic variants, respectively.

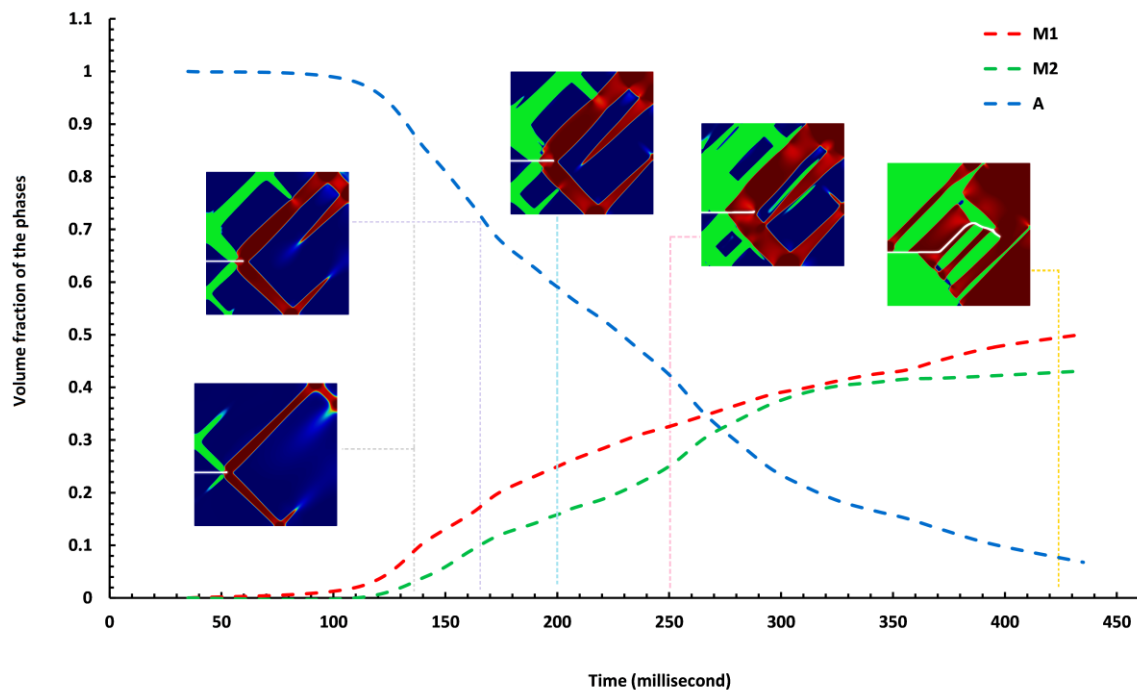


**Figure 4.39: Phase transformation of austenite to martensite graphically and based on the volume percentage of martensitic variants in Model 4.14**

The findings of the Model 4.15 simulation are shown in Fig. 4.40. The fracture field, the distribution of the martensitic variants, the temperature distribution, and the von Mises stress in the structure are all presented, the same as in Model 4.14. Model 4.15 differs from Model 4.14 in which the lower side of the material is at a higher temperature, which is intended to increase the temperature.

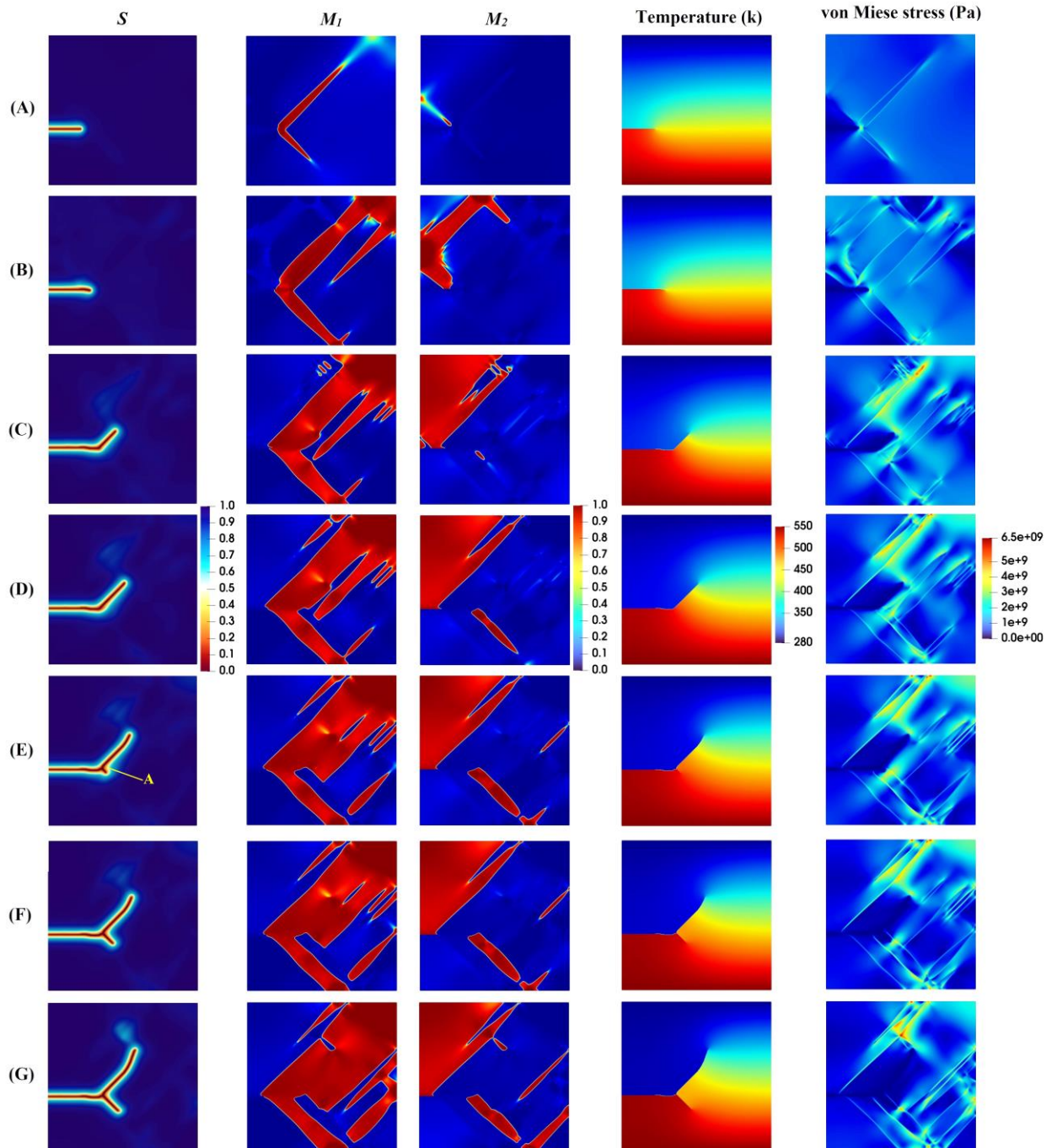


**Figure 4.40: Evolution of damage variable, two martensite variants, temperature, and von Mises stress in the austenitic microstructure in Model 4.15**

The formation of martensitic variables is more difficult in the bottom part of the material than in the previous model, and as can be seen, the lower section of the material has a lesser proportion of the created martensite. With the beginning of crack growth in the material and its progression at the end, we will have a structure consisting of an austenite phase and two martensitic variants, in which the volume percentage of austenite is higher than in the previous



model. Studying the crack behavior in this model is noteworthy that a new crack in the material develops from point A and begins to grow, creating a new branch. The presence of high-stress concentration at point A and interlayer stresses between the martensitic variants has led to the creation and expansion of this new branch.

Fig. 4.41 shows a graph of the martensite phase formation process in Model 4.15. As can be seen from the figure, no significant phase change occurs in the material before the time of 120 milliseconds until the stress concentration generated at the crack tip leads to the onset of this phase change. The initial martensitic variant is the dominating phase in this model, as it was in the previous simulation, and this tendency continues until the end, with the difference increasing during the process.

The noteworthy point in this model is that at the end of the simulation a significant percentage of the austenite phase (about 27%) remains in the material, which is about 45% and 28% for the first and second martensitic variants, respectively.

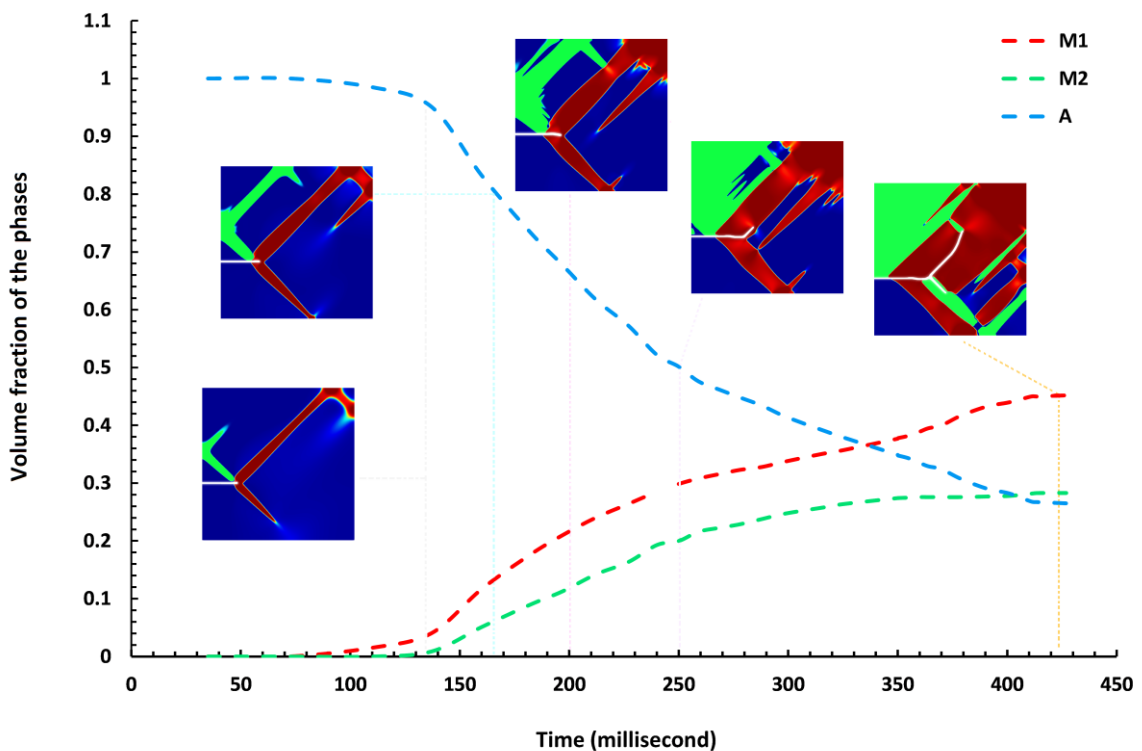


**Figure 4.41: Phase transformation of austenite to martensite graphically and based on the volume percentage of martensitic variants in Model 4.15**

Fig. 4.42 illustrates the schematic comparison between the two proposed models which includes the process of martensitic formation and crack growth in both models step by step. The commencement of the martensitic transformation in the first model begins and proceeds faster and with a greater volume percentage, as indicated in the figure. The second model is

kept in higher temperature conditions in which it is more difficult to supply the energy required for the martensitic phase change, which can be seen until the end. The first model is completely occupied by martensitic variants at the completion of the simulation (row J), whereas in the second model, parts of the material (about 27%) remain austenitic.

If these two models are examined from the point of view of the fracture field, it can be stated that the crack in the second model starts moving earlier. The reason for this is that due to the increase in temperature, the level of energy required to change the martensitic phase increases.

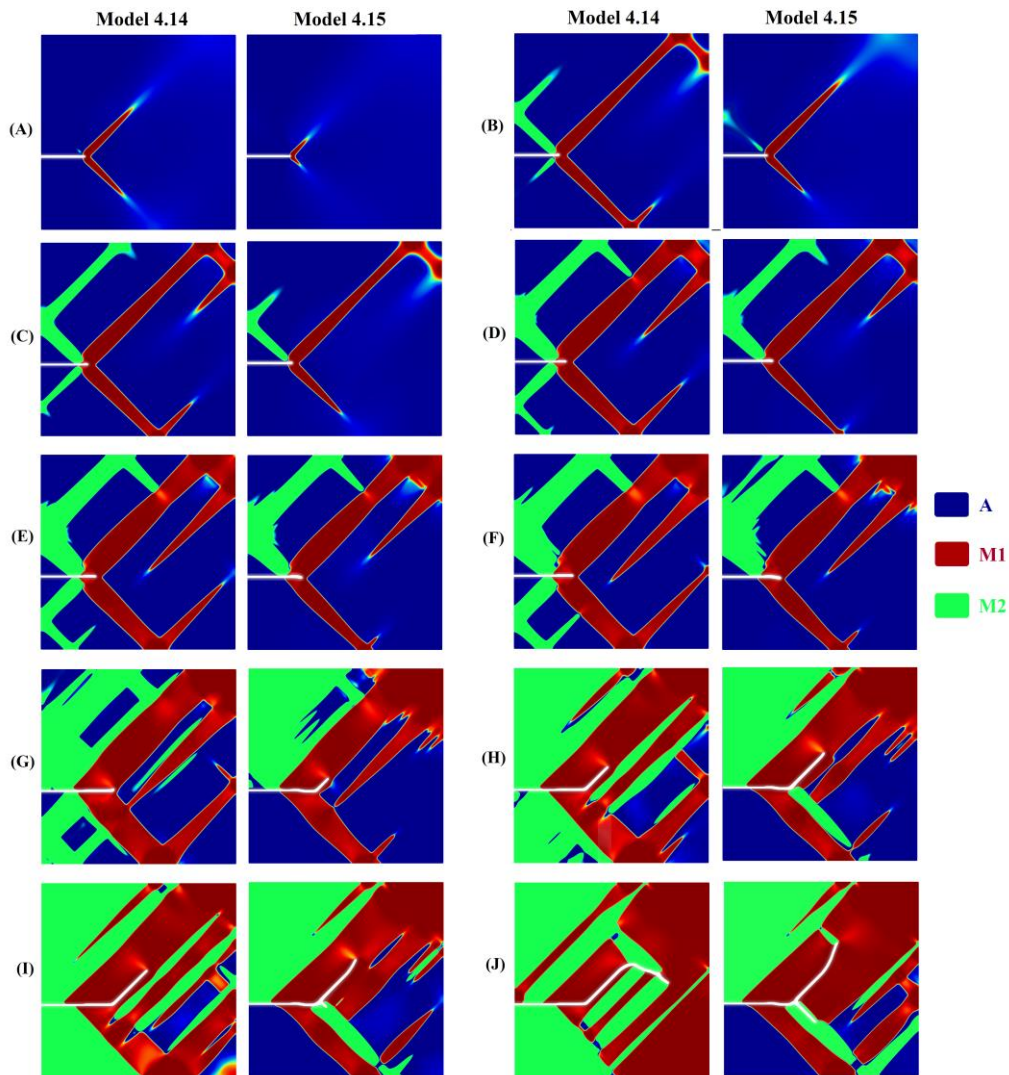


Figure 4.42: Comparison of crack progression and formation of martensitic variants in the two models

As the required martensitic transformation energy in the material increases, the available energy goes for the crack growth, which is not enough to change the martensitic phase. This means that the material uses the available energy for crack growth. After the crack starts to grow and

moves throughout the material, depending on the problem conditions, the martensitic transformation can consume some of the energy in the material and this phase change occurs simultaneously with the crack growth. It can be noted that different temperature boundary conditions create a different pattern for the martensitic structure and thermal strain in the two models, which eventually leads to different fracture behavior in the two models.

In the following, Fig. 4.43 compares the formation process of martensitic variants in the two models based on the volume percentage of each variant. This comparison based on the volume percentage of remaining austenite has also been shown in Fig. 4.44.

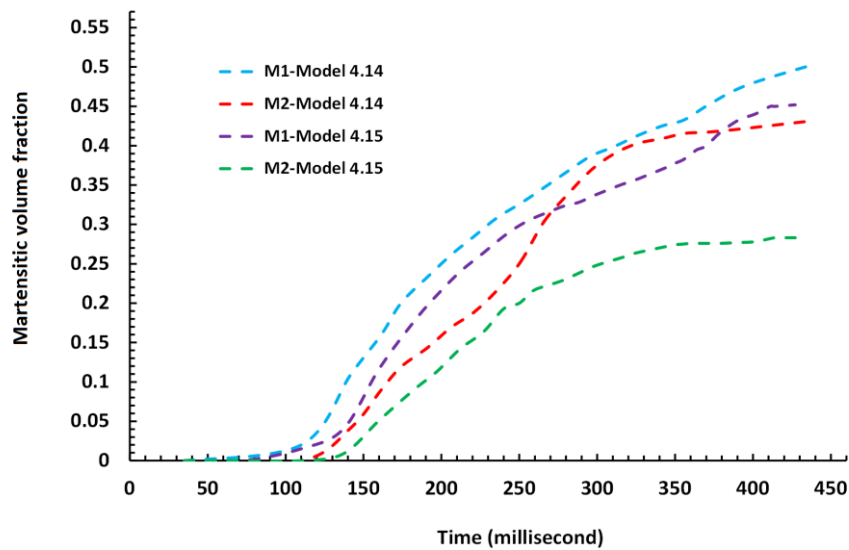


Figure 4.43: Variation of the volume fraction of the martensitic phases,  $M_1$  and  $M_2$  for the two models

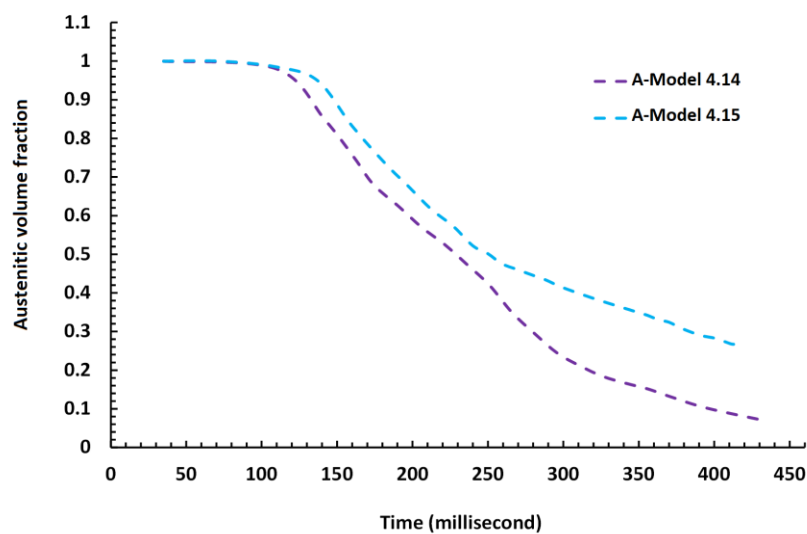


Figure 4.44: Variation of the volume fraction of the austenitic phase,  $A$  for the two models





## Conclusion and Recommendation for Future Research

### 5.1 Main conclusions

In this chapter, the results obtained in this research are briefly reviewed. The overall purpose of this work was to investigate a coupled problem in the field of fracture mechanics and martensitic phase change, a PFA-based computational framework. Initially in **sections 4.1**, in order to simplify and better understand the concepts of each part, it was decided to examine this problem in an uncoupled method. The advantage of this was that the details of the material phase change and the failure mechanics were done with a greater focus on the details of each part. First, a phase change problem of austenite to martensite has been considered. Then, the fracture behavior in this martensitic structure was analyzed by tensile loading on the obtained results.

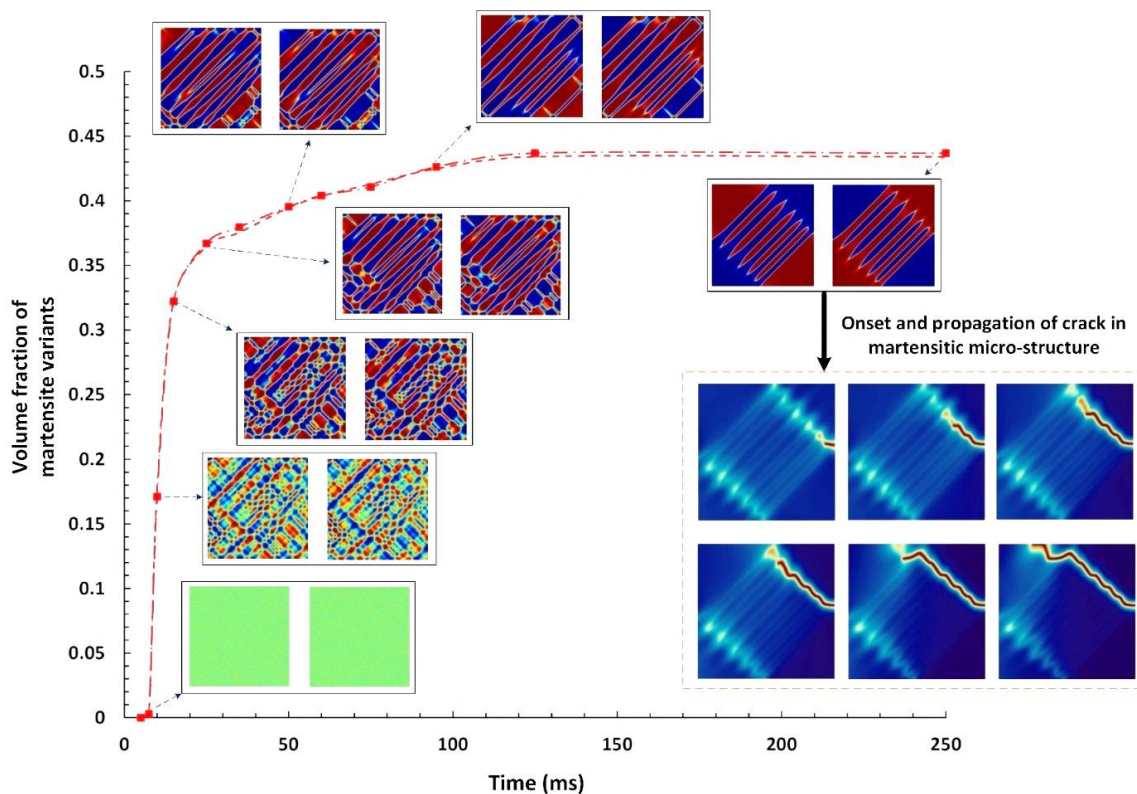


**Figure 5.1:** Graphical abstract of the first part of the study (Uncoupled crack propagation in a martensitic microstructure) [129]

This section of the study is summarized graphically in Fig. 5.1. This figure depicts the MPT process, as well as the crack initiation and propagation in martensite obtained in a randomly distributed initial martensite state.

In **section 4.2**, in order to get closer to more realistic concepts, the problem of fracture mechanics coupled with the MPT has been studied. For this purpose, by re-examining the problem and the effective energy terms, the coupling parts of the problem were redefined. This study was first analyzed in a single crystal material for different martensitic orientations of 15, 30, 45, 60, and 90. The next example explains one of the significant advantages which the phase-field method offers in comparison to other methodologies. This method, in contrast to the majority of other techniques, has the ability to identify the places in the material with the potential to initiate cracks. It can be inferred from the results of this section, in this coupled problem the stress concentration at the crack tip provides the energy needed to phase transformation under a stress-induced process. Before crack growth begins, an initial martensitic structure forms in the material, affecting crack behavior. The presence of stresses between the phase layers, the stress concentration, and the martensitic orientation progression are important factors affecting crack behavior. Due to these factors, cracks grow in the material. It again affects the structure of the initial martensite; interestingly, this new structure affects the movement of the crack again. After the final growth of the crack in the material, the final martensitic structure will be created, completely different from its primary structure. During material failure, observations such as nucleation and the formation of new crack branches are also significant points of this study, which are created in the material under certain conditions. Examining the different martensitic orientation structures in **section 4.2.1**, the idea of working on a polycrystalline problem was created, which solved two polycrystalline problems with different crystalline arrangements. A suggestion of considering the effect of the grain boundaries can be counted as a novel research field in future work.

Figure 5.2 schematically summarizes the final results of the different simulations performed in **section 4.2**. These results include fracture field, martensitic variants, and von Mises stress distribution in the structure.

Section 4.3 of this research adds the effect of temperature as an independent parameter to the set of equations governing this problem by defining the transient heat transfer equation as a degree of freedom. Thus, the coupled fracture problem with the MPT was defined by defining the temperature and mechanical boundary conditions, and the necessary energy for this phase change was provided in a temperature and stress-induced process. Two identical models with different temperature boundary conditions have been defined to better understand and explain the effect of temperature. The results of these two simulations are compared graphically and schematically in Fig. 5.3.

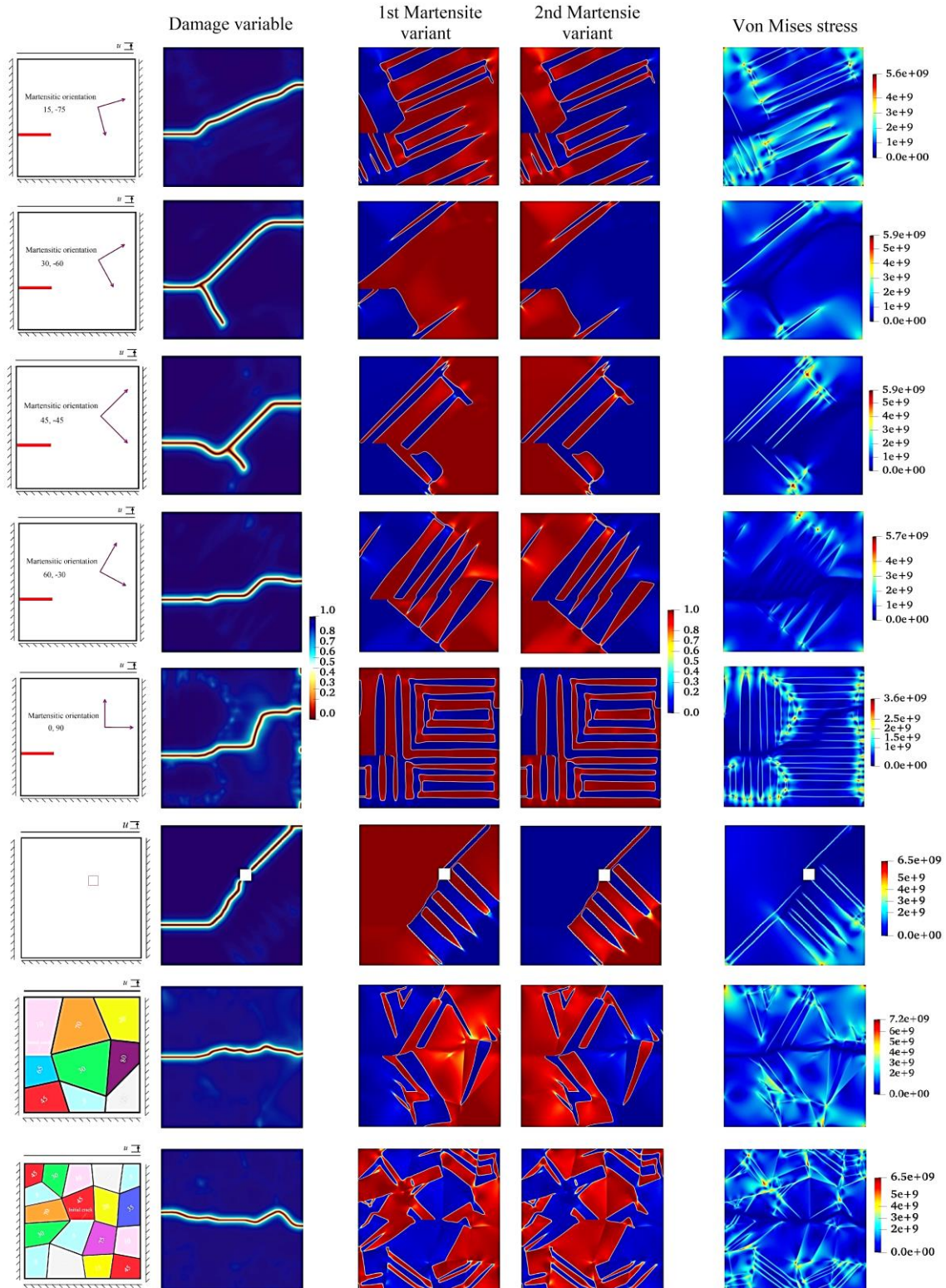


**Figure 5.2: The final results obtained in a coupling fracture mechanics and martensitic phase change according to the geometric and boundary conditions shown for each problem related to section 4.2**

It can be mentioned that temperature plays an essential role in this problem by generating thermal strain and changing the energy level required for the transformation. However, the

effect of thermal strain is less than the strain of phase change. High temperature increases the energy barrier between the stable martensite phase and the metastable austenite, which means more energy is required to overcome this barrier and consequently the MPT. As it is clear from the results, points with higher temperatures have a lower phase change rate and lesser martensitic volume percentage. It is also noteworthy that the temperature rise may be so high that the energy released at the crack tip is insufficient to change the martensitic phase. Some points remain austenitic, as seen in Model 4.15.

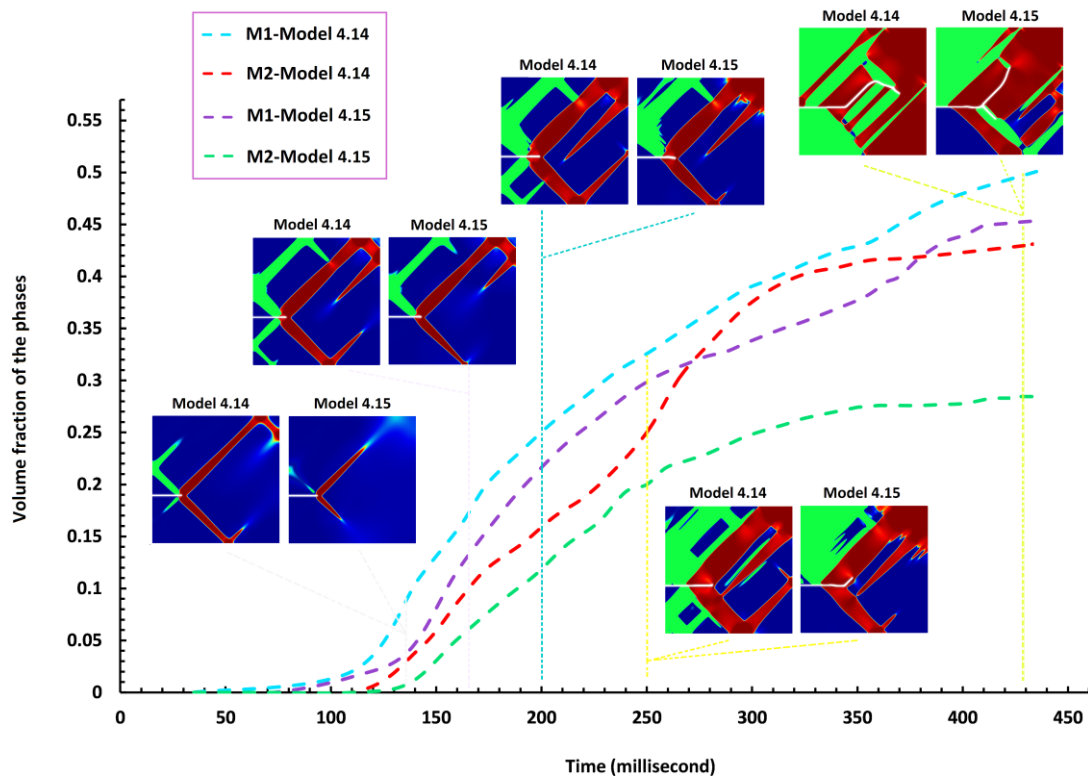


**Figure 5.3: Comparison and variation of the volume fraction of the martensitic phases,  $M_1$  and  $M_2$  for Model 4.14 and Model 4.15 related to section 4.3**

## 5.2 Recommendations for future research

The following, suggestions for further research activities are proposed:

- A three-dimensional simulation of the subject can be studied. We can expect the numerical findings to be closer to reality if the third spatial dimension and the effect of the third martensitic variant are included. [130-136]
- Since the structure of many materials is polycrystalline, it is imperative to study the behavior of this type of structure in the coupled analysis [137-140]. This work attempted to study this behavior by combining single crystals with the ability to spread

martensite at different orientations with perfectly continuous grain boundaries [141]. However, examining the behavior of grain boundaries in detail can be a very interesting issue. The grain boundaries are not completely continuous, and the amount of this discontinuity depends on factors such as the difference in material properties and the angular difference of adjacent crystals, and the difference in the toughness of these neighboring crystals [142]. In order to better implement grain boundary behaviors, other methods such as the cohesive zone method or XFEM can be used in addition to PFA. These methods can play a role independently or by coupling with PFA formulation [144, 144].

- One of the critical applications of this research topic can be discussed in fatigue or shape memory alloy problems [145-149]. To examine the issues more realistic, the effects of plasticity must be considered adequately in the research topics. [130, 150].
- Since numerical works always face the challenge of validation, conducting experimental efforts in this field is crucial. So far, the research topic has received limited experimental studies and the absence of such attempts is noticeable.





# Bibliography

- [1] Efendi Maburri, Siska Prifiharni, Moch. Syaiful Anwar, Toni B. Romijarso, Bintang Adjiantoro, Mechanical properties optimization of the modified 410 martensitic stainless steel by heat treatment process, *Materials Today: Proceedings*, Volume 5, Issue 7, Part 1, 2018, Pages 14918-14922.
- [2] Valery I. Levitas, *Phase Transformations in Elastic Materials*, Draft date August 27, 2018
- [3] H.K.D.H. Bhadeshia, R. Honeycombe, *Steels: microstructure and properties. The tempering of martensite steels* (Oxford, OX: United Kingdom Elsevier Publishing Company, 2006), 183-208.
- [4] C.S Smith, A history of martensite: Early ideas on the structure of steel, in: G.B. Olson, W.S. Owen (Eds.), *Martensite*, ASM Int., Materials Park, OH, 1992, pp. 21-39.
- [5] G.E. Totten, *Steel heat treatment: Metallurgy and technologies* (London, LON: LLC Taylor & Francis Group, 2006), p207.
- [6] L. Delaey, Diffusionless transformations. In: Cahn R W, Haasen P, Kramer E J (eds.) *Materials Science and Technology*, Vol. 5, *Phase Transformations in Materials*. VCH, Weinheim, Germany, 1991.
- [7] B.C. Muddle, J.F. Nie, *Martensite*, *Encyclopedia of materials: science and technology*, Elsevier
- [8] E. J. Mittemeijer, *Fundamentals of materials science, the microstructure-property relationship using metals as model systems*. Springer-Verlag Berlin Heidelberg, 2010
- [9] Z. Y. Hou, P. Babu, P. Hedström, J. Odqvist, Microstructure evolution during tempering of martensitic Fe-C-Cr alloys at 700 °C, *J Mater Sci*, 2018, 53(9): 6939–6950
- [10] Mitchell, S. & Youseffi, Mansour & Abosbaia, Hadi & Ernest, J. (2008). *Progressing and Heat Treatment of High Carbon Liquid Phase Sintered Steels*.
- [11] Reisner G, Werner EA, Fischer FD, *Micromechanical modeling of martensitic transformation in random microstructures*. *International journal of solids and structures* 1998;35(19):2457–73
- [12] Bartel T , Hackl K, *A novel approach to the modelling of single-crystalline materials undergoing martensitic phase-transformations*. *Materials Science and Engineering: A* 2008;481:371–5 .

- [13] Bartel T , Menzel A , Svendsen B, Thermodynamic and relaxation-based modeling of the interaction between martensitic phase transformations and plasticity. *Journal of the mechanics and physics of solids* 2011;59(5):1004–19
- [14] Cherkaoui M, Berveiller M, Sabar H, Micromechanical modeling of martensitic transformation induced plasticity (TRIP) in austenitic single crystals. *International Journal of Plasticity* 1998;14(7):597–626 .
- [15] Chan S-K, Steady-state kinetics of diffusionless first order phase transformations. *The Journal of chemical physics* 1977;67(12):5755–62 .
- [16] Khachaturyan AG, *Theory of structural transformations in solids*. Courier Corporation; 2013
- [17] Wang Y , Khachaturyan AG, Three-dimensional field model and computer modeling of martensitic transformations. *Acta materialia* 1997;45(2):759–73 .
- [18] Levitas VI , Preston DL, Three-dimensional landau theory for multivariant stress-induced martensitic phase transformations. i. austenite martensite. *Physical review B* 2002;66(13):134206
- [19] Yamanaka A , Takaki T , Tomita Y, Elastoplastic phase-field simulation of martensitic transformation with plastic deformation in polycrystal. *International Journal of Mechanical Sciences* 2010;52(2):245–50 .
- [20] Levitas VI, Phase-field theory for martensitic phase transformations at large strains. *International Journal of Plasticity* 2013;49:85–118 .
- [21] Schmitt R , Müller R , Kuhn C , Urbassek HM. A phase field approach for multivariant martensitic transformations of stable and metastable phases. *Archive of Applied Mechanics* 2013;83(6):849–59 .
- [22] Mamivand M , Zaeem MA , El Kadiri H, Phase field modeling of stress-induced tetragonal to monoclinic transformation in zirconia and its effect on transformation toughening. *Acta materialia* 2014;64:208–19 .
- [23] Rabczuk T, Computational methods for fracture in brittle and quasi-brittle solids: state-of-the-art review and future perspectives. *ISRN Applied Mathematics* 2013;2013
- [24] Francfort GA, Marigo J-J. Revisiting brittle fracture as an energy minimization problem. *Journal of the mechanics and physics of solids* 1998;46(8):1319–42 .
- [25] Bourdin B, Francfort GA, Marigo J-J, Numerical experiments in revisited brittle fracture. *Journal of the mechanics and physics of solids* 2000;48(4):797–826 .
- [26] Ortiz M, Pandolfi A, Finite-deformation irreversible cohesive elements for three-dimensional crack-propagation analysis. *International journal for numerical methods in engineering* 1999;44(9):1267–82.

- [27] Krueger R, Virtual crack closure technique: history, approach, and applications. *Applied mechanics reviews* 2004;57(2):109–43 .
- [28] Moës N , Dolbow J , Belytschko T, A finite element method for crack growth without remeshing. *International journal for numerical methods in engineering* 1999;46(1):131–50 .
- [29] E. Moshkelgosha, M. Mamivand, Phase field modeling of crack propagation in shape memory ceramics application to zirconia, *Computational Materials Science* 174 (2020) 109509.
- [30] J. Clayton, J. Knap, Phase field modeling and simulation of coupled fracture and twinning in single crystals and polycrystals, *Computer Methods in Applied Mechanics and Engineering* 312 (2016) 447–467.
- [31] R. Schmitt, C. Kuhn, R. Skorupski, M. Smaga, D. Eifler, R. Müller, A combined phase field approach for martensitic transformations and damage, *Archive of Applied Mechanics* 85 (9) (2015) 1459–1468
- [32] H. Jafarzadeh, V. I. Levitas, G. H. Farrahi, M. Javanbakht, Phase field approach for nanoscale interactions between crack propagation and phase transformation, *Nanoscale* 11 (46) (2019) 22243–22247.
- [33] C. Cissé, M. A. Zaeem, Transformation-induced fracture toughening in CuAlBe shape memory alloys: A phase-field study, *International Journal of Mechanical Sciences* 192 (2021) 106144.
- [34] J. Altenbach and H. Altenbach, *Einführung in die Kontinuumsmechanik*. B. G. Teubner Stuttgart, 1994.
- [35] M. E. Gurtin, E. Fried, and L. Anand, *The Mechanics and Thermodynamics of Continua*. Cambridge University Press, 2010.
- [36] P. Haupt, *Continuum Mechanics and Theory of Materials*. Springer, 2002
- [37] G. A. Holzapfel. *Nonlinear Solid Mechanics, A Continuum Approach for Engineering*. John Wiley & Sons, 2000.
- [38] W. Becker and D. Gross, *Mechanik elastischer Körper und Strukturen*. SpringerVerlag, 2002
- [39] D. Gross and T. Seelig. *Bruchmechanik, Mit einer Einführung in die Mikromechanik*. Springer Berlin Heidelberg, 2007.
- [40] E. Pereloma and D. V. Edmonds, editors, *Phase Transformations in Steels*. Woodhead Publishing Series in Metals and Surface Engineering. Woodhead Publishing, 2012.
- [41] K. Bhattacharya, *Microstructure of martensite*. Oxford University Press, 2003.
- [42] A.G. Khachaturyan, *Theory of Structural Transformations in Solids*. Dover Books on Engineering Series. Dover Publications, 2008.

- [43] E. Pereloma and D. V. Edmonds, editors, Phase Transformations in Steels. Woodhead Publishing Series in Metals and Surface Engineering. Woodhead Publishing, 2012.
- [44] M.-X. Zhang and P. M. Kelly, Crystallographic features of phase transformations in solids. *Progress in Materials Science*, 54(8):1101–1170, 2009.
- [45] M. S. Wechsler, D. S. Lieberman, and T. A. Read, On the theory of the formation of martensite. *Journal of Metals*, November:1503–1515, 1953.
- [46] J. S. Bowles and J. K. Mackenzie, The crystallography of martensite transformations i. *Acta Metallurgica*, 2(1):129 – 137, 1954.
- [47] Muhammad Mohsin Khan, Damage Evolution of High Chromium Steels Utilised for High Temperature Components, Master thesis, Darmstadt, den August 1, 2018.
- [48] A.V. Idesman, V.I. Levitas, D.L. Preston, J.-Y. Cho, Finite element simulations of martensitic phase transitions and microstructures based on a strain softening model, *Journal of the Mechanics and Physics of Solids*, Volume 53, Issue 3, 2005, Pages 495-523.
- [49] Shah, A., et al. (2014) Numerical Simulation of Two-Dimensional Dendritic Growth Using Phase Field Model. *World Journal of Mechanics*, 4, 128-136.
- [50] Christian Miehe, Martina Hofacker, Fabian Welschinger, A phase field model for rate-independent crack propagation: Robust algorithmic implementation based on operator splits, *Computer Methods in Applied Mechanics and Engineering*, Volume 199, Issues 45–48, 2010, Pages 2765-2778.
- [51] J.W Cahn, J.E Hilliard, Spinodal decomposition, A reprise, *Acta Metallurgica*, Volume 19, Issue 2, 1971, Pages 151-161,
- [52] Cahn, J. W. & Hilliard, J. E, Free energy of a nonuniform system. I. Interfacial free energy. *J. Chem. Phys.*28, 258–267 (1958).
- [53] Steinbach I. Phase-field models in materials science, *Modell Simul Mater Sci Eng* 2009; 17(7):073001.
- [54] Zhang W, Jin YM, Khachaturyan AG, Phase field microelasticity modeling of heterogeneous nucleation and growth in martensitic alloys. *Acta materialia* 2007;55(2):565–74
- [55] Schoof E, Schneider D, Streichhan N , Mittnacht T , Selzer M , Nestler B, Multiphase–field modeling of martensitic phase transformation in a dual-phase microstructure. *International journal of solids and structures* 2018;134:181–94 .
- [56] She H, Liu Y, Wang B, Phase field simulation of heterogeneous cubic tetragonal martensite nucleation. *International journal of solids and structures* 2013;50(7–8):1187–91.

- [57] Babaei H, Basak A, Levitas VI, Algorithmic aspects and finite element solutions for advanced phase field approach to martensitic phase transformation under large strains. *Computational mechanics* 2019;64(4):1177–97.
- [58] Mirzakhani S, Javanbakht M, Phase field-elasticity analysis of austenite–martensite phase transformation at the nanoscale: finite element modeling. *Computational Materials Science* 2018;154:41–52 .
- [59] Mura T, *Micromechanics of defects in solids*. Springer Science & Business Media; 2013 .
- [60] R Ahluwalia, T Lookman, A Saxena, and R. C Albers. Landau theory for shape memory polycrystals. *Acta Materialia*, 52:209–218, 2004.
- [61] S.Y. Hu and L.Q. Chen. A phase-field model for evolving microstructures with strong elastic inhomogeneity. *Acta Materialia*, 49(11):1879 – 1890, 2001.
- [62] Guo XH, Shi S-Q, Ma XQ, Elastoplastic phase field model for microstructure evolution. *Applied physics letters* 2005;87(22):221910.
- [63] Taylor R.L. *Feap-a finite element analysis program*. 2014.
- [64] Zienkiewicz OC , Taylor RL , Nithiarasu P , Zhu JZ . *The finite element method*, vol 3. McGraw-hill London; 1977.
- [65] L.-Q. Chen, Y. Wang, and A. G. Khachaturyan. Kinetics of tweed and twin formation during an ordering transition in a substitutional solid solution. *Philosophical Magazine Letters*, 65:15–23, 1992.
- [66] T. J. R. Hughes, *The Finite Element Method: Linear Static and Dynamic Finite Element Analysis*. Dover Civil and Mechanical Engineering. Dover Publications, 2000.
- [67] P. Wriggers. *Nichtlineare Finite-Element-Methoden*. Springer Berlin Heidelberg, 2001.
- [68] Horacio D. Espinosa, Pablo D. Zavattieri, A grain level model for the study of failure initiation and evolution in polycrystalline brittle materials. Part I: Theory and numerical implementation, *Mechanics of Materials*, Volume 35, Issues 3–6, 2003, Pages 333-364.
- [69] X.-P. Xu, A. Needleman, Numerical simulations of fast crack growth in brittle solids, *Journal of the Mechanics and Physics of Solids*, Volume 42, Issue 9, 1994, Pages 1397-1434.
- [70] M. Elices, G.V. Guinea, J. Gómez, J. Planas, The cohesive zone model: advantages, limitations and challenges, *Engineering Fracture Mechanics*, Volume 69, Issue 2, 2002, Pages 137-163.
- [71] J.D. Clayton, Dynamic plasticity and fracture in high density polycrystals: constitutive modeling and numerical simulation, *Journal of the Mechanics and Physics of Solids*, Volume 53, Issue 2, 2005, Pages 261-301.

- [72] Jörg F. Unger, Stefan Eckardt, Carsten Könke, Modelling of cohesive crack growth in concrete structures with the extended finite element method, *Computer Methods in Applied Mechanics and Engineering*, Volume 196, Issues 41–44, 2007, Pages 4087–4100.
- [73] Nicolas Moës, Ted Belytschko, Extended finite element method for cohesive crack growth, *Engineering Fracture Mechanics*, Volume 69, Issue 7, 2002, Pages 813–833.
- [74] Ortiz M , Pandolfi A, Finite-deformation irreversible cohesive elements for three-dimensional crack-propagation analysis. *International journal for numerical methods in engineering* 1999;44(9):1267–82.
- [75] Moës N , Dolbow J , Belytschko T, A finite element method for crack growth without remeshing. *International journal for numerical methods in engineering* 1999;46(1):131–50 .
- [76] Wu J-Y, Nguyen VP, Nguyen CT, Sutula D, Bordas S, Sinaie S. Phase-field modeling of fracture. *Advances in applied mechanics: multi-scale theory and computation* 2019. doi: 10.1016/bs.aams.2019.08.001.
- [77] Surendran M, Natarajan S , Palani GS , Bordas SPA . Linear smoothed extended finite element method for fatigue crack growth simulations. *Engineering fracture mechanics* 2019;206:551–64.
- [78] Surendran M , Natarajan S , Bordas SPA , Palani GS . Linear smoothed extended finite element method. *International journal for numerical methods in engineering* 2017;112(12):1733–49.
- [79] Martínez-Pañeda E, Natarajan S , Bordas S, Gradient plasticity crack tip characterization by means of the extended finite element method. *Computational mechanics* 2017;59(5):831–42.
- [80] Karamnejad A, Nguyen VP, Sluys LJ, A multi-scale rate dependent crack model for quasi-brittle heterogeneous materials. *Engineering fracture mechanics* 2013;104:96–113.
- [81] Sutula D , Kerfriden P , Van Dam T , Bordas SPA, Minimum energy multiple crack propagation. part III: XFEM computer implementation and applications. *Engineering fracture mechanics* 2018;191:257–76.
- [82] Kuhn C , Müller R . A continuum phase field model for fracture. *Engineering fracture mechanics* 2010;77(18):3625–34.
- [83] Schlüter A , Willenbücher A , Kuhn C , Müller R . Phase field approximation of dynamic brittle fracture. *Computational mechanics* 2014;54(5):1141–61.
- [84] Liu Z , Juhre D . Phase-field modelling of crack propagation in anisotropic polycrystalline materials. *Procedia Structural Integrity* 2018;13:787–92.
- [85] Makvandi R , Duczek S , Juhre D . A phase-field fracture model based on strain gradient elasticity. *Engineering fracture mechanics* 2019;220:106648.

- [86] De, L , Gerasimov T . Numerical implementation of phase-field models of brittle fracture. In: *Modeling in Engineering Using Innovative Numerical Methods for Solids and Fluids*. Springer; 2020. p. 75–101.
- [87] Ambati M , Gerasimov T , De Lorenzis L . A review on phase-field models of brittle fracture and a new fast hybrid formulation. *Computational mechanics* 2015;55(2):383–405.
- [88] Bourdin B , Francfort GA , Marigo J-J . The variational approach to fracture. *Journal Of Elasticity* 2008;91(1–3):5–148.
- [89] Jin Y , González-Estrada OA , Pierard O , Bordas S . Error-controlled adaptive extended finite element method for 3d linear elastic crack propagation. *Computer methods in applied mechanics and engineering* 2017;318:319–48.
- [90] Muixía A , Fernández-Méndez S , Rodríguez-Ferran A . Adaptive refinement for phase-field models of brittle fracture based on nitsches method. *Computational mechanics* 2020:1–17.
- [91] Lee S , Wheeler MF , Wick T . Pressure and fluid-driven fracture propagation in porous media using an adaptive finite element phase field model. *Computer methods in applied mechanics and engineering* 2016;305:111–32.
- [92] Badnava H , Msekh MA , Etemadi E , Rabczuk T . An h-adaptive thermo-mechanical phase field model for fracture. *Finite Elements in Analysis and Design* 2018;138:31–47.
- [93] Patil RU , Mishra BK , Singh IV . An adaptive multiscale phase field method for brittle fracture. *Computer methods in applied mechanics and engineering* 2018;329:254–88.
- [94] Pramod A , Annabattula RK , Ooi ET , Song C , Natarajan S , et al. Adaptive phase-field modeling of brittle fracture using the scaled boundary finite element method. *Computer methods in applied mechanics and engineering* 2019;355:284–307.
- [95] Tian F , Tang X , Xu T , Yang J , Li L . A hybrid adaptive finite element phase-field method for quasi-static and dynamic brittle fracture. *International journal for numerical methods in engineering* 2019;120(9):1108–25.
- [96] Michael J. Borden, Thomas J.R. Hughes, Chad M. Landis, Clemens V. Verhoosel, A higher-order phase-field model for brittle fracture: Formulation and analysis within the isogeometric analysis framework, *Computer Methods in Applied Mechanics and Engineering*, Volume 273, 2014, Pages 100-118.
- [97] Tanné E , Li T , Bourdin B , Marigo J-J , Maurini C . Crack nucleation in variational phase-field models of brittle fracture. *Journal of the mechanics and physics of solids* 2018;110:80–99.
- [98] Amor H , Marigo J-J , Maurini C , Regularized formulation of the variational brittle fracture with unilateral contact: numerical experiments. *Journal of the Mechanics and Physics of Solids*. 2009; 57:1209- 29.



- [99] Charlotte Kuhn, Ralf Müller, A continuum phase field model for fracture, *Engineering Fracture Mechanics*, Volume 77, Issue 18, 2010, Pages 3625-3634.
- [100] Kuhn C, Müller R, A phase field model for fracture. *PAMM*. 2008; 8:10223-4.
- [101] Borzabadi Farahani, E. and Juhre, D. (2021), A phase field approach to study of transformation induced micro-cracking in a martensitic phase transformation. *Proc. Appl. Math. Mech.*, 20: e202000291.
- [102] E. Borzabadi Farahani, B. Sobhani Aragh, A. Sarhadi, D. Juhre, A framework to model thermomechanical coupled of fracture and martensite transformation in austenitic microstructures, *Thin-Walled Structures*, Volume 183, 2023, 110435.
- [103] Schmidt, S., Dornisch, W. and Müller, R. (2017), A phase field model for martensitic transformation coupled with the heat equation. *GAMM-Mitteilungen*, 40: 138-153.
- [104] L. Sandoval, H. M. Urbassek, and P. Entel, *New Journal of Physics* 11(10), (2009).
- [105] F. Nix and D. MacNair, *Physical Review* 60(8), 597 (1941)
- [106] S. Schmidt, C. Plate, R. Muller, R. Müller, J. Meiser, and H. M. Urbassek, *PAMM* 16(1), 481–482 (2016).
- [107] Cheikh Cissé, Mohsen Asle Zaeem, Design of NiTi-based shape memory microcomposites with enhanced elastocaloric performance by a fully thermomechanical coupled phase-field model, *Materials & Design*, Volume 207, 2021, 109898.
- [108] H. M. Urbassek and L. Sandoval, *Phase transformations in steels, vol. 2: Diffusionless transformations, high strength steels, modelling and advanced analytical techniques*, 2012.
- [109] Kuhn, C. and Müller, R. (2009), Phase field simulation of thermomechanical fracture. *Proc. Appl. Math. Mech*, 9: 191-192.
- [110] Bhattacharya K. *Why it forms and how it gives rise to the shape-memory effect. Microstructure of Martensite* Oxford University Press, Oxford 2003 .
- [111] Meng QP, Rong YH , Hsu TY . Effect of internal stress on autocatalytic nucle- ation of martensitic transformation. *Metallurgical and Materials Transactions A* 2006;37(5):1405–11 .
- [112] T. Zhao, J. Zhu, J. Luo, Study of crack propagation behavior in single crystalline tetragonal zirconia with the phase field method, *Engineering Fracture Mechanics* 159 (2016) 155–173.
- [113] J. Stolarz, N. Baffie, T. Magnin, Fatigue short crack behaviour in metastable austenitic stainless steels with different grain sizes, *Materials Science and Engineering: A* 319 (2001)
- [114] Ehsan Mohtarami, Alireza Baghbanan, Hamid Hashemolhosseini, Stéphane P.A. Bordas, Fracture mechanism simulation of inhomogeneous anisotropic rocks by extended finite element method, *Theoretical and Applied Fracture Mechanics*, Volume 104, 2019, 102359.

- [115] Malekan, M., Barros, F.B. Numerical analysis of a main crack interactions with micro-defects/inhomogeneities using two-scale generalized/extended finite element method. *Comput Mech* 62, 783–801 (2018).
- [116] Alshoaibi, A.M.; Fageehi, Y.A. Finite Element Simulation of a Crack Growth in the Presence of a Hole in the Vicinity of the Crack Trajectory. *Materials* 2022, 15, 363.
- [117] Lal, A., Vaghela, M., Mishra, K. (2021). Numerical Analysis of an Edge Crack Isotropic Plate with Void/Inclusions under Different Loading by Implementing XFEM. *Journal of Applied and Computational Mechanics*, 7(3), 1362-1382. doi: 10.22055/jacm.2019.31268.1848
- [118] M.A. Meyers, A. Mishra, D.J. Benson, *Prog. Mater. Sci.* 51 (2006) 427–556.
- [119] H.D. Espinosa, P.D. Zavattieri, *Mech. Mater.* 35 (2003) 333–364.
- [120] I. Szlufarska, A. Nakano, P. Vashishta, *Science* 309 (2005) 911–914.
- [121] R.A. Andrievski, *Rev. Adv. Mater. Sci.* 22 (2009) 1–20.
- [122] N. Sukumar, D.J. Srolovitz, T.J. Baker, and J-H. Prévost. Brittle fracture in polycrystalline microstructures with the extended finite element method. *International Journal for Numerical Methods in Engineering*, 56(14):2015– 2037, 2003.
- [123] B. Moran T. Belytschko N. Sukumar, N. Moes. Extended finite element method for three-dimensional crack modeling. *International Journal for Numerical Methods in Engineering.*, 48(11):1549–70, 2000.
- [124] W.H. Yang, D.J. Srolovitz, G.N. Hassold, and M.P. Anderson. Microstructural effects in the fracture of brittle materials. *Simulation and Theory of Evolving Microstructures*, pages 277–284, 1990.
- [125] McMeeking, R.M.; Evans, A.G. Mechanics of Transformation-Toughening in Brittle Materials. *J. Am. Ceram. Soc.* 1982, 65, 242–246
- [126] Budiansky, B.; Hutchinson, J.W.; Lambropoulos, J.C. Continuum Theory of Dilatant Transformation Toughening in Ceramics. *Int. J. Solids Struct.* 1983, 19, 337–355.
- [127] Lambropoulos, J.C. Shear, shape and orientation effects in transformation toughening. *Int. J. Solids Struct.* 1986, 22, 1083–1106.
- [128] Chen, I.W.; Reyes-Morel, P.E. Transformation Plasticity and Transformation Toughening in Mg-PSZ and Ce-TZP. *MRS Proc.* 1986, 78, 75
- [129] E. Borzabadi Farahani, B. Sobhani Aragh, J. Voges, D. Juhre, On the crack onset and growth in martensitic micro-structures; a phase-field approach, *International Journal of Mechanical Sciences*, Volume 194, 2021, 106187.

- [130] Yeddu, Hemantha Kumar, et al. "3D Phase Field Modeling of Martensitic Microstructure Evolution in Steels." *Solid State Phenomena*, vol. 172–174, Trans Tech Publications, Ltd., June 2011, pp. 1066–1071.
- [131] H. Z. Chen *and* Y. C. Shu, Phase-field modeling of martensitic microstructure with inhomogeneous elasticity, *Journal of Applied Physics* 113, 123506 (2013).
- [132] Oğuz Umut Salman, Alphonse Finel, Rémi Delville, and Dominique Schryvers, The role of phase compatibility in martensite", *Journal of Applied Physics* 111, 103517 (2012).
- [133] Bhowmick S, Liu G-R. Three Dimensional CS-FEM Phase-Field Modeling Technique for Brittle Fracture in Elastic Solids. *Applied Sciences*.2018;8(12):2488.
- [134] Ephraim Schoof, Daniel Schneider, Nick Streichhan, Tobias Mittnacht, Michael Selzer, Britta Nestler, Multiphase-field modeling of martensitic phase transformation in a dual-phase microstructure, *International Journal of Solids and Structures*, Volume 134, 2018.
- [135] Harison da Silva Ventura, Gabriella Maria Silveira de Sá, Aline Cristine Lemos Duarte, Wesley Luiz da Silva Assis, Paulo Rangel Rios, Original Article Computer simulation in 3D of a phase transformation nucleated by simple sequential inhibition process, *Journal of Materials Research and Technology*, Volume 9, Issue 1, 2020.
- [136] Hemantha Kumar Yeddu, Hongxiang Zong, Turab Lookman, Alpha – omega and omega–alpha phase transformations in zirconium under hydrostatic pressure: A 3D mesoscale study, *Acta Materialia*, Volume 102, 2016.
- [137] J.D. Clayton, J. Knap, Phase field modeling of directional fracture in anisotropic polycrystals, *Computational Materials Science*, Volume 98, 2015, Pages 158-169.
- [138] Thanh Tung Nguyen, Julien Rethore, Julien Yvonnet, Marie-Christine Baietto. Multi-phase-field modeling of anisotropic crack propagation for polycrystalline materials. *Computational Mechanics*, Springer Verlag, 2017, 60 (2), pp.289-314.
- [139] Nguyen, Thanh-Tung, Réthoré, Julien, Baietto, Marie-Christine, Bolivar, José, Fregonese, Marion and Bordas, Stéphane P.A, Modeling of inter- and transgranular stress corrosion crack propagation in polycrystalline material by using phase field method, *Journal of the Mechanical Behavior of Materials*, vol. 26, no. 5-6, 2017, pp. 181-191.
- [140] Farahani EB, Aragh BS, Juhre D. Interplay of Fracture and Martensite Transformation in Microstructures: A Coupled Problem. *Materials*. 2022; 15(19):6744.
- [141] Arezoo Emdadi, William G. Fahrenholtz, Gregory E. Hilmas, Mohsen Asle Zaeem, A modified phase-field model for quantitative simulation of crack propagation in single-phase and multi-phase materials, *Engineering Fracture Mechanics*, Volume 200, 2018, Pages 339-354.
- [142] Arezoo Emdadi, Mohsen Asle Zaeem, Phase-field modeling of crack propagation in polycrystalline materials, *Computational Materials Science*, Volume 186, 2021, 110057.

- [143] Shahed Rezaei, Stephan Wulfinghoff, Stefanie Reese, Prediction of fracture and damage in micro/nano coating systems using cohesive zone elements, *International Journal of Solids and Structures*, Volume 121, 2017, Pages 62-74.
- [144] Shahed Rezaei, Jaber Rezaei Mianroodi, Tim Brepols, Stefanie Reese, Direction-dependent fracture in solids, Atomistically calibrated phase-field and cohesive zone model, *Journal of the Mechanics and Physics of Solids*, Volume 147, 2021, 104253.
- [145] Seleš, K., Aldakheel, F., Tonković, Z. et al, A general phase-field model for fatigue failure in brittle and ductile solids. *Comput Mech* 67, 1431–1452 (2021).
- [146] Schreiber, C., Müller, R. & Kuhn, C. Phase field simulation of fatigue crack propagation under complex load situations. *Arch Appl Mech* 91, 563–577 (2021).
- [147] Xi S, Su Y. Phase Field Study of the Microstructural Dynamic Evolution and Mechanical Response of NiTi Shape Memory Alloy under Mechanical Loading. *Materials*. 2021; 14(1):183.
- [148] Yuan Zhong, Ting Zhu, Phase-field modeling of martensitic microstructure in NiTi shape memory alloys, *Acta Materialia*, Volume 75, 2014, Pages 337-347.
- [149] Marlini Simoes, Emilio Martínez-Pañeda, Phase field modelling of fracture and fatigue in Shape Memory Alloys, *Computer Methods in Applied Mechanics and Engineering*, Volume 373, 2021, 113504.
- [150] Cheikh Cissé, Mohsen Asle Zaeem, A phase-field model for non-isothermal phase transformation and plasticity in polycrystalline yttria-stabilized tetragonal zirconia, *Acta Materialia*, Volume 191, 2020, Pages 111-123.